Generation of electromagnetic waves by electrons rotating in a radial electrostatic field in free space

V. V. Dolgopolov and Yu. V. Kirichenko

Kharkov Physicotechnical Institute
(Submitted January 28, 1999)
Pis'ma Zh. Tekh. Fiz. **25**, 1–4 (November 12, 1999)

A theoretical analysis is made of mechanisms for the generation of electromagnetic waves by electrons rotating in a radial electrostatic field formed by a positively charged filament in free space. A dispersion equation is obtained to describe the interaction between the waves and nonrelativistic electrons. It is shown that electromagnetic fields can be generated by means of Čerenkov resonance. The frequencies and growth rates of the emitted waves are determined and their dependence on the parameters of the problem is investigated.
 [S1063-7850(99)00111-1]

We shall consider a cylindrical layer of electrons, unbounded along the z axis (using cylindrical coordinates r,φ,z), which rotate about the axis, upon which is located a metal charged filament of radius a and having a linear positive charge density Q. The electrons are confined to equilibrium circular orbits by the radial electrostatic field of the filament $E_0(r)=2Q/r$. We shall neglect the self-induced constant electrostatic and magnetic fields of the electron layer. It is assumed that the perturbations of the electromagnetic fields, the density, and electron velocity do not depend on z. We denote the dependence of all the perturbations on φ and time t by the factor $\exp[i(m\varphi-\omega t)]$, where $m\neq 0$ is an integer and ω is the frequency. We make the analysis in the hydrodynamic approximation. The unperturbed density $n(r)$ is nonzero between the surfaces $r=r_-$ and $r=r_+$. The method described in Ref. 1 can be used to show that, in the linear approximation for a thin layer when

$$r_+ - r_- = \delta r \ll r_-, \tag{1}$$

the perturbation component of the magnetic field H_z satisfies the following boundary conditions at the electron layer:

$$\left.\frac{dH_z}{dr}\right|_{r_+} = \left.\frac{dH_z}{dr}\right|_{r_-}, \quad H_z|_{r_+} - H_z|_{r_-} = \lambda \left.\frac{dH_z}{dr}\right|_{r_-}, \tag{2}$$

where

$$\lambda = \int_{r_-}^{r_+} dr\left(1-\frac{\Omega^2(r)}{W}\right) - \left(\frac{2V^2}{r^2\omega_m^2 W}\right)_{r_-} \int_{r_-}^{r_+} dr\,\Omega^2(r)\,\frac{W+\Omega^2}{W-\Omega^2}; \tag{3}$$

$V=[2eQ/m_e]^{1/2}$ is the equilibrium unperturbed electron velocity, $-e<0$, m_e are the electron charge and mass, $\omega_m=\omega-mV/r_-$, $W=\omega_m^2-2V^2/r^2$, and $\Omega^2(r)=4\pi e^2 n(r)/m_e$. The value of H_z in vacuum is given by

$$H_z = AJ_m(kr)+BN_m(kr) \quad a\leqslant r\leqslant r_-, \tag{4}$$

$$H_z = CH_m^{(1)}(kr) \quad r_+\leqslant r, \tag{5}$$

where $k=\omega/c$, c is the velocity of light, $J_m(x)$, $N_m(x)$, and $H_m^{(1)}$ are Bessel, Neumann, and Hankel functions, respectively, and A and B are integration constants. Matching H_z and dH_z/dr at the layer boundaries, assuming that $dH_z/dr=0|_{r=a}$, and taking account of Eq. (1), we obtain the dispersion equation

$$H_m^{(1)'}(x_1)G(x,x)+\lambda k H_m^{(1)'}(x)K(x,x_1)=0, \tag{6}$$

where

$$G(x,y)=J_m(x)N_m'(y)-N_m(x)J_m'(y),$$

$$K(x,y)=J_m'(x)N_m'(y)-N_m'(x)J_m'(y), \tag{7}$$

$x_1=ka$, $x=kr$, and $\delta x=k\delta r$. Since Eq. (6) remains unchanged as a result of making the transformations $m\Rightarrow -m$ and $\omega\Rightarrow-\omega$, it is sufficient to solve this equation for $m>0$ and $\mathrm{Re}(\omega)>0$. As in Ref. 6, we shall confine ourselves to solving Eq. (6) in the approximation

$$|x|\ll 2m^{1/2}. \tag{8}$$

Quite clearly, interaction between electrons and a wave will be most effective in the case of resonances (Čerenkov or plasma). We shall analyze the Čerenkov resonance

$$\omega_m(r_-)\simeq 0. \tag{9}$$

If conditions (8) and (9) are satisfied, the dispersion equation (6) has the form

$$\omega_m=\pm(\Delta)^{1/2}, \tag{10}$$

where

$$\Delta=\frac{(\delta_m+i)\,\eta_m}{\delta_m+i\,\eta^{2m}}\,\frac{m}{r_-}\int_{r_-}^{r_+} dr\,\Omega^2(r)\,\frac{\Omega^2(r)-2V^2/r^2}{\Omega^2(r)+2V^2/r^2}; \tag{11}$$

$\delta_m=\pi x^{2m}/[(m-1)!\,m!\,2^{2m}]$, $\eta=r_-/a$, and $\eta_m=(\eta^{2m}-1)/2$. Utilizing the fact that condition (9) implies $|\mathrm{Im}(\omega)|\ll\mathrm{Re}(\omega)$, from Eqs. (10) and (11) we obtain expressions for the frequencies and growth rates. Under these conditions two cases are possible.

For

$$2V^2 > r_-^2 \bar{\Omega}^2, \tag{12}$$

we have

$$\mathrm{Re}(\omega) = \frac{mV}{r_-} + 0\left(\left(\frac{\delta r}{r_-}\right)^{1/2} x_r^{2m}\right), \tag{13}$$

$$\mathrm{Im}(\omega) = \bar{\Omega}\left(\frac{m\eta_m}{\eta^{2m}}\right)^{1/2}\left(\frac{2V^2 - r_-^2\bar{\Omega}^2}{2V^2 + r_-^2\bar{\Omega}^2}\right)^{1/2}\left(\frac{\delta r}{r_-}\right)^{1/2}. \tag{14}$$

For

$$2V^2 < r_-^2 \bar{\Omega}^2, \tag{15}$$

we have

$$\mathrm{Re}(\omega) = \frac{mV}{r_-} - 0\left(\left(\frac{\delta r}{r_-}\right)^{1/2}\right), \tag{16}$$

$$\mathrm{Im}(m) = \bar{\Omega}\left(\frac{\eta_m}{\eta^{2m}}\right)^{3/2} \frac{\pi x_r^{2m} m^{1/2}}{(m-1)!\, m!\, 2^{2m}} \times \left(\frac{r_-^2\bar{\Omega}^2 - 2V^2}{2V^2 + r_-^2\bar{\Omega}^2}\right)^{1/2}\left(\frac{\delta r}{r_-}\right)^{1/2}, \tag{17}$$

where $x_r = \mathrm{Re}(x)$ and $\bar{\Omega}$ is given by

$$\bar{\Omega}^2 \frac{r_-^2\bar{\Omega}^2 - 2V^2}{r_-^2\bar{\Omega}^2 + 2V^2} = \frac{1}{\delta r}\int_{r_-}^{r_+} dr\,\Omega^2(r)\frac{r^2\Omega^2(r) - 2V^2}{r^2\Omega^2(r) + 2V^2}. \tag{18}$$

It follows from expressions (12)–(17) that if condition (12) is satisfied, the growth rate is much larger than that for condition (15) when waves are generated by their emission into the surrounding space. Note that when condition (12) is satisfied, the electrons lag behind the waves whereas when condition (15) is satisfied, they precede the wave. It can be seen from formulas (14) and (17) that the growth rate is a nonmonotonic function of the velocity V (or the charge density Q). The growth rate (17) has a maximum when

$$V_m^2 = \frac{r_-\bar{\Omega}^2}{2}\frac{(m^2+1)^{1/2} - 1}{m}. \tag{19}$$

The growth rate given by formula (14) increases with increasing V and for fairly large V does not depend on V. For large $\bar{\Omega}$, when $\bar{\Omega}^2 \gg 2V^2/r^2$, $\mathrm{Im}(\omega)$ increases linearly with increasing $\bar{\Omega}$. The dependences of the growth rates (14) and (17) on m differ qualitatively. When the electrons lag behind the wave, $\mathrm{Im}(\omega)$ increases monotonically with increasing m as $m^{1/2}$ whereas when the electrons precede the wave, this dependence decreases exponentially.

[1] Z. S. Chernov, Radiotekh. Elektron. (Moscow) **1**, 1428 (1956).
[2] G. A. Bernashevskiĭ and T. A. Novskova, Radiotekh. Elektron. (Moscow) **3**, 1218 (1958).
[3] Z. S. Chernov and G. A. Bernashevskiĭ, Radiotekh. Elektron. (Moscow) **8**, 973 (1963).
[4] I. Alexeff and F. Dyer, Phys. Rev. Lett. **45**, 351 (1980).
[5] F. Dyer, M. Rader, A. Matas *et al.*, in *Abstracts of the 1990 IEEE International Conference on Plasma Science, Piscataway, NJ*, p. 209.
[6] V. V. Dolgopolov, Yu. V. Kirichenko, Yu. F. Lonin, and I. F. Kharchenko, Zh. Tekh. Fiz. **68**(8), 91 (1998) [Tech. Phys. Lett. **43**, 959 (1998)].

Translated by R. M. Durham

Electromagnetic quadrupole-octupole lens

L. P. Ovsyannikova and T. Ya. Fishkova

A. F. Ioffe Physicotechnical Institute, Russian Academy of Sciences, St. Petersburg
(Submitted June 2, 1999)
Pis'ma Zh. Tekh. Fiz. **25**, 5–7 (November 12, 1999)

A design is proposed for an electromagnetic quadrupole lens with correction for spherical chromatic aberration. This lens consists of eight electrodes, of which four are also the poles of the magnet. © *1999 American Institute of Physics.* [S1063-7850(99)00211-6]

Systems of quadrupole lenses are frequently used for transporting high-energy beams. Recently, a system of four quadrupole lenses which produces a true image similar to an axisymmetric lens, known as the ''Russian Quadruplet''[1] has been used in electron microscopy and also to develop nanometer ion probes.[2,3] In these systems the problem of eliminating spherical chromatic aberration is highly relevant because this aberration strongly influences the resolution of electron microscopes and the probe diameter in microanalyzers.

Kel'man and Yavor[4] and also Yavor *et al.*[4] proposed and investigated an achromatic quadrupole lens based on spatially matched electrostatic and magnetic lenses whose powers were directed in opposite directions. The electrostatic lens is located inside the magnetic one.

In a review[5] Yavor *et al.* describe conditions for the correction of spherical aberration in various systems of quadrupole lenses by using octupoles, and give designs of electrostatic quadrupole-octupole lenses with concave cylindrical electrodes.

In the present paper we propose a simplified design of achromatic quadrupole lens with correction for spherical aberration. The lens cross section is shown in Fig. 1. The electrodes of the quadrupole-octupole lens take the form of a cylinder cut into eight sections having the same angular dimensions along the generating lines. The four electrodes positioned between the quadrupole electrodes are also the pole pieces of the magnetic lens. In this case, the apertures of the magnetic and electrostatic lenses are the same so that the power of the magnetic lens for which the condition for correction of chromatic aberration is satisfied is lower than that in the achromatic lenses normally used (see, for example, Ref. 4). An additional advantage of the proposed design is that the electrode-poles can be fabricated and installed more accurately relative to each other compared with differently shaped electrodes and poles.

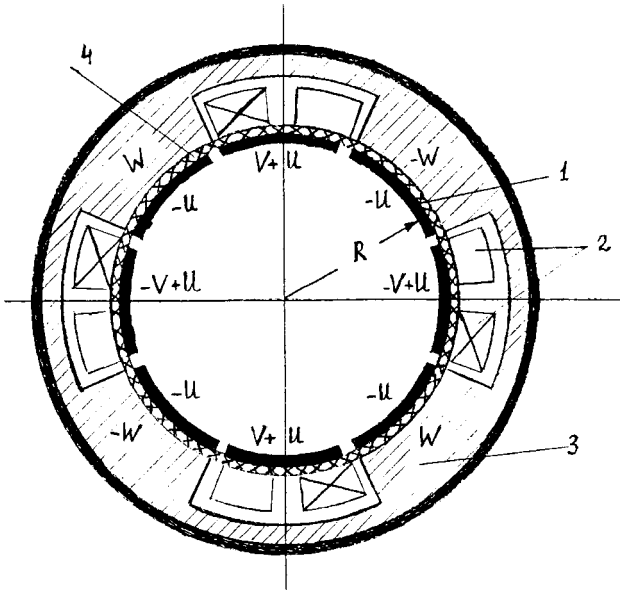

FIG. 1. Cross section through eight-electrode electromagnetic quadrupole lens: *1* — electrode-pole, *2* — electromagnet winding, *3* — yoke of magnet, and *4* — insulator.

The scalar potential distribution of the proposed electromagnetic eight-electrode quadrupole-octupole lens was obtained for the two-dimensional case in a closed form similar to that obtained in Ref. 6 for an electrostatic four-electrode quadrupole lens having angular dimensions of $\pi/2$. In a cylindrical coordinate system (r,φ), provided that the gaps between the electrode-poles of angular dimensions $\pi/4$ are infinitely small, this distribution has the form:

$$\Phi_{\mathrm{EM}}(r,\varphi)=1/\pi\{(W-V)\arctan[2\rho^2\sin(\pi/4)+2\varphi/(1-\rho^4)]-(W+V)\arctan[2\rho^2\sin(\pi/4-2\varphi)/(1-\rho^4)]+2U\arctan[2\rho^4\cos 4\varphi/(1-\rho^8)]\},$$

where $\rho=r/R$ (R is the radius of the lens aperture), $\pm V$ and $\pm U$ are the potentials of the electrostatic quadrupole and octupole, respectively, and $\pm W$ is the scalar potential of the magnetic quadrupole lens.

An analytic solution of the field problem can be used to solve the differential equation for the charged particle trajectories in a separate combined quadrupole-octupole lens and in systems of these.

To conclude, we note that the proposed simplified design of a combined quadrupole-octupole lens with corrected spherical chromatic aberration is useful for developing multielement systems, and in particular the Russian Quadruplet.

[1] A. D. Dymnikov and S. Ya. Yavor, Zh. Tekh. Fiz. **33**, 851 (1963) [Sov. Phys. Tech. Phys. **8**, 639 (1963)]; A. D. Dymnikov, T. Ya. Fishkova, and S. Ya. Yavor, Zh. Tekh. Fiz. **35**, 431 (1965) [Sov. Phys. Tech. Phys. **10**, 340 (1965)].

[2] A. D. Dymnikov and G. Martínez, Nucl. Instrum. Methods Phys. Res. B **130**, 64 (1997).
[3] H. Wollnik, M. I. Yavor, and A. G. Kalimov, Rev. Sci. Instrum. **69**, 4116 (1998).
[4] V. M. Kel'man and S. Ya. Yavor, Zh. Tekh. Fiz. **31**, 1439 (1961) [Sov. Phys. Tech. Phys. **6**, 1052 (1961)]; S. Ya. Yavor, A. D. Dymnikov, and L. P. Ovsyannikova, Nucl. Instrum. Methods **26**, 13 (1964).
[5] S. Ya. Yavor, T. Ya. Fishkova, E. V. Shpak, and L. A. Baranova, Nucl. Instrum. Methods **76**, 181 (1969).
[6] A. M. Strashkevich, *Electron Optics of Electrostatic Fields*, (Énergiya, Moscow 1966), pp. 141–142.

Translated by R. M. Durham

Waveguide properties of a four-layer resonant planar structure

D. I. Sementsov, A. M. Shutyĭ, and D. G. Sannikov

Ulyanovsk State University
(Submitted March 22, 1999)
Pis'ma Zh. Tekh. Fiz. **25**, 8–14 (November 12, 1999)

The waveguide properties of a four-layer structure for which the permittivity of the cover layer has a resonant frequency dependence in the optical range are investigated. The condition for maximum mode absorption is obtained. It is observed that there is a frequency range in which the damping of the TE mode exceeds that of the TM mode. It is shown that the mode damping decreases appreciably in the range of negative values of the cover layer permittivity.
 [S1063-7850(99)00311-0]

Optical waveguides with an absorbing cover layer are widely used to develop polarizing filters in information transfer and processing systems, modulators, switches, and photodetectors.[1,2] The unique properties of these waveguides are caused by a periodic coupling effect between the modes of the waveguide and cover layers.[3] Recent interest has been directed toward multilayer structures in which the permittivity of one layer depends on frequency.[4,5] In the present paper we consider for the first time how the waveguide properties of a four-layer planar structure are influenced by a cover layer whose permittivity has a resonant frequency dependence.

Let us assume that this waveguide structure consists of four layers, of which three are described by real permittivities (ε_1 for the substrate, ε_2 for the main waveguiding layer, and ε_4 for the covering medium) which are constants in the optical range under study. The fourth (cover) layer is in resonance with the permittivity

$$\varepsilon_3(\omega)=\varepsilon_\infty+(\varepsilon_0-\varepsilon_\infty)\omega_0^2/(\omega_0^2-\omega^2+i\omega g), \tag{1}$$

where ω_0 is the resonant frequency which lies in the frequency range under study, g is the width of the resonance curve, and ε_0 and ε_∞ are the static permittivity and the permittivity under rf excitation. The structure is positioned such that the x axis is perpendicular to the interface between the layers and the radiation propagates in the direction of the z axis. The interface between the substrate and the waveguide layer lies in the plane $x=-L_2$, that between the waveguide and the cover layers lies in the plane $x=0$, and that between the cover layer and the medium lies in the plane $x=L_3$.

We express the field of the waveguide mode in the structure in the form:

$$F_\alpha(x,z)=C\mathscr{F}_\alpha(x)\exp(-i\beta z), \quad \alpha=x,y,z, \tag{2}$$

where C is the normalization constant, β is the propagation constant which, taking account of Eq. (1), is complex: the imaginary part of the propagation constant β'' determines the mode damping in the structure, while the real part is associated with its phase velocity ($\beta'=\omega/v_{ph}$); $\mathscr{F}_\alpha(x)$ are profile functions which define the distribution of the mode field over the waveguide thickness.

The dispersion equation relating the propagation constant of the waveguide mode to the parameters of the waveguide structure and the radiation is obtained from the condition that the tangential components of the fields are continuous at the interfaces, and has the following form:[6]

$$\begin{aligned}&(\delta h_1 h_3^2\tau+\sigma h_1^2 h_4)\tanh h_2L_2\cdot\tanh h_3L_3+h_3\\&\times(h_2^2-\delta\sigma\tau h_1h_4)\tanh h_2L_2+h_2(h_3^2\tau-\delta\sigma h_1h_4)\\&\times\tanh h_3L_3-h_2h_3(\delta h_1+\sigma\tau h_4)=0.\end{aligned} \tag{3}$$

Here the transverse components of the wave vector in each layer are given by:

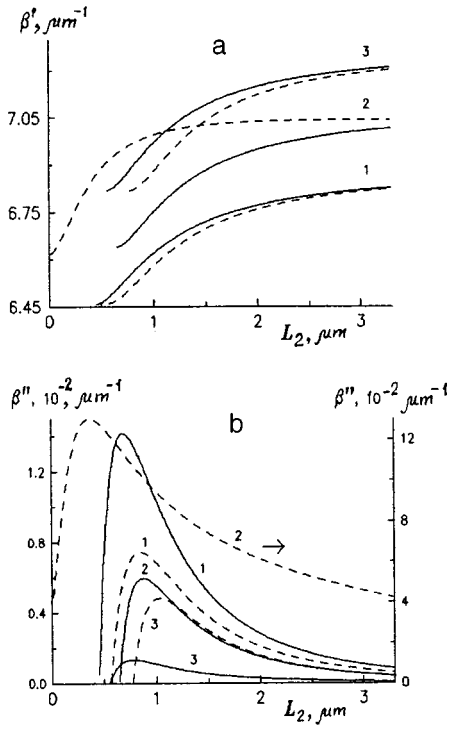

FIG. 1. Dependences of the real (a) and imaginary (b) parts of the propagation constant β on the thickness of the waveguiding layer L_2 for $L_3=0.2\ \mu$m for three frequencies close to the optical resonance; the solid curves corresponds to the TE_0 mode and the dashed curves to the TM_0 modes.

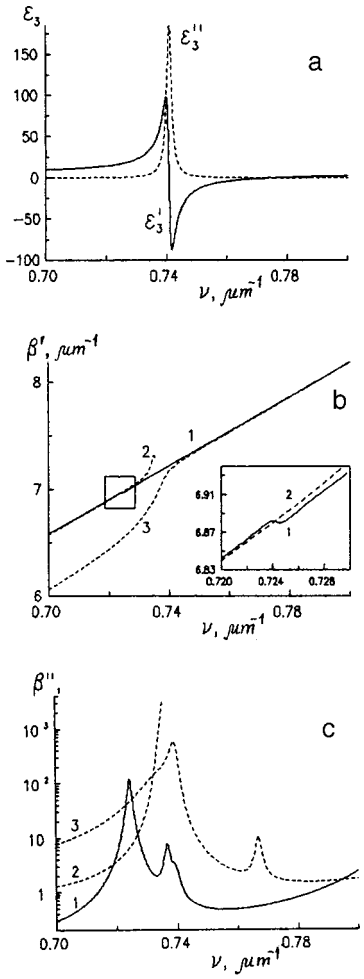

FIG. 2. Frequency dependences of the real and imaginary parts of the resonant layer permittivity (a) and of the real (b) and imaginary (c) parts of the propagation constants of the TE_0, TM_0, and TM_1 modes (curves *1–3*) for waveguiding and cover layers of thickness $L_2=4\ \mu$m and $L_3=0.2\ \mu$m.

$$h_{1,4}^2=\beta^2-k_0^2\varepsilon_{1,4},\quad h_{2,3}^2=k_0^2\varepsilon_{2,3}-\beta^2, \tag{4}$$

where $k_0=\omega/c$, c is the velocity of light, and the parameters are $\sigma=\delta=\tau=1$ for the TE modes and $\sigma=\varepsilon_3/\varepsilon_4$, $\delta=\varepsilon_2/\varepsilon_3$, $\tau=\varepsilon_2/\varepsilon_3$ for TM modes.

Here we present results of a numerical analysis of Eq. (3) and the waveguide regimes in the structure of the optical resonance region, for which we take the following values of the structure parameters: $\varepsilon_0=5.8$, $\varepsilon_\infty=5.3$, $\varepsilon_1=2.04$, $\varepsilon_2=2.31$, $\varepsilon_4=1$, $L_3=0.2\ \mu$m, $\nu_0=0.74\ \mu$m (here and subsequently we use the spectroscopic frequency $\nu=\omega/2\pi c$, which corresponds to the wavelength $\lambda=1/\nu$, $\lambda_0=1.35\ \mu$m), and the line width is $g/2\pi c=2\times10^{-3}\ \mu\text{m}^{-1}$. Figure 1 gives the real (a) and imaginary (b) parts of the propagation constant as a function of the thickness of the waveguiding layer L_2 obtained for three frequencies near the optical resonance ($\nu=0.72$, 0.74, and 0.76 μm^{-1}, curves *1–3*). The solid curves correspond to the TE_0 mode and the dashed curves to the TM_0 mode (the mode number m implies the number, reduced to unity, of maxima of the square of the field function $|\mathscr{F}_y(x)|^2$ in the cross section of the waveguide layer). It can be seen from these curves that an increase in frequency shifts the dispersion curves toward higher values of β'. At the optical resonance frequency no cutoff regime exists for the TM_0 mode. The strongest mode damping occurs near the cutoff thickness.

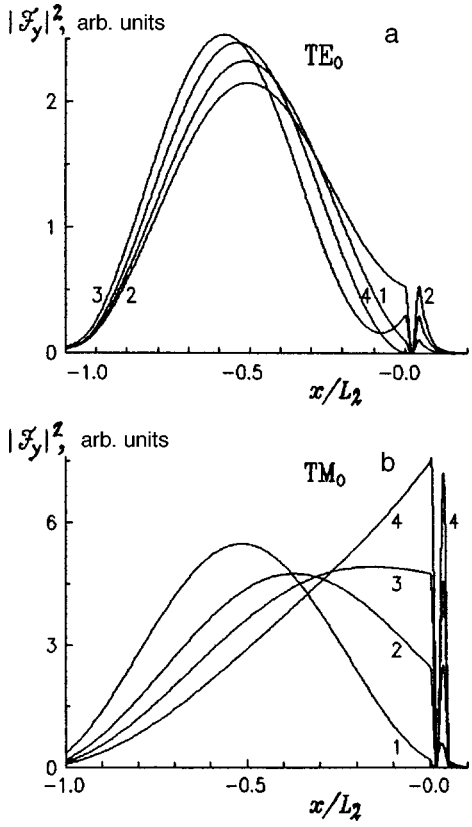

FIG. 3. Distribution of the function $|\mathscr{F}_y|^2$, which determines the energy density of the TE_0 and TM_0 modes, over the cross section of the waveguide structure (a, b) for $L_2=4\ \mu$m and $L_3=0.2\ \mu$m at various frequencies ν.

Figure 2 gives the frequency dependences of the real and imaginary parts of the resonant layer permittivity (a) and the real (b) and imaginary (c) parts of the propagation constants of the TE_0, TM_0, and TM_1 modes (curves *1, 2,* and *3*) for the selected parameters of the structure and the thickness of the waveguiding layer $L_2=4\ \mu$m. The increase in the constant β' with frequency for the TE_0 mode is linear over the entire frequency range under study, except for a small interval near $\nu_r=0.724\ \mu\text{m}^{-1}$ where β' decreases negligibly (inset to Fig. 2). For the $TM_{0,1}$ modes the dependence is linear in various parts of the spectrum. For the TM_0 mode the propagation constant β' increases abruptly for $\nu>\nu_r$ and is converted to the cover layer mode at $\nu_s\approx0.732\ \mu\text{m}^{-1}$. As a result, a sharp increase in the damping β'' of this particular mode is observed near this frequency. In the region beyond the resonance the curves of $\beta'(\nu)$ for the TE_0 and TM_1 modes are linear and differ negligibly. In the region where $\varepsilon_3'<0$ and $|\varepsilon_3'|\gg\varepsilon_3''$, a ''metallic'' reflection effect occurs at the interface between the waveguide layer and the cover and the mode propagating in the structure penetrates slightly into the cover layer, reducing its damping. This region corresponds to frequencies $\nu=0.75$–$0.78\ \mu\text{m}^{-1}$. Another characteristic of these curves is that they reveal a frequency range in which the damping of the TE_0 mode exceeds that of the TM_0 mode. The frequency position of the mode absorption peaks is

mainly determined by the thickness of the cover layer.

Figure 3 shows the distribution of the mode energy density over the cross section of the waveguide structure, defined by $|\mathscr{F}_y|^2$ for the TE_0 and TM_0 modes (a, b). The thicknesses of the waveguide and cover layers were taken as $L_2=4\ \mu$m and $L_3=0.2\ \mu$m. Dependences were plotted for the frequencies $\nu=0.722$, 0.724, 0.725, and $0.750\ \mu\text{m}^{-1}$ (curves *1–4*, a) and 0.725, 0.731, 0.732, and $0.733\ \mu\text{m}^{-1}$ (curves *1–4*, b). It can be seen from Fig. 3a that at the beginning of this frequency range the function $|\mathscr{F}_y|^2$ has one peak in the waveguide layer and one peak in the cover layer. As the frequency increases, the peak in the cover layer increases while that in the waveguide layer decreases. An analysis of these curves suggests that maximum mode absorption occurs when the field distribution is such that the maximum of the function $|\mathscr{F}_y|^2$ occurs at the interface between the waveguide and cover layers. In this case, the fraction of the mode energy flux in the absorbing cover layer reaches a maximum. Minimum mode absorption will thus correspond to the field configuration for which this function has a minimum at the interface between the cover and waveguide layers. A further increase in frequency causes a drop in the maximum and shifts it into the cover layer. For the TM_0 mode the function $|\mathscr{F}_y|^2$ is plotted for frequencies lower than its frequency of conversion to the cover layer mode ($\nu_s\approx 0.732\ \mu\text{m}^{-1}$). As the frequency approaches ν_s, the energy maximum shifts toward the boundary with the cover layer and increases sharply. The localization of the mode field also increases here and the fraction of the mode energy in the waveguide layer increases. At frequencies corresponding to negative values of ε_3' the field of the TE and TM modes decays monotonically, almost exponentially, in the cover layer (Fig. 3a, curve *4*), which ensures relatively low mode absorption.

This analysis has shown that the proposed type of waveguide is potentially useful from the point of view of increasing its functional capabilities when used as a tunable source of laser radiation.

[1] M. M. Vekshin, V. A. Nikitin, and N. A. Yakovenko, Pis'ma Zh. Tekh. Fiz. **24**(6), 35 (1998) [Tech. Phys. Lett. **24**, 222 (1998)].
[2] R. Carson and T. Batchman, Appl. Opt. **29**, 2769 (1990).
[3] R. Carson, Proc. SPIE **835**, 18 (1987).
[4] A. I. Voronko, G. A. Nemova, and G. N. Shkerdin, Radiotekh. Elektron. (Moscow) **35**, 644 (1990).
[5] J. Stiens, R. Vounckx, I. Veretennicoff *et al.*, J. Appl. Phys. **81**, 1 (1997).
[6] A. M. Shutyĭ, D. I. Sementsov, and D. G. Sannikov, Radiotekh. Elektron. (Moscow) **44**(3), 1 (1999).

Translated by R. M. Durham

Unstrained epitaxial $In_xGa_{1-x}As$ films obtained on porous GaAs

F. Yu. Soldatenkov, V. P. Ulin, A. A. Yakovenko, O. M. Fedorova, S. G. Konnikov, and V. I. Korol'kov

A. F. Ioffe Physicotechnical Institute, Russian Academy of Sciences, St. Petersburg
(Submitted July 9, 1999)
Pis'ma Zh. Tekh. Fiz. **25**, 15–20 (November 12, 1999)

Epitaxial layers of InGaAs solid solutions were grown on porous GaAs(100) substrates by liquid-phase epitaxy. A comparison between the compositions and thicknesses of these epitaxial layers with those of layers obtained under the same conditions on normal monolithic GaAs substrates suggests that the crystallization of epitaxial layers on porous substrates may be considered as the growth of free unstrained films. © *1999 American Institute of Physics.* [S1063-7850(99)00411-5]

The use of porous III–V single crystals as substrates for epitaxial growth opens up new possibilities for radically reducing the level of mechanical stresses and the density of relaxational crystal defects induced in heteroepitaxial structures by lattice mismatch between the materials being joined.[1]

In the present study, liquid-phase epitaxy was used to grow epitaxial layers of $In_xGa_{1-x}As$ solid solution, containing up to ~4% InAs, on monolithic (solid) and porous GaAs substrates. We used (100)-oriented, *n*-type GaAs substrates doped with tin to a concentration of $(1–2)\times10^{18}\,cm^{-3}$. Layers of porous material (5–20 μm) were obtained on these substrates by electrochemical etching in aqueous solutions containing HF, using a technique described in Ref. 1.

An In–Ga–As flux was used for the epitaxial growth processes at crystallization initiation temperatures of 710 °C. In order to suppress primary etching of the substrates on contact with the flux and penetration of the flux into the bulk of the porous material before this is brought in contact with the substrate, the initially saturated flux was supercooled to 5–7 °C. Figure 1 shows a photograph of a cleaved section through an as-grown $In_xGa_{1-x}As$ epitaxial layer on porous GaAs. It can be seen that for this type of pores and growth regime the flux does not penetrate into the bulk of the porous GaAs.

The results are presented in Table I.

The InAs content in the epitaxial layers of the solid solutions on the monolithic (x_m) and porous (x_p) substrates was determined from the position of the maximum of the photoluminescence edge band at 77 K and also from the results of an x-ray spectral microanalysis using a Camebax device (values in parentheses). For some samples the photoluminescence measurements were made both at the surface of the layer and near the substrate–layer interface after etching the substrate (samples 4b and 4a, respectively). The layer thicknesses (h_m for monolithic and h_p for porous substrates) were determined from the cleaved section by using optical and electron scanning microscopes. In Table I, $h_{rel}=h_p/h_m$ is the ratio of the layer thickness grown on a porous GaAs substrate to the layer thickness grown on a monolithic (solid) substrate, f is the relative lattice mismatch between the layer and the substrate, h_c is the critical thickness of a layer of given composition (calculated using the energy balance model[2]), and ΔT is the calculated minimum supercooling required to initiate epitaxial growth of an elastically deformed layer of solid solution pseudomorphic to the GaAs substrate (see below).

Figure 2 shows the relationship between the compositions of the layers grown on monolithic (x_m) and porous (x_p) media. Also plotted is the calculated relationship between the equilibrium compositions of a free-growing InGaAs crystal (x_f) and a strained InGaAs epitaxial layer (x_{st}) on a GaAs(100) substrate.

The dependence of x_{st} on x_f and the corresponding value of ΔT were calculated using concepts of minimizing the excess specific free energy (δG) of the system consisting of the initial phase in equilibrium with the $In_xGa_{1-x}As$ ($x=x_f$) solid solution and an $In_xGa_{1-x}As$ ($x=x_{st}$) solid solution with a tetragonally distorted crystal lattice pseudomorphic in the (100) plane to the GaAs substrate:[3]

$$\delta G=\left[\frac{RT}{2x_f(1-x_f)}-\Omega\right](x_{st}-x_f)^2+\frac{\lambda_{(100)}N_A a(\Delta a)^2}{4}x_{st}^2. \quad (1)$$

Here $\Omega=15145$ J/mole is the interaction parameter in the InAs–GaAs system (using the model of a regular solid solution), $\lambda_{(100)}$ is the reduced elastic modulus of the solid solution, $\lambda_{(100)}=C_{11}+C_{12}-2\cdot C_{12}^2/C_{11}$, where C_{ij} are the matrix elastic moduli of the layer (all the numerical values of the parameters are taken from Ref. 4), N_A is Avogadro's number, a is the lattice constant of the solid solution, Δa is the difference between the lattice constants of the unstrained layer and the substrate, R is the universal gas constant, and T is the temperature in kelvin.

The first term of the sum takes into account the change in the chemical component of the free energy of the system caused by the composition of the solid solution varying from the equilibrium value. The second term is the specific mechanical energy of the elastically strained layer on the

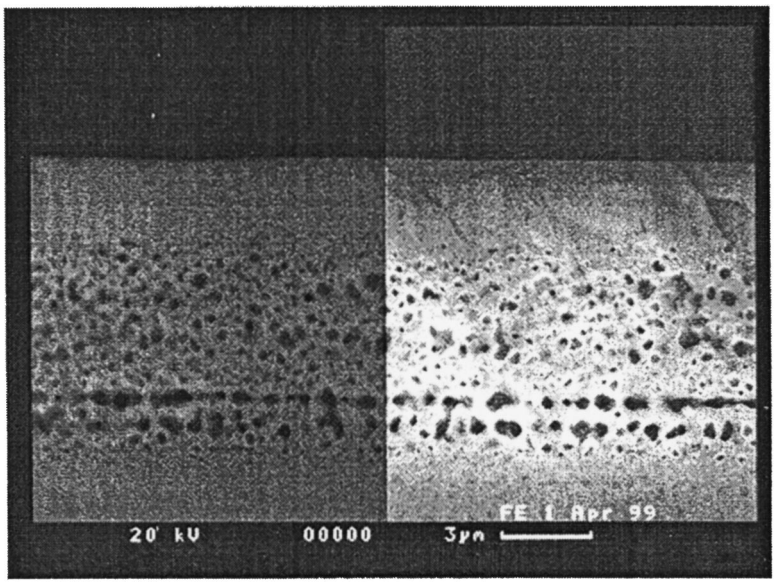

FIG. 1. Epitaxial $In_xGa_{1-x}As$ layer on a porous substrate. Photograph taken with an electron microscope, using reflected electrons (left-hand side) and reflected plus secondary electrons (right-hand side).

GaAs(100) substrate. Thus, we obtain from formula (1)

$$x_{st}=x_f\left[\frac{RT-2\Omega x_f(1-x_f)}{RT-\Omega x_f(1-x_f)+\frac{\lambda_{(100)}}{2}N_A a(\Delta a)^2 x_f(1-x_f)}\right]. \quad (2)$$

Using the dependence $x_{st}(x_f)$, we estimated the value of ΔT as $\Delta T=\delta G/R$ (see Table I) .

It can be seen from Table I that epitaxial layers grown on porous substrates systematically have a greater thickness and higher InAs content compared with layers on normal GaAs substrates. For epitaxial layers of thickness considerably less than the calculated critical thickness for the onset of relaxational defect formation in pseudomorphic films, these differences increase with increasing InAs concentration. However, during growth of epitaxial layers containing more than 3% InAs on a solid substrate, the composition changes with the content increasing toward the layer surface. In this case, the ratio of the layer thicknesses on the porous and solid substrates decreases. The thickness of the epitaxial layer for which these changes were observed is comparable with the critical thickness h_c for the initial layer composition calculated using the energy balance model[2] and is many times greater than the critical thickness calculated from the condition for mechanical equilibrium of the layer.[5] Consequently, these characteristics may be attributed to the onset of relaxation processes of the elastic stresses in the layer growing on the solid substrate. This then leads to a reduction in the free energy of the crystallizing solid solution and increases the effective supersaturation at the crystallization front.

Thus, the similarity between the crystallization condi-

TABLE I.

Experiment No.	Type of substrate	x_m, x_p, mol.%	h_m, h_p, μm	h_{rel}	$f\times10^3$	h_c, μm	ΔT, °C
1	Mon.	0.79(0.77)	1.8	1.22	0.56	80	0.25
	Por.	1.08(0.89)	2.2		–	–	–
2	Mon.	1.46(1.45)	1.3	1.69	1.05	21	0.9
	Por.	1.79(1.71)	2.2		–	–	–
3	Mon.	2.33	1.5	2.0	1.67	7.4	2.5
	Por.	2.88	3.0		–	–	–
4a	Mon.	3.35			2.41	3.3	5.8
b	Mon.	3.77	2.9	1.21			
	Por.	4.26	3.5		–	–	–

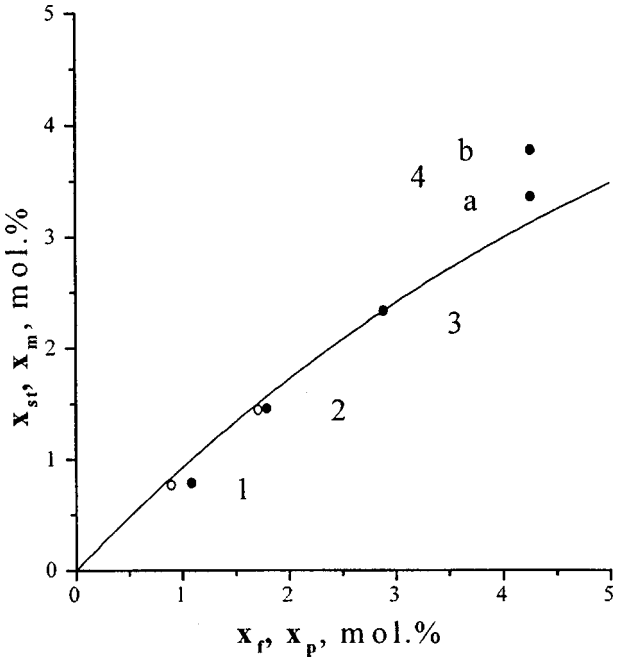

FIG. 2. The solid curve calculated using formula (2) gives the relationship between the compositions of $In_xGa_{1-x}As$ solid solutions under conditions of free growth (x_f) and epitaxial crystallization in the form of layers pseudomorphic to GaAs(100) (x_{st}). The experimental points reflect the correlation of the compositions for pairs of $In_xGa_{1-x}As$ layers grown in a single process from the same flux on porous (x_p) and monolithic (x_m) substrates (see Table I); the filled circles give data obtained by photoluminescence measurements and the open circles give the results of an x-ray spectral microanalysis.

tions achieved under liquid-phase epitaxy and the interphase equilibrium state made it possible to identify differences in the compositions and thicknesses of epitaxial layers induced thermodynamically by differences in their elastically deformed state. The differences observed for $In_xGa_{1-x}As$ layers grown from the same solution on porous and solid substrates indicate that even before the critical layer thickness is reached, the strains formed in the heterostructure are localized in the bulk of the porous substrate and the growth of the epitaxial layer on this substrate is almost the same as the growth of a free unstrained crystal.

To conclude, the authors would like to thank S. I. Troshkov, V. M. Busov, and T. B. Popova for assistance with the measurements and E. L. Portnoĭ for interest and assistance with this work.

[1] V. V. Mamutin, V. P. Ulin, V. V. Tret'yakov *et al.*, Pis'ma Zh. Tekh. Fiz. **25**(1), 3 (1999) [Tech. Phys. Lett. **25**, 1 (1999)].
[2] R. People and J. C. Bean, Appl. Phys. Lett. **47**, 322 (1985); **49**, 229 (1986).
[3] V. V. Voronkov, L. M. Dolginov, A. N. Lapshin, and M. G. Mil'vidskiĭ, Kristallografiya **22**, 375 (1977) [Sov. Phys. Crystallogr. **22**, 211 (1977)].
[4] V. V. Kuznetsov, P. P. Moskvin, and V. S. Sorokin, *Nonequilibrium Effects in Liquid-Phase Heteroepitaxy of Semiconducting Solid Solutions* [in Russian], Moscow (1991), 175 pp.
[5] J. W. Matthews and A. E. Blakeslee, J. Cryst. Growth **27**, 118 (1974).

Translated by R. M. Durham

Conversion of the polarization of an electromagnetic wave under cyclotron resonance in a two-dimensional electron system

V. V. Popov and T. V. Teperik

Institute of Radio Engineering and Electronics, Saratov Branch, Russian Academy of Sciences
(Submitted May 11, 1999)
Pis'ma Zh. Tekh. Fiz. **25**, 21–26 (November 12, 1999)

A theoretical analysis is made of the conversion of the polarization of an electromagnetic wave when cyclotron resonance is excited in a two-dimensional electron system. It is shown that the greatest conversion of the polarization can be achieved in the reflected wave. At high electron concentrations the effect remains very appreciable even in the presence of electron scattering. In this case, the wave polarization conversion effect can be used to obtain information on electron relaxation in a two-dimensional system. © *1999 American Institute of Physics.* [S1063-7850(99)00511-X]

Cyclotron resonance in two-dimensional (2D) electron systems has formed the subject of numerous experimental[1–5] and theoretical studies.[6–9] A submillimeter linearly polarized electromagnetic wave normally incident on a 2D electron system is usually used experimentally and the relative change in the total (for both orthogonal polarizations) coefficient of transmission of the wave power is measured under resonance conditions. Thus, the question of the conversion of the wave polarization does not arise. The conversion of the polarization of an electromagnetic wave under cyclotron resonance has also not yet been considered in any theoretical studies. However, it has been predicted that when cyclotron resonance is excited in a 2D electron system, the wave polarization conversion effect will increase substantially (resonantly). This suggests that this resonant polarization conversion effect may be used for diagnostics of the 2D electron system and to develop controllable polarization devices in the submillimeter range.

Bakunov and Zhukov[10,11] reported a theoretical analysis of the resonant conversion of electromagnetic radiation when transverse plasma oscillations are excited in a gyrotropic semiconducting film. The magnitude of this effect is proportional to the film thickness which substantially reduces the polarization conversion efficiency in extremely thin (including two-dimensional) electron layers. Unlike transverse plasma oscillations, electron cyclotron motion takes place in the plane of the electron system so that, in principle, constraints associated with the layer thickness should not arise.

We shall consider the case of a linearly polarized electromagnetic wave incident normally from medium *1* onto the surface of a 2D electron system at the interface between media *1* and *2* having relative permittivities ε_1 and ε_2. We shall assume that an external static magnetic field is directed normal to the plane of the 2D system from medium *1* to medium *2*.

We introduce the conversion efficiencies of the incident wave power in the form:

$$R_{pp}=\frac{P_{rp}}{P_{ip}}, \quad R_{sp}=\frac{P_{rs}}{P_{ip}},$$

$$T_{pp}=\frac{P_{tp}}{P_{ip}}, \quad T_{sp}=\frac{P_{ts}}{P_{ip}}, \tag{1}$$

where P_{ip} is the energy flux density of the incident wave, P_{rp} and P_{tp} are the energy flux densities of the reflected and transmitted waves, respectively, whose polarization is the same as that of the incident wave, P_{rs} and P_{ts} are the energy flux densities of the reflected and transmitted waves exhibiting linear polarization orthogonal to that of the incident wave. Quite clearly, the values of R_{sp} and T_{sp} have the meaning of the conversion efficiencies of the wave polarization.

Solving the Maxwell equations in media *1* and *2* with boundary conditions at the interface which take into account the response of a magnetoactive 2D electron plasma, yields the following expressions for the conversion efficiencies:

$$R_{pp}=\left|\frac{(\sqrt{\varepsilon_2}+Z_0\sigma_\perp)^2-\varepsilon_1+Z_0^2\sigma_\times^2}{(\sqrt{\varepsilon_1}+\sqrt{\varepsilon_2}+Z_0\sigma_\perp)^2+Z_0^2\sigma_\times^2}\right|^2,$$

$$T_{pp}=4\sqrt{\varepsilon_1\varepsilon_2}\left|\frac{\sqrt{\varepsilon_1}+\sqrt{\varepsilon_2}+Z_0\sigma_\perp}{(\sqrt{\varepsilon_1}+\sqrt{\varepsilon_2}+Z_0\sigma_\perp)^2+Z_0^2\sigma_\times^2}\right|^2,$$

$$R_{sp}=4\varepsilon_1\left|\frac{Z_0\sigma_\times}{(\sqrt{\varepsilon_1}+\sqrt{\varepsilon_2}+Z_0\sigma_\perp)^2+Z_0^2\sigma_\times^2}\right|^2,$$

$$T_{sp}=4\sqrt{\varepsilon_1\varepsilon_2}\left|\frac{Z_0\sigma_\times}{(\sqrt{\varepsilon_1}+\sqrt{\varepsilon_2}+Z_0\sigma_\perp)^2+Z_0^2\sigma_\times^2}\right|^2, \tag{2}$$

where $Z_0=120\pi\,\Omega$ is the wave impedance of free space,

$$\sigma_\perp=\sigma_0\frac{1-i\omega\tau}{(\omega_c\tau)^2+(1-i\omega\tau)^2},$$

$$\sigma_\times=-\sigma_0\frac{\omega_c\tau}{(\omega_c\tau)^2+(1-i\omega\tau)^2} \tag{3}$$

are the components of the conductivity tensor of a 2D electron plasma in a magnetic field. Here ω is the angular frequency of the wave, $\omega_c=eB_0/m^*$ is the cyclotron frequency, $\sigma_0=e^2N_s\tau/m^*$ is the dc conductivity of a 2D

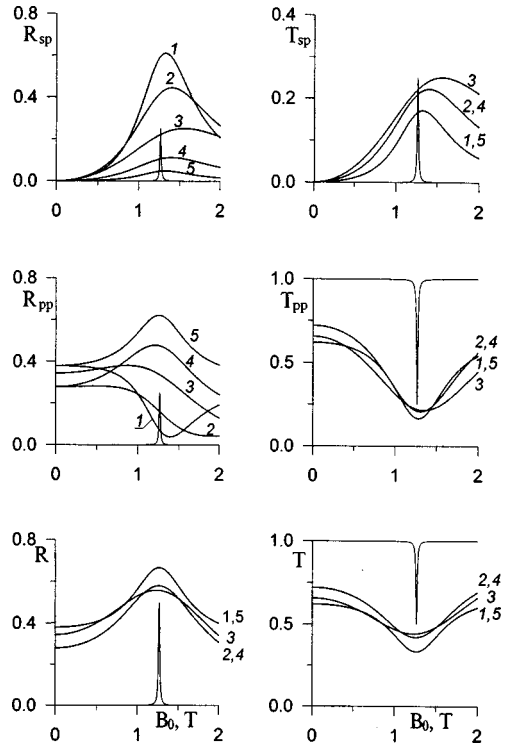

FIG. 1. Conversion efficiencies as a function of magnetic field at frequency $20\,\mathrm{cm}^{-1}$ for $1/\tau=0$, $N_s=3\times10^{12}\,\mathrm{cm}^{-2}$, $\varepsilon_2/\varepsilon_1$: 1/12 (*1*), 1/4 (*2*), 1/1 (*3*), 4/1 (*4*), and 12/1 (*5*). The fine solid curves give the corresponding dependences for $\varepsilon_1=\varepsilon_2=1$ and $N_s=3\times10^{10}\,\mathrm{cm}^{-2}$.

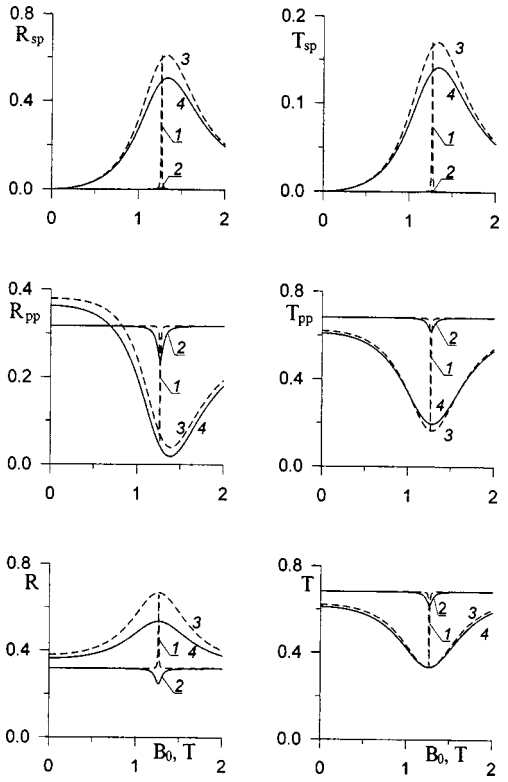

FIG. 2. As Fig. 1 for $\varepsilon_1/\varepsilon_2=1/12.8$ and $1/\tau, \mathrm{s}^{-1}$: 0 (*1, 3*) and 1×10^{11} (*2, 4*). N_s, cm^{-2}: 3×10^{10} (*1, 2*) and 3×10^{12} (*3, 4*).

electron system in the absence of an external magnetic field, e, m^*, N_s, and τ are the charge, effective mass, surface concentration, and phenomenological relaxation time of the electron momentum in the 2D system, respectively.

If we neglect electron scattering in the 2D system $(1/\tau\to0)$, the formulas (3) have a simpler form, and we can write explicit expressions for the external magnetic field $B_0=B_0^{\max}$ corresponding to maximum conversion of the wave polarization, and for the maximum efficiencies R_{sp} and T_{sp} (the positions of the R_{sp} and T_{sp} maxima coincide):

$$B_0^{\max}=\frac{m^*}{e}\sqrt{\frac{(\sqrt{\varepsilon_1}+\sqrt{\varepsilon_2})^2\omega^2+(e^2N_sZ_0/m^*)^2}{(\sqrt{\varepsilon_1}+\sqrt{\varepsilon_2})^2}}, \tag{4}$$

$$R_{\mathrm{sp}}^{\max}=\frac{\varepsilon_1}{(\sqrt{\varepsilon_1}+\sqrt{\varepsilon_2})^2}, \tag{5}$$

$$T_{\mathrm{sp}}^{\max}=\frac{\sqrt{\varepsilon_1\varepsilon_2}}{(\sqrt{\varepsilon_1}+\sqrt{\varepsilon_2})^2}. \tag{6}$$

At low concentrations N_s the second term in the numerator of the radicand in formula (4) may become considerably smaller than the first. In this case, the wave polarization undergoes maximum conversion when $\omega_c\simeq\omega$. As N_s increases, maximum polarization conversion shifts toward stronger magnetic fields.

Figure 1 gives the wave power conversion efficiencies as a function of the magnetic field for various surface electron concentrations in the 2D system, and various permittivity ratios of media *1* and *2*. It can be seen that as well as the shift of the polarization conversion maximum as N_s increases, the width of the resonance curves of the conversion efficiencies also increases. Note that the resonance curves of the total reflection $R=R_{\mathrm{pp}}+R_{\mathrm{sp}}$ and transmission coefficients $T=T_{\mathrm{pp}}+T_{\mathrm{sp}}$ show almost no shift (and simply become broader) as the surface electron concentration varies.

It follows from formulas (5) and (6) that the maximum polarization conversion efficiencies are determined only by the permittivity ratio of media *1* and *2*. For example, for $\varepsilon_1=\varepsilon_2$ we have $R_{\mathrm{sp}}^{\max}=T_{\mathrm{sp}}^{\max}=0.25$. The value of $R_{\mathrm{sp}}^{\max}$ increases appreciably if the electromagnetic wave is incident on the surface of the 2D system from the optically denser medium (see Fig. 1). In the opposite case, $R_{\mathrm{sp}}^{\max}$ decreases. At the same time $T_{\mathrm{sp}}^{\max}$ decreases as the permittivity of either medium increases, but does not change when ε_1 and ε_2 are exchanged. Consequently the most efficient conversion of the polarization may be obtained in the reflected wave.

Figure 2 illustrates the influence of electron scattering in a 2D system on the magnitude of the wave polarization conversion effect. For the calculations we used structure parameters similar to the real parameters of 2D electron systems in semiconducting GaAs/AlGaAs heterostructures. At low concentrations N_s, electron scattering almost completely suppresses the polarization conversion effect, whereas at high concentrations the effect remains appreciable. Note that the total transmission coefficient T, usually used in experiments to study cyclotron resonance, depends weakly on the relaxation parameter $1/\tau$ at high electron concentrations. In this case, polarization measurements in the transmitted wave are more suitable for studying electron relaxation processes.

This work was supported financially by the Federal Target Program ''State Support for the Integration of Higher Education and Fundamental Science for 1997–2000,'' Project No. 696.3.

[1] G. Abstreiter, J. P. Kotthaus, J. F. Koch, and G. Dorda, Phys. Rev. B **14**, 2480 (1976).
[2] Z. Schlesinger, S. J. Allen, J. C. M. Hwang *et al.*, Phys. Rev. B **30**, 435 (1984).
[3] M. J. Chou, D. C. Tsui, and G. Weimann, Phys. Rev. B **37**, 848 (1988).
[4] S. D. Suchalkin, Yu. B. Vasil'ev, and Yu. L. Ivanov, Fiz. Tekh. Poluprovodn. **27**, 2078 (1993) [Semiconductors **27**, 1141 (1993)].
[5] L. Van Bockstal, M. Mahy, A. De Keyser *et al.*, Physica B **211**, 466 (1995).
[6] T. Ando, J. Phys. Soc. Jpn. **38**, 989 (1975).
[7] C. S. Ting, S. C. Ying, and J. J. Quinn, Phys. Rev. Lett. **36**(4), 215 (1976).
[8] R. Lassnig and E. Gornik, Solid State Commun. **47**, 959 (1983).
[9] C. Kallin and B. I. Halperin, Phys. Rev. B **31**, 3635 (1985).
[10] M. I. Bakunov and S. N. Zhukov, Pis'ma Zh. Tekh. Fiz. **16**(1), 69 (1990) [Sov. Tech. Phys. Lett. **16**, 30 (1990)].
[11] M. I. Bakunov and S. N. Zhukov, Radiotekh. Elektron. (Moscow) **36**, 1284 (1991).

Translated by R. M. Durham

Sealed efficient excilamps excited by a capacitive discharge

M. I. Lomaev, V. S. Skakun, É. A. Sosnin, V. F. Tarasenko, and D. V. Shitts

Institute of High-Current Electronics, Siberian Branch of the Russian Academy of Sciences, Tomsk
(Submitted June 15, 1999)
Pis'ma Zh. Tekh. Fiz. **25**, 27–32 (November 12, 1999)

The development of sealed XeCl ($\lambda \sim 308$ nm), KrCl ($\lambda \sim 222$ nm), and XeI ($\lambda \sim 253$ nm) excilamps excited by a capacitive rf discharge is reported. It is shown that highly efficient emission of exciplex molecules is achieved under capacitive discharge excitation and the emitter has a simple design. An average emission power of 3 W was obtained with a ~12% efficiency and the lifetime of the sealed excilamps was longer than 1000 h. © *1999 American Institute of Physics.* [S1063-7850(99)00611-4]

1. Increasing interest is now being shown in the development of new sources of spontaneous ultraviolet and vacuum ultraviolet radiation, especially excilamps,[1–14] and their application in various fields of science and technology.[11,14] The highest efficiencies for XeCl ($\lambda \sim 308$ nm) and KrCl ($\lambda \sim 222$ nm) excilamps are achieved at low working mixture pressures and low specific glow-discharge excitation powers.[2–13] The highest efficiencies were obtained in the cw regime or under pulsed excitation using long pulses (having durations of tens of microseconds or longer) in a positive low-pressure glow-discharge column[7] or in a subnormal glow discharge (high-voltage glow discharge).[10] However, in sealed glow-discharge excilamps the working mixture pressure is limited because of contact between the chlorine-containing active mixture and the electrodes, whose temperature rises appreciably during operation, especially in excilamps having a high average radiation power. For example, for an excilamp having an average radiation power of 100 W and stainless steel electrodes, the mixture lifetime did not exceed 1 h and this needed to be replaced at intervals.[11] By reducing the average radiation power by more than an order of magnitude, using a ballast volume, and nickel electrodes, Golovitskiĭ and Kan[3] obtained an active mixture lifetime of 100 h which is also clearly inadequate for many practical applications. However, we know that in elevated-pressure lamps (~1 atm) excited by a barrier discharge in which the working mixture is only in contact with the quartz flask of the excilamp, it is possible to obtain a working mixture lifetime of more than 1000 h (Ref. 14), but then the emission efficiency is generally four times lower than that under excitation by a subnormal glow discharge.

In the present paper we report for the first time the development of efficient sealed, cylindrical, low-pressure excilamps excited by an rf capacitive discharge in which the working-mixture lifetime is more than 1000 h and the emitter has a very simple design. Note that a barrier discharge is also a type of capacitive discharge and that a cylindrical geometry was used earlier to pump low-pressure CO_2 lasers using a capacitive discharge.

2. Figure 1 shows the design of the emitter for an excilamp excited by a capacitive discharge. We used cylindrical tubes between 2 and 4 cm in diameter and up to 40 cm long. The electrodes were positioned on the outer surface of the tubes, between 2 and 38 cm apart and their length could be varied between 1 and 19 cm.

The working mixtures were excited by three sinusoidal pulse generators having powers of 20, 35, and 55 W and a pulse repetition frequency of 22 kHz. The amplitude of the voltage could be regulated for gas discharge loads with the same working mixture composition, and did not exceed 4 kV.

The current and voltage were measured using an Ohmic shunt and a voltage divider from which the signals were fed to an S8-17 dual-beam oscilloscope. The average radiation power in a given spectral range was determined using an FÉK-22 SPU vacuum photodiode with known spectral sensitivity in the visible and ultraviolet, from which the signal was fed to a pulse voltmeter or S8-17 oscilloscope.

3. The following results were obtained. In mixtures of rare gases with halides (chlorine and iodine in the present study) it was easy to produce an rf volume discharge at low mixture pressures, emitting highly efficiently on $B–X$ transitions of exciplex molecules. The optimum pressure depended on the mixture composition, the distance between the electrodes, and the diameter, and was between fractions and several torr, which coincides with the range of operating pressures in glow-discharge excilamps.[2–13] The ratios of the working mixture components for chlorine-containing mixtures were also similar to those used in a glow discharge. Figure 2 gives the radiation power and efficiency as a function of the product of the pressure and the interelectrode gap

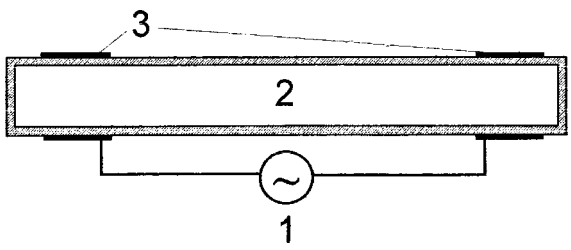

FIG. 1. Design of rf capacitive-discharge emitter: 1 — excitation generator, 2 — volume containing working mixture, and 3 — electrodes.

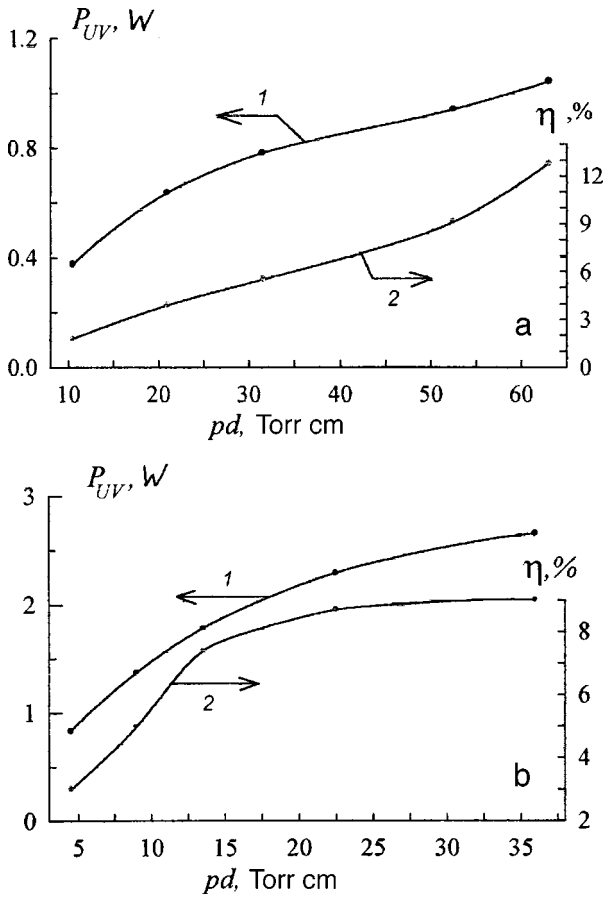

FIG. 2. Average radiation power and efficiency as a function of the product of the mixture pressure and the interelectrode gap for KrCl (a) and XeCl (b) excilamps: *1*—Kr:Cl_2=8:1 mixture at 4.2 Torr, *2*—Xe:Cl_2=8:1 mixture at 1.8 Torr.

(pd) for XeCl* and KrCl* exciplex molecules. It can be seen that the emission efficiency is similar to that obtained for glow discharge excitation. The duration of the emission pulse also depends on the composition and mixture pressure, the interelectrode gap, and the working voltage, the electrode area, and the diameter of the quartz tube. For example, for an XeI excilamp 4 cm in diameter with an interelectrode gap of 9 cm, and a mixture pressure of 10 Torr the duration of isolated radiation pulses corresponded to each half-period of the discharge current and was $\sim 20\ \mu$s.

The spectral characteristics of the XeCl and KrCl excilamp radiation are similar to those obtained under glow discharge excitation. The width of the emission band of the XeI* molecules ($\lambda \sim 253$ nm) was 2 nm and also corresponded to that obtained by us in a glow discharge. However, the emission efficiency of the XeI* molecules was approximately between five and ten times lower both for capacitive discharge excitation and for glow discharge excitation.

The main advantages of capacitive discharge excitation compared with a glow discharge are the simple emitter design, the absence of any contact between the working mixture and the electrodes, and the substantial increase in the service life of the sealed excilamps. Tests, which are still ongoing, have shown that the service life of the mixture in a sealed excilamp exceeds 1000 h.

Compared with barrier discharge excitation, a capacitive discharge can provide more uniform excitation (no isolated filaments), produce narrower emission lines, and couple energy more efficiently into the working mixture at low pressure so that higher efficiencies of ultraviolet emission can be obtained from the ''rosette.''

4. To conclude, we note that sealed cylindrical low-pressure XeCl ($\lambda \sim 308$ nm), KrCl ($\lambda \sim 222$ nm), and XeI ($\lambda \sim 281$ nm) excilamps excited by an rf capacitive discharge have been developed for the first time using an emitter of extremely simple design. High emission efficiencies in the ultraviolet ($\sim 12\%$) and high average radiation powers (~ 3 W in a 250 cm^3 working volume) were achieved using XeCl and KrCl excilamps. The lifetime of the sealed XeCl and XeI excilamps was longer than 1000 h.

[1] B. A. Koval', V. S. Skakun, V. F. Tarasenko *et al.*, Prib. Tekh. Éksp. No. 4, 244 (1992).
[2] A. P. Golovitskiĭ, Pis'ma Zh. Tekh. Fiz. **18**(8), 73 (1992) [Sov. Tech. Phys. Lett. **18**, 269 (1992)].
[3] A. P. Golovitskiĭ and S. N. Kan, Opt. Spektrosk. **75**, 604 (1993) [Opt. Spectrosc. **75**, 357 (1993)].
[4] A. N. Panchenko, É. A. Sosnin, V. S. Skakun *et al.*, Pis'ma Zh. Tekh. Fiz. **21**(21), 47 (1995).
[5] A. M. Boichenko, A. N. Panchenko, V. F. Tarasenko *et al.*, Laser Phys. No. 5, 1112 (1995).
[6] M. I. Lomaev, A. N. Panchenko, V. S. Skakun *et al.*, Opt. Atmos. Okean. **9**(2), 199 (1996).
[7] A. M. Boĭchenko, A. N. Panchenko, V. F. Tarasenko *et al.*, Kvant. Elektron. (Moscow) **23**, 417 (1996).
[8] A. N. Panchenko, É. A. Sosnin, and V. F. Tarasenko, Zh. Tekh. Fiz. **67**(4), 78 (1997) [Tech. Phys. **42**, 394 (1997)].
[9] A. P. Golovitskiĭ and S. V. Lebedev, Opt. Spektrosk. **82**, 251 (1997) [Opt. Spectrosc. **82**, 227 (1997)].
[10] A. N. Panchenko and V. F. Tarasenko, Opt. Spektrosk. **84**, 389 (1998) [Opt. Spectrosc. **84**, 337 (1998)].
[11] M. I. Lomaev, A. N. Panchenko, V. S. Skakun *et al.*, Laser Part. Beams **15**, 241 (1998).
[12] M. I. Lomaev, A. N. Panchenko, É. A. Sosnin *et al.*, Zh. Tekh. Fiz. **68**(2), 64 (1998) [Tech. Phys. **43**, 192 (1998)].
[13] A. N. Panchenko, E. A. Sosnin, and V. F. Tarasenko, Opt. Commun. **161**, 249 (1999).
[14] E. Arnold, R. Dreiskemper, and S. Reber, in *Proceedings of the Eighth International Symposium on Science and Technology of Light Sources (LS-8)*, Graifswald, Germany, 1998, IL 12, pp. 90-98.

Translated by R. M. Durham

Stability of a laser cavity with a two-mirror multipass system

M. Yu. Kantor

A. F. Ioffe Physicotechnial Institute, Russian Academy of Sciences, St. Petersburg
(Submitted June 7, 1999)
Pis'ma Zh. Tekh. Fiz. **25**, 33–38 (November 12, 1999)

An investigation is made of the stability of a laser cavity in which one of the nontransmitting mirrors is a multipass system consisting of two spherical mirrors. The stability of the cavity depends strongly on the number of passes of the beam in the multipass system, the configuration of the mirrors, and the constriction of the beam entering the system. A stable cavity configuration ensures low diffraction losses in the system and efficient lasing. © *1999 American Institute of Physics.* [S1063-7850(99)00711-9]

Cavities with a multipass system are widely used in laser engineering. In particular, they can create a substantial difference in the radiation energy circulating in the multipass system and passing through the laser active element, which appreciably increases the capabilities of diagnostics systems based on laser radiation scattering.[1] The low radiation losses in a cavity required for laser operation can be achieved when this configuration is stable. In the present study, the stability of a cavity with a two-mirror multipass system (Fig. 1) is examined. This system consists of two spherical mirrors *0* and *1* having radii of curvature $R_{0,1}$, forming a multipass system, a focusing objective *2*, and a nontransmitting mirror *4*. The laser active element *3* is positioned between the objective and the nontransmitting cavity mirror.

Natural oscillation modes propagate in a stable cavity, i.e., radiation beams which conserve their transverse dimensions, shape, and wavefront curvature after a complete round trip. For the cavity under study this property is satisfied in any common cross section of the beams entering and leaving the multipass system.

Let us assume that the multipass system is aligned such that after N passes, the outgoing beam is directed toward the mirror *4*. In order to determine the stability of the cavity, we need to find the relationship between the transverse dimensions of the beams entering and leaving the multipass system. In the paraxial approximation, the transverse coordinates and angles of inclination of the beams in any cross sections are linearly related using the ray matrix (see, for example, Ref. 2).

In order to calculate this matrix, we introduce a coordinate system whose origin coincides with the center of the multipass system and the z axis is directed along the cavity axis away from the nontransmitting mirror. We shall call the center of the multipass system the position of the constriction of the natural modes of a stable cavity formed by mirrors *0* and *1* located at distances $L(1\pm\delta)/2$ from these mirrors, respectively. Here L is the distance between the mirrors and $\delta=(R_1-R_0)/(R_1+R_0-2L)$ (Ref. 2). This definition is also convenient for the position of the mirrors in an unstable cavity although in this case, it does not have such a clear meaning. The matrix describing propagation of the beam from the center of the multipass system and back as a result of a single reflection from each mirror has the form:

$$M=\begin{pmatrix} 2\eta-1 & 2R\eta(1-\eta) \\ -\dfrac{2}{R} & 2\eta-1 \end{pmatrix}, \tag{1}$$

$$R=R_0R_1/(R_0+R_1-2L),$$

$$\eta=(1-L/R_0)/(1-L/R_1).$$

The matrix for n passes is the product of n matrices (1). For $0<2\eta-1<1$ this matrix is obtained using the Silvester theorem:[2]

$$M''=\begin{pmatrix} \cos 2n\phi & \dfrac{R}{2}\sin 2\phi \sin 2n\phi \\ -\dfrac{2}{R}\dfrac{\sin 2n\phi}{\sin 2\phi} & \cos 2n\phi \end{pmatrix}. \tag{2}$$

Here we have $\cos 2\phi=2\eta-1$, $0\leqslant\phi\leqslant\pi$. By making the substitutions $\phi=i\Phi$ and $\phi=i\Phi+\pi/2$ the matrix (2) is generalized to the cases $\eta>1$ and $\eta<0$, respectively:

$$M''=\sigma''\begin{pmatrix} \cosh 2n\Phi & \sigma\dfrac{R}{2}\sin 2\Phi\sinh 2n\Phi \\ -\sigma\dfrac{2}{R}\dfrac{\sinh 2n\Phi}{\sinh 2\Phi} & \cosh 2n\Phi \end{pmatrix}. \tag{2a}$$

Here we have $\sigma=\pm 1$, $\sigma\eta>0$, and $2\Phi=\operatorname{arcosh}(|2\eta-1|)$. The matrix (2) is used as the basis to calculate the matrix for beam propagation from point z_0 to point z after $N=2n+2$ passes between the mirrors:

$$P=\begin{pmatrix} AB \\ CD \end{pmatrix}$$

$$=\sigma''\begin{pmatrix} (c+\Delta s) & -\sigma\rho[(\Delta_0+\Delta)c+(\Delta\Delta_0\pm 1)s] \\ -\sigma s/\rho & (c+\Delta_0 s) \end{pmatrix}, \tag{3}$$

$$\Delta=z/\rho, \quad \Delta_0=z_0/\rho.$$

The plus sign corresponds to the cases $\eta>1$ and $\eta<0$, for which c, s, and ρ have the form:

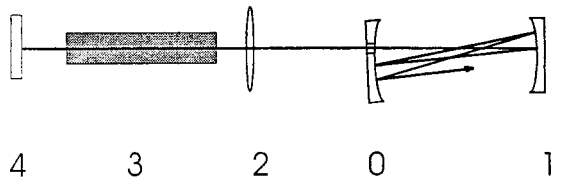

FIG. 1.

$$c=(\sigma R_0\cosh N\Phi+R_1\cosh(N-2)\Phi)/(R_0+R_1-2L),$$

$$s=(\sigma R_0\sinh N\Phi+R_1\sinh(N-2)\Phi)/(R_0+R_1-2L),$$

$$\rho=0.5\sigma R\sinh 2\Phi.$$

For the case $0<\eta<1$ the hyperbolic functions in these expressions are replaced by circular functions of ϕ. If the beam constriction is located at the point z_0, the radius ω_0 of the dominant radiation mode at the wavelength λ is determined using the $ABCD$ law[2] $\pi\omega_0^2=\lambda\sqrt{-B/C}$, where the elements of the matrix (3) are taken at $z=z_0$. From this we find:

$$\left(\frac{\pi\omega_0^2}{\lambda\rho}\right)^2=\pm 1-\Delta_0^2-2\Delta_0\frac{c}{s}. \tag{4}$$

Here the positive sign corresponds to $0\leqslant\eta\leqslant 1$. A positive right-hand side of Eq. (4) is the main necessary condition for cavity stability. The additional constraint that the wavefront curvature of the outgoing beam from the multipass system should coincide with the curvature of the reflecting surface of the mirror *4* at this mirror is easily satisfied by correctly selecting the objective and nontransmitting mirror. For a cavity with a plane mirror *4* and an objective having the focal length f the spot radius of the dominant mode ω_a on the rear mirror is given by:

$$\omega_a=\omega_0\sqrt{\frac{(S_a-f)}{(S_c-f)}}. \tag{5}$$

Here S_a and S_c are the distances between the lens and mirror *4* and the constriction of the beam entering the multipass system. In this case, the additional constraint for stability of the cavity is that the radicand in expression (5) is positive.

We represent formula (4) graphically as the dependence of $a_0=\pi\omega_0^2/\lambda R_1$ on L/R_1 and $z_0(R_1)$. For $a_0\ll 1$ this quantity is the ratio of the dimensions of the input beam at the constriction z_0 and at mirror *1* for all transverse cavity modes. Figure 2 gives the value of a_0 in the region of cavity stability for $R_0=R_1$, $N=4$ (a) and $N=14$ (b). The region of stability (4) for two passes lies between the two sloping lines. It can be seen how strongly the cavity stability and thus the lasing mode depends on N, L, and z_0. For a particular configuration of cavity elements lasing is determined by competition between modes for which the position of the input beam constriction differs. The laser active element has an appreciable influence on the mode selection, especially

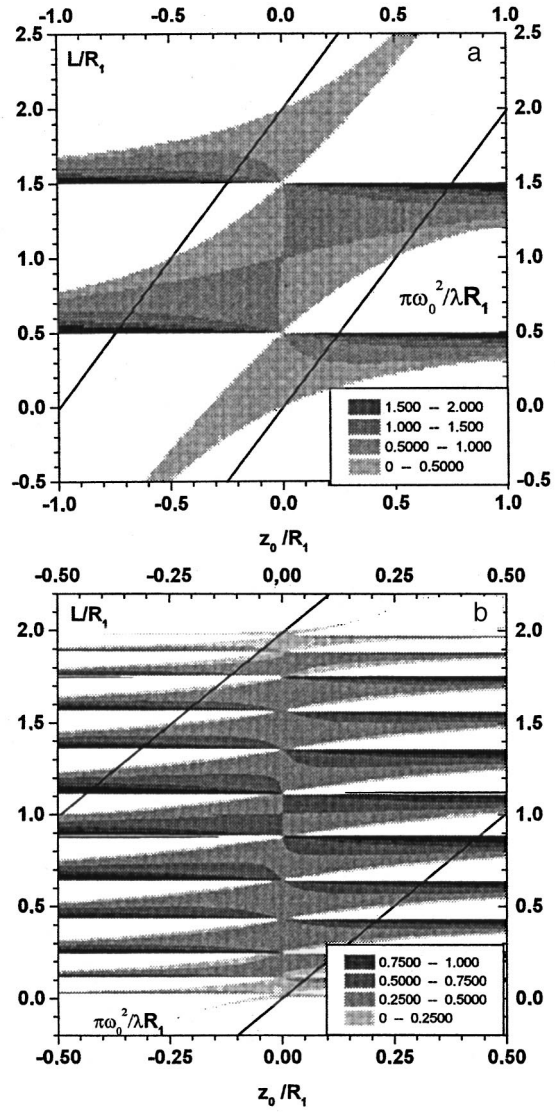

FIG. 2.

when its optical quality limits the divergence of the outgoing radiation. Leaving aside these important issues in the present study, we merely note that an optimally aligned cavity with a multipass system ensures low radiation losses over a large number of passes[3] and can increase the probing energy for an object positioned between the mirrors of the multipass system by more than two orders of magnitude compared with the same laser without a multipass system.

This work was supported by RFBR Grant No. 97-02-18084.

[1] M. Yu. Kantor and D. V. Kuprienko, Pis'ma Zh. Tekh. Fiz. **23**(8), 65 (1997) [Tech. Phys. Lett. **23**, 321 (1997)].
[2] H. Kogelnik and T. Li, Appl. Opt. **5**, 1550 (1966).
[3] M. Yu. Kantor and D. V. Kouprienko, Rev. Sci. Instrum. **70**, 780 (1999).

Translated by R. M. Durham

Heat exchange processes near the boundary of a film boiling nucleus

M. O. Lutset

S. S. Kutateladze Institute of Thermophysics, Siberian Branch of the Russian Academy of Sciences, Novosibirsk

(Submitted April 14, 1999)
Pis'ma Zh. Tekh. Fiz. **25**, 39–46 (November 12, 1999)

Results are presented of an experimental investigation of the change in temperature, heat flux to the liquid, and rate of displacement of the isotherms near a film boiling nucleus propagating over a plane surface. The experiment was carried out in a liquid nitrogen bath at atmospheric pressure on the saturation line. The heater was a sapphire plate 1.2 mm thick having a heat transfer surface area of $77\times 22\,\mathrm{mm}^2$. The following facts were established: 1) near the boundary of the film boiling nucleus a new heat exchange mechanism takes place caused by the instability of the liquid microlayer; 2) the maximum heat flux to the liquid is considerably greater than the critical heat flux; 3) the vapor film in the film boiling region grows gradually with increasing distance from the boundary, i.e., there is a smooth transition in terms of heat exchange intensity before the equilibrium film boiling level is reached. © *1999 American Institute of Physics.* [S1063-7850(99)00811-3]

In technology-based catastrophes and other transient processes, nonuniform, rapidly time-varying temperature distributions are frequently encountered at a liquid-cooled heat-transfer surface, leading to the appearance of new heat transfer laws. One example of such as transition is the evolution of a nucleate boiling crisis over the entire surface from a local nucleus covered with a vapor film. This is usually modeled by a switching autowave[1] using the one-dimensional heat-conduction equation:

$$SC(T)\partial T/\partial t=\nabla(S\lambda(T)\nabla T)+P(W-Q). \qquad (1)$$

Here $C(T)$ is the specific heat of the heater material calculated per unit volume, λ is its thermal conductivity, $W(T)$ and $Q(T)$ are the densities of heat release and heat removal at the heater surface, respectively, and S and P are the area and cooled perimeter of the cross section orthogonal to the direction of propagation of the autowave. Estimates and measurements[1] indicate that the wave velocity V is very low (of the order of centimeters per second). On this basis, the dependence of the heat flux Q to the liquid on the heater temperature T is usually assumed to be quasisteady-state and is calculated using steady-state boiling theories.[2] However, in Ref. 3 the present author indicated that there is a strict relationship between the heat exchange intensity in the transient regime and the wave velocity for limiting cases, and in Ref. 4 the author put forward data to suggest that heat exchange near the boundary of a film boiling nucleus exhibits significant transient characteristics. No other studies have considered the dependence $Q(T)$.

Here we present results of an experimental investigation of $Q(T)$.

The experiments were carried out using a liquid nitrogen tank at atmospheric pressure on the saturation line. The heater was a sapphire plate 1.2 mm thick having a heat transfer surface area of $77\times 22\,\mathrm{mm}^2$. The heat-transfer surface was oriented horizontally upward. A nichrome film 1000 Å thick was deposited on the lower side of the plate while a platinum film 800 Å thick was deposited on the upper side on which a pattern for the measuring system was fabricated by direct photolithographic techniques. This pattern consisted of two fragments. The first fragment was in the form of a meander measuring $11\times 20\,\mathrm{mm}^2$. The meander was positioned symmetrically relative to the long axis of the heat transfer surface and had a length of 11 mm along this surface. The edge of the meander was 3 mm from the edge of the plate. This meander served as a pulsed heater. Fourteen temperature sensors were then distributed along the long axis, which together with current and potential lines formed the second fragment of the pattern. All the sensors were distributed along the long axis, having dimensions of 1 mm perpendicular to the axis and 10 μm parallel to the axis. The current circuit consisted of connecting lines and series-connected sensors. A four-pass system was used to measure the resistance of the sensors. If we denote the sensors as si, numbering them from the pulsed heater, their distribution geometry is as follows: from the edge of the pulsed heater to $s1=10$ mm, $s1-s2=8$ mm, $s2-s3=7$ mm, $s3-s4=2$ mm, $s4-s5=2$ mm, $s5-s6=s6-s7=s7-s8=s8-s9=1$ mm, $s9-s10=2$ mm, $s10-s11=2$ mm, $s11-s12=5$ mm, $s12-s13=5$ mm, and $s13-s14=11$ mm. The temperature dependence of the sensor resistance was determined by special measurements. The measurement errors did not exceed 0.5%.

The sapphire plate was thermally insulated on all sides except for the heat transfer surface. The experiment was carried out as follows. First, steady-state nucleate boiling of the nitrogen on the plate was established by passing a direct current through the nichrome film. A current pulse was then applied to the pulsed heater which initiated a propagating film-boiling nucleus. An eight-channel computer-controlled analog-to-digital converter recorded the resistance of the sensors for 80 μs and then went over to the next measurement.

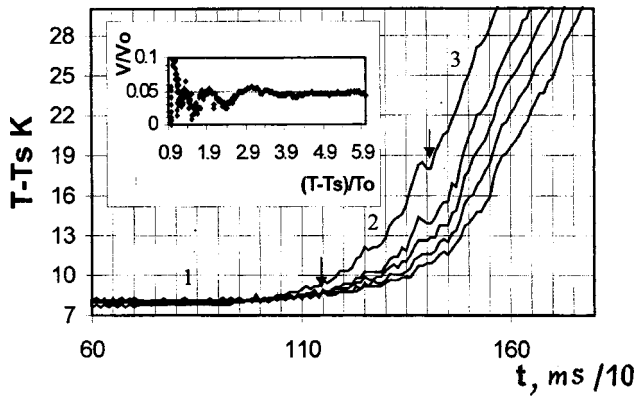

FIG. 1. Change in temperature in the wave from the readings of sensors in order from left to right: $s4$, $s5$, $s6$, $s7$, and $s8$. The inset shows the rate of displacement of the isotherms as a function of temperature: $W=7.5$ W/cm^2, $T_0=10$ K, $T_s=77.45$ K, and $V_0=x_0/t_0=20.7$ cm/s.

In this way we obtained the time variation of the temperature distribution along the axis of the heat-transfer surface.

The film boiling region was observed visually from the brightening of the heat transfer surface. The brightening boundary moved symmetrically relative to the longitudinal axis of the heater, undergoing flexural oscillations having a scale of 3–5 mm. Typical results of the measurements are plotted in Fig. 1. Three regions can be identified according to the intensity of the temperature fluctuations. For the $s4$ readings, the arrows indicate the boundaries of these regions. Region *1* has high frequencies and low oscillation amplitudes. Region *2* has low frequencies and large amplitudes and in region *3* the frequencies and amplitudes decrease. These regions can be seen even more clearly in Fig. 2 which plots the data in (T,y,t) coordinates where y is the distance between $s1$ and the measuring point. The two-dimensional plane gives some conception of the change in temperature along the heater axis with time. In addition to the coordinate grid, isotherms at 1 K intervals are also plotted on the surface. The heavy lines indicate the isotherms corresponding to temperatures of 9.75 K, 10 K, and 20 K. The position of the first arrow in Fig. 1 coincides with the gap between 9.75 K and 10 K not visible in Fig. 2 while the second corresponds to 20 K. Thus, these lines are the boundaries of the three regions isolated above. The configurations and densities of the isotherms in each region differ substantially, corresponding to the different processes of heat transfer to the liquid. The surface cross sections at constant time are shown in the inset. These characterize the positions of the wave temperature profiles along the axis of the heat transfer surface at various times. The data are approximated by third-degree polynomials with a confidence level of 1.

These data define the dependence $T=T(x,t)$ of the heat transfer surface along the longitudinal axis with an error not exceeding 0.5%. This dependence includes the steady-state wave motion, the temperature pulsations caused by flexural oscillations of the front, processes attributed to switching off the nichrome heater supply at a certain time (in order to avoid its overheating), and processes reflecting the finite length of the heater. The last two processes are easily eliminated and are not included in the analysis described subsequently.

The average motion of the front can be considered to be one-dimensional and may be described using Eq. (1). For convenience of the calculations this equation is reduced to the semidimensionless form:

$$Q=W-AC\partial T/\partial t+B[d\lambda/dT(\partial T/\partial x)^2+\lambda\partial^2 T/\partial x^2]. \qquad (2)$$

Here the dimensions of Q and W are unchanged. The notation for the other quantities also remains unchanged, but a notation with the subscript ''0'' is taken as the unit of measurement: $C_0=C(90\,\mathrm{K})$, $\lambda_0=\lambda(90\,\mathrm{K})$, $T_0=10$ K,

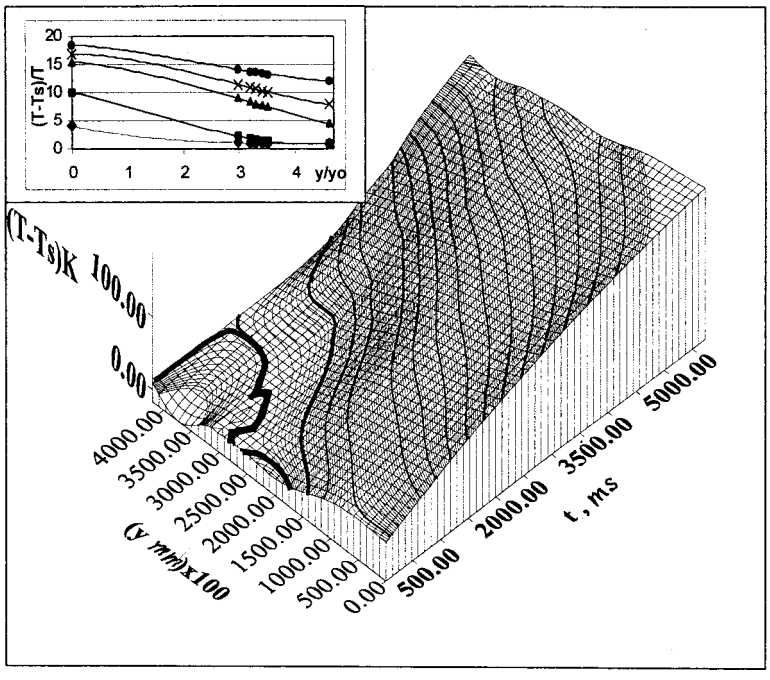

FIG. 2. Change in temperature shown in space and time. Coordinates of sensors along the axis (y, mm)$\times 100$: $s1$ — 0, $s4$ — 2700, $s5$ — 2900, $s6$ — 3000, $s7$ — 3100, $s8$ — 3200, and $s12$ — 4200. The inset shows the surface cross sections for $t=$ const in order from bottom to top: $t/t_0=2.55$, 40.76, 88.15, 104.97, 127.64, $t_0=0.044$ s.

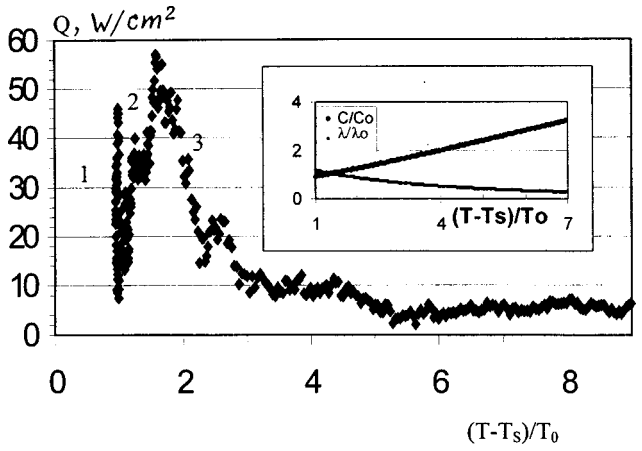

FIG. 3. Density of heat flux to the liquid as a function of temperature head. The inset gives the specific heat and thermal conductivity of sapphire as a function of temperature from data given in Refs. 6 and 7: $C_0 = 0.367$ J/cm^{3}K, $\lambda_0 = 7$ W/cmK.

$t_0 = \Delta C_0/\alpha_0$, $x_0 = (\lambda_0 S/\alpha_0 P)^{1/2}$, $A = \Delta C_0 T_0/t_0$, $B = \Delta\lambda_0 T_0/x_0^2$, where Δ is the plate thickness and $\alpha_0 = 1$ W/cm^{2}K.

The time derivative was calculated from the finite changes in temperature at neighboring times and the x-derivatives were calculated using a four-point formula (Ref. 5, p. 232). The dependences $C(T)$ and $\lambda(T)$ were taken from Refs. 6 and 7 and are illustrated in the inset to Fig. 3. The results of calculations using the $s5-s8$ data are plotted in Fig. 3 which clearly reveals three different heat exchange regions. In region *1* the temperature head varies slightly and corresponds to the value of 9–10 K achieved for the critical heat flux in nucleate boiling, but the maximum heat fluxes to the liquid are 2.2 times the critical value. In region *2* the heat exchange intensity is lower than that in the first but the heat fluxes are 2.8 times the critical level with a temperature head of 15.8 K. In the third region the heat exchange intensity falls sharply to values corresponding to film boiling.

The visual observations and the data plotted in Figs. 1 and 2, and 3 suggest that the motion of the boundary of the film boiling nucleus is pulsating. Thus, it is interesting to calculate the rate of displacement of the isotherms. Differentiating the expression $T[x(t),t] = \text{const}$ with respect to time, we obtain $V = dx/dt = -(\partial T/\partial t)/(\partial T/\partial x)$. The results of calculations using this formula are given in the inset to Fig. 1. The clearly defined autowave nature of the temperature variation in the wave is only observed in region *3* at temperature heads exceeding the critical overheating of the liquid, i.e., in the film boiling region. Region *1* is naturally identified with the nucleate boiling region and the boundary of this region is identified with the boundary of the film boiling nucleus. Nucleate boiling takes place on a wetted surface and film boiling on a dried surface. Near the boundary the liquid microlayer cannot be stable because of the increase in the temperature gradient. Thus, it explodes periodically, removing heat from the surface. This instability may be called temperature instability of the microlayer. This mechanism produces the maximum heat flux to the liquid and is typical of the second region. A similar effect was observed in Ref. 8 when studying the liquid wetting of an overheated surface. The termination of wetting causes a steep drop in the heat flux to the liquid but the thickness of the vapor film cannot instantaneously acquire the equilibrium value and grows gradually. Hence, in region *3* we observe a gradual decrease in Q to the level corresponding to steady-state film boiling.

To sum up, the following results have been established experimentally: 1) near the boundary of a film boiling nucleus a new heat exchange mechanism takes place as a result of the instability of the liquid microlayer; 2) the vapor film in region *3* grows gradually with increasing distance from the boundary, i.e., there is a smooth transition of heat exchange intensity between the second and third regions before the equilibrium film boiling level is reached; 3) the maximum heat flux to the liquid is considerably greater than the critical heat flux.

It follows from these observations that in order to describe the propagation of a boiling-regime switching autowave, the well-known equation[1] must be supplemented by another equation which controls the change in $Q = Q(T,t)$. Examples of the velocity pulsations of a traveling front for two diffusion processes with essentially different diffusion coefficients are well-known.[9]

This work was supported by the RFBR under Project No. 98-02-17920.

[1] S. A. Zhukov, V. V. Barelko, and A. G. Merzhanov, Int. J. Heat Mass Transf. **24**, 47 (1980).
[2] S. S. Kutateladze, *Principles of Heat Exchange Theory* (Nauka, Novosibirsk, 1970), 659 pp.
[3] M. O. Lutset, Pis'ma Zh. Tekh. Fiz. **24**(9), 21 (1998) [Tech. Phys. Lett. **24**, 338 (1998)].
[4] M. O. Lutset, *Heat Transfer 1998, Proceedings of the 11th International Heat Transfer Conference*, Kyongju, Korea, 1998, Vol. 2, pp. 315–317.
[5] I. S. Berezin and N. P. Zhidkov, *Computing Methods* (Pergamon Press, Oxford, 1965; Vol. 2, GIFML, Moscow, 1959, 464 pp.).
[6] I. G. Kozhevnikov and L. A. Novitskiĭ, *Handbook of Thermophysical Properties of Materials at Low Temperatures* (Mashinostroenie, Moscow, 1982), 328 pp.
[7] M. G. Holland, J. Appl. Phys. **33**(9), 270 (1962).
[8] T. Ueda, M. Inoue, Y. Iwata, and Y. Sogawa, Int. J. Heat Mass Transf. **26**, 401 (1983).
[9] V. A. Vasil'ev, Yu. M. Romanovskiĭ, and V. G. Yakhno, *Autowave Processes* (Nauka, Moscow, 1987), 240 pp.

Translated by R. M. Durham

Clusters in a pulsed free jet of a monosilane–argon mixture

R. G. Sharafutdinov, A. E. Zarvin, N. G. Korobeĭshchikov, V. Zh. Madirbaev, and S. Ya. Khmel'

Novosibirsk State University Institute of Thermophysics, Siberian Branch of the Russian Academy of Sciences, Novosibirsk

(Submitted July 6, 1999)
Pis'ma Zh. Tekh. Fiz. **25**, 47–51 (November 12, 1999)

An experimental investigation is made of condensation in a pulsed supersonic jet of a monosilane–argon gas mixture. In addition to silane-series (hydrogenated silicon) and argon clusters, mixed argon–silane complexes were observed for the first time and their conditions of formation in the jet were determined. The mass peak intensities of monomers and cluster ions were studied as a function of the initial pressure. Parameters of the flow transition to advanced condensation were determined. It is shown that condensation in the mixture jet at low initial pressures leads to the formation of monosilane clusters only whereas at high pressures, mixed monosilane–argon clusters are formed. © *1999 American Institute of Physics.* [S1063-7850(99)00911-8]

Recently gas jets have begun to be used to deposit thin films.[1] However, the deposition process may be influenced by condensation which takes place in a supersonic jet as the initial pressure P_0 increases.[2] It is therefore interesting to study cluster formation in a jet of monosilane-argon mixture used to produce silicon films.[1,3]

Condensation was investigated using the LÉMPUS complex of gasdynamic rigs at Novosibirsk State University using mass spectrometry of the molecular beam formed from a pulsed supersonic jet.[4] The duration of the gas pulse was 0.8 ms, which ensured a quasisteady-state flow regime. The measurements were made on the axis of the jet beyond a sonic nozzle having an exit cross section of diameter $d_0=1$ mm at a distance $x/d_0=175$ from the nozzle edge. High-purity argon and a $5\%SiH_4+95\%Ar$ mixture were used. The initial pressure P_0 was varied between 1 and 700 kPa.

We first investigated the condensation of pure argon, both to check the diagnostics procedures and for a comparison with condensation of the mixture. Figure 1 gives the amplitudes of the monomer and argon cluster peaks recorded in the molecular beam formed from the free argon jet, plotted as a function of the initial pressure. The arrow indicates the pressure at which a transition to advanced condensation is observed. These results agree satisfactorily with those obtained in a steady-state argon jet.[2] As a result of the release of condensation heat into the jet, ''drift'' of monomers into clusters, and possibly skimmer interaction, the intensity of the monomer signal stops increasing with increasing pressure after the onset of condensation and then decreases until the argon clusters begin to contribute to this signal as a result of fragmentation. The Ar_2^+, Ar_3^+, and Ar_4^+ ion signals occur predominantly as a result of the breakup of large clusters.

In the molecular beam extracted from a jet of SiH_4+Ar mixture, in addition to the peaks of Ar monomers and clusters, we observed silane monomers and clusters as well as peaks of mixed clusters of the type Ar_nSiH_x, where $n=1–4$ and $x=2–4$. Figure 2 shows the amplitudes of the mass peaks corresponding to Ar^+, SiH_3^+, $Si_2H_7^+$, Ar_2^+, $Ar_2SiH_2^+$, and $Si_3H_{11}^+$ ions plotted as a function of the initial pressure. The similarity between the dependences for the monomers and the clusters in jets of pure argon and mixtures indicates that condensation also takes place in the mixture jet. The recorded ions can be divided into three groups according to the behavior of these dependences: argon and monosilane monomers, silane-series clusters, and also clusters of argon and mixed argon–silane complexes. The dependences of the amplitudes of the argon and monosilane monomer signals on P_0 in the mixture jet agree qualitatively with the dependence of the monomer signal in a pure argon jet. The pressure at which advanced condensation begins in the mixture is shifted toward lower values and is approximately 20 kPa. Both curves have a clearly defined minimum at $P_0\sim 50$ kPa, after which the signal amplitudes increase as a result of fragmentation of the clusters. Consequently, the clusters contain not only monosilane but also argon. The enrichment of the molecular beam in clusters at high pressures changes the relationship between the argon and monosilane signals. The $Si_2H_7^+$ cluster ion signal appears at $P_0>15$ kPa, i.e., after the transition to advanced condensation in the jet. This signal evidently occurs as a result of the fragmentation of large clusters. The Ar_2^+ signal appears at $P_0>50$ kPa, i.e., considerably later than the silane-series dimers. There are also differences from the behavior of the Ar_2^+ dimer in a pure argon jet: first, it appears at higher pressure and second the first peak is almost completely absent in the mixture. Signals from Ar_3^+, Ar_4^+, and mixed clusters are only observed at high P_0 and behave like an argon dimer.

Thus, pure monosilane clusters are formed in the mixture jet at $P_0\sim 20$ kPa. As P_0 increases, they probably become condensation nuclei for Ar and, from $P_0\sim 40$ kPa, combined condensation of monosilane and argon takes place in the jet. At $P_0>40$ kPa signals from argon and argon–silane cluster ions appear in the mass spectrum. These are

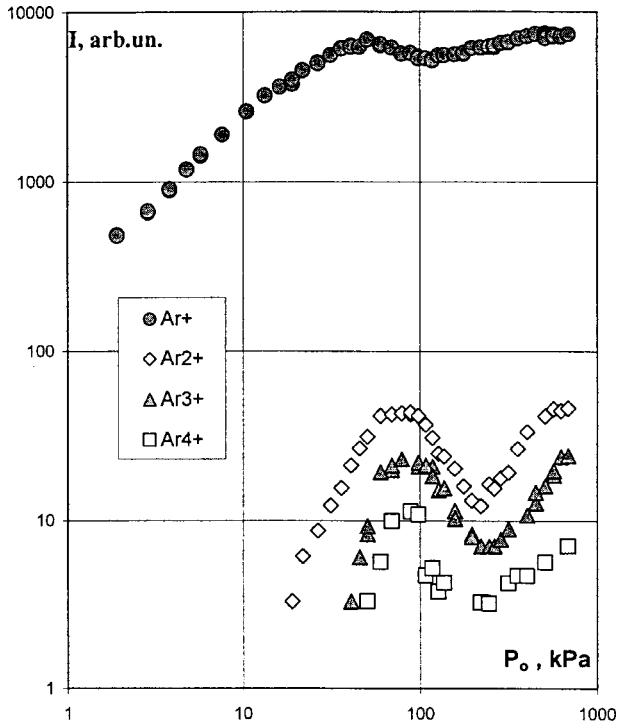

FIG. 1.

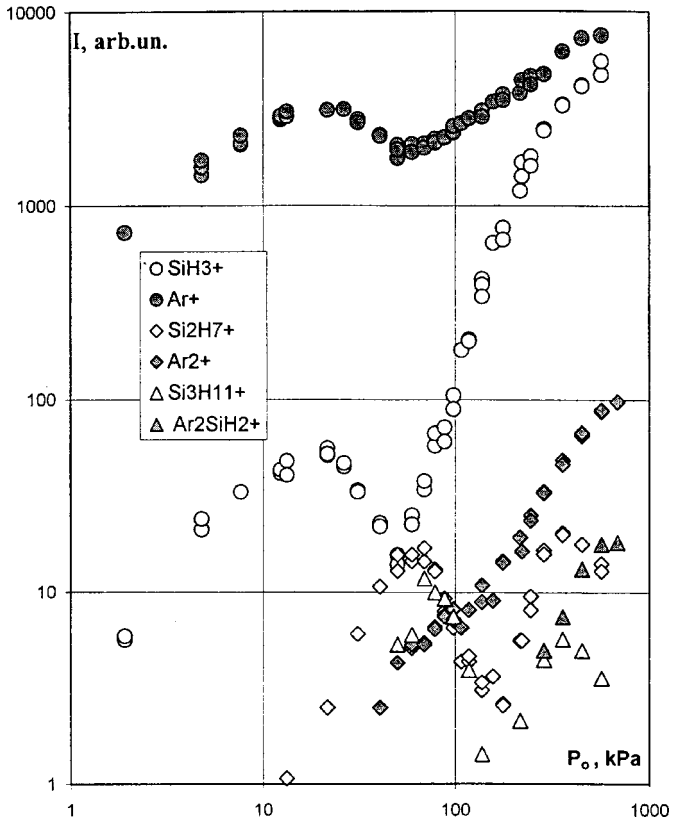

FIG. 2.

evidently formed as a result of the breakup of large mixed argon–monosilane clusters caused by electron impact. At high pressures P_0 the readily condensing impurity can be almost completely transferred to the condensed state in the mixture jet. Thus as the pressure increases, the cluster nucleus consisting mainly of monosilane molecules becomes overgrown with a ''coat'' of argon atoms. This leads to an increase in the argon cluster signals and mixed clusters and reduces the signals from hydrogenated silicon clusters.

To sum up, in a jet of $5\%SiH_4+Ar$ mixture at low pressures P_0 monosilane clusters formed whereas at high pressures mixed monosilane–argon clusters appear.

This work was supported by the Russian Fund for Fundamental Research (Project No. 96-03-33924), by the Ministry of Science and Technical Policies of the Russian Federation (''List of Unique Scientific Research and Experimental Facilities of National Importance'' Registration No. 06-06), and by a Fundamental Natural Science Grant from the Ministry of Education of the Russian Federation.

[1] R. G. Sharafutdinov, A. V. Skrynnikov, A. V. Parakhnevich *et al.*, J. Appl. Phys. **79**, 7274 (1996).
[2] D. Golomb, R. E. Good, A. E. Bailey *et al.*, J. Chem. Phys. **57**, 3844 (1972).
[3] A. Ding, R. A. Cassidy, L. S. Cordis *et al.*, J. Chem. Phys. **100**, 7051 (1994).
[4] G. G. Gartvich, V. G. Dudnikov, A. E. Zarvin *et al.*, Prib. Tekh. Éksp. No. 2, 134 (1997).

Translated by R. M. Durham

Change in the acoustic emission spectrum of dislocation-containing silicon under current and thermal influences

A. M. Orlov, A. A. Skvortsov, and V. A. Frolov

Ulyanovsk State University
(Submitted July 12, 1999)
Pis'ma Zh. Tekh. Fiz. **25**, 52–58 (November 12, 1999)

Changes in the acoustic emission spectra of dislocation-containing silicon under current and thermal influences are investigated. The shift of the maximum frequency of the acoustic emission spectrum is explained and described using the sharp kink model, The stopping constant, velocity, and mobility of the dislocations are estimated. © *1999 American Institute of Physics.* [S1063-7850(99)01011-3]

The influence of dislocations on the mechanical and electrical properties of semiconductors and devices fabricated from them is well known. Linear defects promote the formation of traps and carrier scattering centers when an electric current flows. Moreover, the presence of electric fields may lead to the migration of dislocations at fairly low temperatures. A drifting dislocation crossing the active region of a device may cause it to malfunction. Devices with a high degree of integration are particularly sensitive to this.

The migration of dislocations can be assessed by direct (electron microscopy) and indirect (selective etching) methods of examination. A highly promising method involves analyzing the acoustic noise which always accompanies a moving dislocation.[1] However, the acoustic emission of semiconductors in external electric and thermal fields has clearly not been sufficiently well studied. In particular, no information is available on the acoustic emission of dislocation-containing semiconductors, its temperature dependence, and the influence of elastic stresses.

Thus, the present paper is devoted to a study of the acoustic emission spectra of dislocation-containing silicon under current and thermal influences.

The initial samples were [111]-oriented, phosphorus-doped, dislocation-free silicon wafers ($40\times10\times0.35$ mm) having resistivity $\rho=0.01\,\Omega\cdot$cm. Subsequent annealing for 25 min at 1273 K under conditions of a three-point loading system promoted the appearance of edge dislocations.[2] The dislocation density was estimated by calculating the etch pits revealed after immersing in *CP* etchant at room temperature for 35 sec and was $(2–5)\times10^5$ cm^{-2}.

The experiment was carried out using a technique described in detail in Ref. 3. Acoustic emission was excited by external thermal heating (T = 330–380 K) and by passing a current of density j = $(0.57–4.3)\times10^5$ A/cm^2. A liquid In–Ga eutectic was used for the current-supply contacts. The acoustic emission signals were recorded by a piezocrystal detector positioned on the surface of the wafer. The electrical response from the detector $U(t)$ was recorded by an S9-8 storage oscilloscope and was fed to a computer where a fast Fourier transform algorithm was applied to reconstruct the spectral composition of the acoustic signals $U(\omega)$.

The main cycle of investigations was carried out after the system had reached equilibrium which was determined from the saturation of the acoustic energy

$$W\sim\sum_n U_n^2(\omega_n),$$

where U_n are the amplitudes of harmonics of the experimental spectrum.[3]

The results revealed a surprising difference in the behavior of structures with and without defects under current and thermal influences. Since they possess effective charge and mass, dislocations may migrate under the action of electron wind and electrostatic action, increasing the acoustic noise. A comparative analysis of the spectra of the samples under identical influences indicates an appreciable increase in the amplitude of the signal spectrum $U(f)$ for dislocation-containing silicon with a clearly defined maximum at $f=0.25$ Hz (curves *1* and *2*, Fig. 1).

The migration of dislocations in semiconductors is described by the model of sharp kinks[4] formed when the shoulder of a dislocation attaches to a new defect center. These kinks overcome the second-order Peierls potentials, propagating perpendicular to the dislocation line. The velocity of this displacement is described by:[4]

$$v=d'f_0\left[\exp\left\{-\frac{E_{p2}-\tau bdd'/2}{kT}\right\}-\exp\left\{-\frac{E_{p2}+\tau bdd'/2}{kT}\right\}\right], \quad (1)$$

where E_{p2} is the second-order Peierls potential, d' is its period, τ is the mechanical stress, b is the length of the Burgers vector, d is the dislocation length, and f_0 is the frequency of the kink vibrations.

In thermal equilibrium the kink pairs formed as a result of the thermal activation mechanism decay to form unlike ones, diffuse along the dislocation line, and annihilate on impact. This is why, in thermodynamic equilibrium in the absence of current, the acoustic emission signal from dislocation-containing samples is very small (curve *3*, Fig. 1).

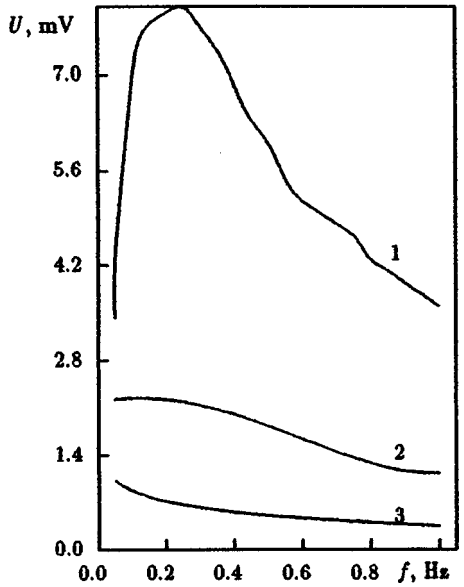

FIG. 1. Acoustic emission spectra: *1* and *2*—silicon with and without dislocations exposed to a current $j=2.9\times10^5$ A/m^2 at $T=360$ K, *3*— dislocation-containing silicon at $T=360$ K ($j=0$).

When an electric field is applied, the stresses created as a result of interaction between carriers and a dislocation[5]

$$\tau=\frac{Bj}{enb} \tag{2}$$

impair the established equilibrium and the kinks begin to migrate in specific directions (here B is the stopping constant, e is the electron charge, and n is the free carrier concentration). In this case, the rate of displacement of the dislocations is determined by the difference between the transition frequencies as the kinks migrate in opposite directions. Their characteristic hopping frequency in the steady-state regime characterizes the transition of dislocations from one metastable state to another. This clearly explains the well-defined maximum in the acoustic emission spectrum of dislocation-containing silicon perturbed by a dc field (curve *1*, Fig. 1).

Taking into account Eqs. (1) and (2) and also the fact that the rate of displacement v of the dislocations may be determined by the product of the dislocation hopping frequency f and the length of a single hop l, we obtain

$$f=\frac{v}{l}=f_0\frac{d'}{l}\left[\exp\left\{-\frac{E_{p2}-Bjdd'/2en}{kT}\right\}-\exp\left\{-\frac{E_{p2}+Bjdd'/2ne}{kT}\right\}\right]. \tag{3}$$

For the following simplification we give expression (3) in the form:

$$f=f_0\frac{d'}{l}\exp\left(\frac{E_{p2}}{kT}\right)\exp\left(\frac{Bjdd'}{2nekT}\right)\left[1-\exp\left(-\frac{Bjdd'}{nekT}\right)\right]. \tag{4}$$

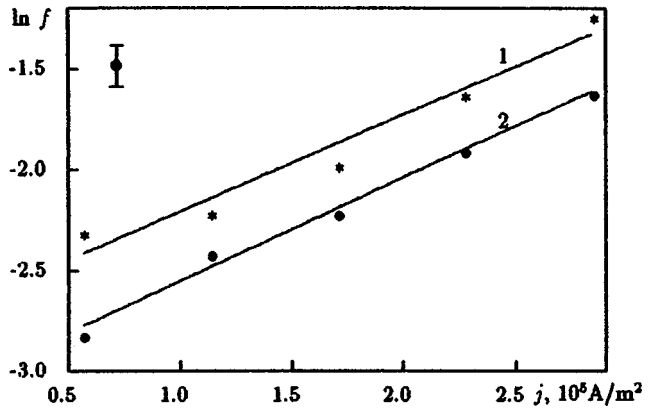

FIG. 2. Logarithm of the maximum frequency of the acoustic emission spectrum as a function of the current density through the sample: *1*—before and *2*—after annealing at $T=1273$ K for 1 h.

Taking the numerical values $B=10^{-6}$ Pa·s], $d=10^{-4}$ [m], $d'=5\times10^{-10}$ [m] (Refs. 4 and 6), $j=(0.57\text{-}4.3)$ A/m^2, and $n=5\times10^{24}$ m^{-3}, the last term in brackets

$$\exp\left(-\frac{Bjdd'}{nekT}\right)\approx(3-10)\times10^{-3}$$

is substantially smaller than unity and can be neglected. This means that the maxima of the experimental spectra (Fig. 2) and the simplified expression (4) rewritten in the form

$$\ln f=\left[\ln\left(f_0\frac{d'}{l}\right)-\frac{E_{p2}}{kT}\right]+\frac{Bdd'}{2nekT}\cdot j, \tag{5}$$

can be used to estimate the stopping constant B and the kink oscillation frequency f_0. It was found that isothermal annealing for 60 min at $T=1273$ K increases the stopping constant B from 10^{-7} to 8×10^{-7} Pa·s and reduces the kink oscillation frequency f_0 from 6×10^6 to 4×10^6 Hz. These changes are caused by the removal of elastic stresses in the heat treatment process and also by the redistribution of impurities near the dislocation line and therefore an increase in the dislocation mass.

These data can be used to determine the dislocation stopping mechanism in silicon in a particular range of temperatures and stresses. We know[7] that the stopping of dislocations in crystals is described by two different mechanisms. This first attributes the stopping to thermoelastic damping caused by a heat flux from the front to the back of the dislocation as is migrates through the crystal. For edge dislocations the stopping constant in this case is:

$$B=\frac{\mu b^2}{2\pi}\frac{9\alpha^2T\chi}{10K}\ln\frac{K}{\rho c_p\omega l'^2}\approx6\times10^{-5}\,[\text{Pa}\cdot\text{s}], \tag{6}$$

where μ is the shear modulus, α is the coefficient of thermal expansion, K is the thermal conductivity, χ is the bulk modulus of elasticity, ω is the relaxation frequency, for nonmetallic crystals $\omega=2\pi\times12\times10^6$ Hz, and $l'\approx10^{-9}$ m is the separation length.

The other mechanism takes into account the scattering of phonons as a dislocation moves through the crystal. For this mechanism we have

$$B=\frac{a}{10v_s}\left(\frac{3ZkT}{a^3}\right)\approx 10^{-6}\,[\mathrm{Pa\cdot s}], \tag{7}$$

where Z is the number of atoms per unit cell, $3kT$ is their thermal energy, v_s is the shear wave velocity, and a is the lattice parameter.

A comparison between the experimental and calculated [Eqs. (6) and (7)] values of the stopping constants suggests that the most probable dislocation stopping mechanism in silicon is the phonon scattering mechanism. For thermoelastic damping the value of B was almost two orders of magnitude higher than the experimentally determined values.

The experimental acoustic emission data and the conclusions reached were further confirmed by the results of direct observations (using etch pits) of the displacement of dislocations. For this we used a method of repeated selective etching. Samples of dislocation-containing silicon with preetched dislocations were exposed to a current density $j=2.9\times 10^5\ \mathrm{A/m^2}$ and temperature $T=350\ \mathrm{K}$ for 72 h. The dislocations were then repeatedly exposed. A metallographic examination of various sections of the samples before and after current treatment revealed the presence of new etch pits, which provide direct confirmation that the dislocations are displaced under the action of a direct electric current. Their displacement toward the positive electrode at the velocity $v_d=5\times 10^{-8}$ cm/s indicates that the dislocations have a negative effective charge and can be used to determine the mobility $\mu_d=v/E=4\times 10^{-8}\ \mathrm{cm^2/(V\cdot s)}$. This supports the assumption made above that the dislocations are increased by electron wind.

Thus, the observed acoustic emission of semiconductors under current and thermal influences is determined by the migration of dislocations. A sharp kink model is used to explain the change in the acoustic emission spectrum with increasing current density caused by redistribution of fluxes of positive and negative kinks. It is observed that isothermal annealing leads to an increase in the stopping constant B and thus reduces the mobility of the dislocation. The dislocation stopping mechanism is inferred and the velocity and mobility of the dislocations is calculated.

[1] V. A. Greshnikov and Yu. E. Drobot, *Acoustic Emission* (Standartov, Moscow, 1976), 272 pp.
[2] V. L. Bonch-Bruevich and S. G. Kalashnikov, *Physics of Semiconductors* (Nauka, Moscow, 1990), 688 pp.
[3] A. M. Orlov, A. A. Skvortsov, and V. A. Frolov, Pis'ma Zh. Tekh. Fiz. **25**(3), 28 (1999) [Tech. Phys. Lett. **25**, 95 (1999)].
[4] T. Suzuki, S. Takeuchi, and H. Yoshinaga, *Dislocation Dynamics and Plasticity* (Springer-Verlag, New York, 1991; Mir, Moscow 1989, 296 pp.).
[5] V. I. Spitsyn and O. A. Troitskiĭ, *Electroplastic Deformation of Metals* (Nauka, Moscow, 1985), 160 pp.
[6] J. Friedel, *Dislocations* (Pergamon Press, Oxford, 1964; Mir, Moscow, 1967, 644 pp.).
[7] W. P. Mason, *Phonon Viscosity and Its Influence on the Absorption of Acoustic Waves and Migration of Dislocations*, in *Ultrasonic Methods of Studying Dislocations* (IIL, Moscow, 1963, pp. 327–371).

Translated by R. M. Durham

Delay of reversible deformation in titanium nickelide after an incomplete transformation cycle

S. P. Belyaev, A. E. Volkov, and A. I. Razov

V. I. Smirnov Research Institute of Mathematics and Mechanics, St. Petersburg State University
(Submitted July 5, 1999)
Pis'ma Zh. Tekh. Fiz. **25**, 59–64 (November 12, 1999)

Characteristic features of the appearance of reversible shape memory in an equiatomic TiNi alloy were studied after a cycle in an incomplete range of martensitic transformation temperatures. It was observed that the establishment of reversible shape memory is accompanied by the SMART effect (Stepwise Martensite to Austenite Reversible Transformation) which is manifest as a temperature delay of the deformation under heating. The delay occurs at that temperature at which the transformation terminated in the preliminary thermal cycle and is 3 °C. © *1999 American Institute of Physics.* [S1063-7850(99)01111-8]

Alloys undergoing thermoelastic martensitic transformations demonstrate various ''memory'' effects for their mechanical and thermal prehistory. These particularly include the shape memory effect which is manifest as the return to a predefined deformation during heating through a range of transformation temperatures.[1,2] A more complex phenomenon known as reversible shape memory essentially involves remembering the path along which the material was loaded. Information on this path is stored in the domain structure of the martensite and when various conditions are satisfied, it is reconstructed as a result of a martensite → austenite transformation.[3] In addition to these well-studied phenomena, the so-called SMART effect (Stepwise Martensite to Austenite Reversible Transformation) has recently come under discussion.[4–8] This is a specific type of memory which is initiated by a preliminary incomplete transformation cycle under heating (ITCH), i.e., a procedure in which the martensite → austenite transformation terminates in the temperature range $A_s - A_f$ and cooling takes place, transferring the material to the martensitic state. If the material is now heated through the complete range of reversible transformation, monotonically increasing the temperature, it is possible to observe a characteristic feature in the temperature kinetics of the transformation. Specifically, a delay in the transformation will occur during heating, which is manifest as the appearance of a ''step'' on the temperature dependence of any physical quantity sensitive to changes in the phase state. This transformation delay occurs at that temperature at which the phase transition terminated during the preliminary ITCH or at a slightly higher temperature. When the ITCH takes place several times with the temperature at which the reverse transition terminates decreasing from one cycle to another, the number of delays in the next complete transformation is the same as the number of ITCHs preceding it. This behavior is classified as the SMART effect, which has been observed for TiNi, TiNiFe, TiNiCu, AgCd, and CuAlZn alloys. This in fact means that different alloys with thermoelastic martensite transformations can ''remember'' a series of incomplete martensite→ austenite transformations.

Two working hypotheses are attractive to explain the physical reasons for the SMART effect. The first is based on the role of lattice defects localized near interphase boundaries, which are inherited by the martensite phase and remain in the material after an ITCH. It is postulated that these defect pileups act as pinning (attachment) centers for the moving interphase boundary during the SMART effect. The other hypothesis is concerned with local elastic-energy relaxation processes at the interphase boundary as a result of which the driving force of the transformation decreases and an additional supply of heat is required for it to continue.

The SMART effect has mainly been observed when the temperature dependences of the electrical resistance vary, and also in calorimetric experiments. However, quite clearly a change in the temperature kinetics of a martensitic transformation should also influence the behavior of the deformation processes associated with this transformation. In fact, it has recently been reported that the SMART effect is observed on mechanical hysteresis loops in the superelastic TiNi alloy.[8]

In the present paper we report the first experimental data obtained from a study of the SMART effect during the establishment of reversible shape memory in TiNi.

The experiments were carried out using wire samples of approximately equiatomic TiNi alloy. The diameter of the samples was 3 mm and their length 550 mm. At room temperature the alloy is in the martensitic state. The samples were isothermally deformed by stretching by 12% and then after the load had been removed, they underwent spontaneous reversible deformation under thermal cycling through the temperature range of martensitic transformations. The samples were heated by an electric current and cooled naturally by leaving in air. The thermal cycling was repeated many times in order to stabilize the deformation in the cycle. As a result, after twenty cycles the reversible change in the deformation was 0.8% in the range 20–130 °C (including thermal elongation of the sample) and remained almost unchanged from one cycle to another.

The reversible shape memory effect is attributed to the

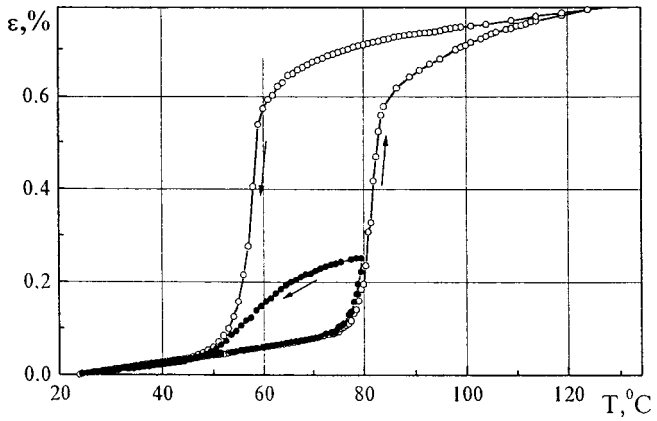

FIG. 1. Strain versus temperature illustrating the spontaneous deformation of a TiNi alloy sample in a thermal cycle through the transformation range (open circles) and in an incomplete cycle during heating (filled circles).

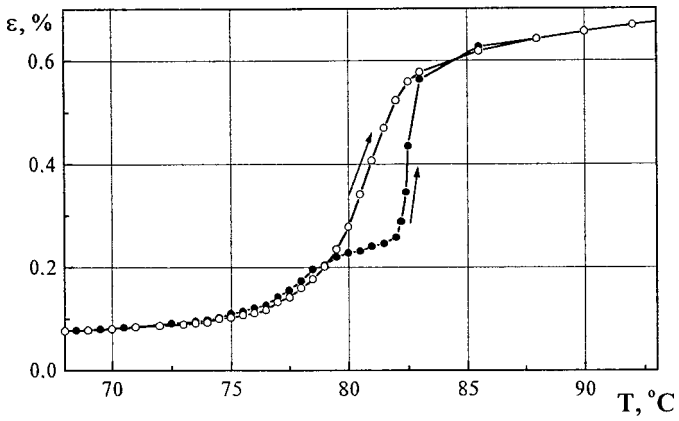

FIG. 2. Strain versus temperature for heating of a TiNi alloy sample during the establishment of the SMART effect (filled circles) and in a the next thermal cycle (open circles).

existence of oriented internal stresses in the predeformed material. These stresses orient elementary microshears during martensitic transformations, thereby promoting spontaneous reversible deformation at the macrolevel. It thus becomes clear that regardless of the nature of the SMART effect, it will be observed during the establishment of reversible shape memory because the relaxation of internal stresses and the formation of a particular defect structure, and together with any change in the kinetics of the phase transition in general, should influence the temperature kinetics of the deformation.

We shall now examine the experimental data. For comparison Fig. 1 gives thermal-deformation dependences obtained in a thermal cycle through a complete range of martensitic transformations and in an incomplete cycle immediately following the first. It can be seen that during heating in the incomplete cycle the transformation was terminated at 79 °C and 0.25% strain after which the material was transferred to the martensitic state by cooling to room temperature. The filled circles in Fig. 1 essentially show the ITCH required to initiate the SMART effect. This effect was observed during subsequent heating through the complete range of transformation temperatures (Fig. 2, filled circles). The fragment of the ''strain–temperature'' dependence clearly reveals a characteristic feature in the form of a step. From 79 °C the strain stops changing (the slight slope of the line is merely caused by the thermal elongation of the sample) and this change only reappears after the temperature has increased by 3 °C. It can be seen from Fig. 2 that the beginning of the deformation delay coincides with the temperature at which heating stops in the ITCH (79 °C). However, this agreement is not observed for the strain, and the value $\varepsilon = 0.25\%$ is only achieved at the end of the delay step.

After heating had ended, the sample was cooled to room temperature and then reheated. The curve corresponding to the repeated heating is shown by the open circles in Fig. 2 and has no such features. In other words, the SMART effect was only observed once in the cycle directly following the ITCH, which is consistent with the known data.

To sum up, it can be seen from these results that the SMART effect is manifest during the establishment of reversible shape memory in the form of a deformation delay in the range of martensite→austenite transformation temperatures. From the point of view of using shape-memory alloys, the fact that the deformation exhibits complex kinetics after partial temperature cycles must be borne in mind, particularly in the design of devices requiring accurate positioning of moving parts.

This work was supported by RFBR Grant No. 99-01-00987 and by the State Program for Support of Leading Scientific Schools, Grants Nos. 90-15-96077 and 96-15-96066.

[1] V. A. Likhachev, S. L. Kuz'min, and Z. P. Kamentseva, *Shape Memory Effect* (Leningrad Technical University Press, Leningrad, 1987), 216 pp.
[2] *Handbook of Materials with Shape Memory*, Vol. 2, edited by V. A. Likhachev (NIIKh St. Petersburg State University Press, St. Petersburg, 1998), 374 pp.
[3] S. P. Belyaev, S. L. Kuz'min, and M. Yu. Rogachevskaya, *Structure and Properties of Metallic Materials and Compositions* (NPI, Novgorod, 1989), pp. 44–51.
[4] G. Airoldi, G. Carcano, and G. Riva, in *Proceedings of the European Symposium on Martensitic Transformation and Shape Memory Properties, Aussois, France, 1991*, published in J. Phys. IV **1**, Colloq. 4, 277 (1991).
[5] G. Airoldi, S. Besseghini, and G. Riva, in *Proceedings of the International Conference on Martensitic Transformations (ICOMAT-92), 1992, Monterey, CA*, edited by C. M. Wayman and J. Perkins (Monterey Institute of Advanced Studies, Carmel, 1993), pp. 959–964.
[6] G. Airoldi, S. Besseghini, and G. Riva, in *Proceedings of the Third European Symposium on Martensitic Transformations, Barcelona, Spain, 1994*, published in J. Phys. IV **5**, Colloq. 2, 483 (1995).
[7] G. Riva, S. Besseghini, and G. Airoldi, J. Phys. IV **5**, Colloq. 8, 877 (1995).
[8] G. Airoldi, A. Corsi, and G. Riva, J. Phys. IV **7**, Colloq. 5, 513 (1997).

Translated by R. M. Durham

Explosive growth of perturbations of the surface of a conducting liquid in an electric field

N. M. Zubarev

Institute of Electrophysics, Urals Branch of the Russian Academy of Sciences, Ekaterinburg
(Submitted July 12, 1999)
Pis'ma Zh. Tekh. Fiz. **25**, 65–69 (November 12, 1999)

An analysis is made of the behavior of the free surface of a conducting liquid in an external electric field near the Tonks–Frenkel instability threshold assuming that the incipient wave is one-dimensional. It is shown that the surface dynamics is described by the nonlinear Klein–Gordon equation. This equation is used to formulate criteria for the explosive growth of perturbation amplitudes. © *1999 American Institute of Physics.* [S1063-7850(99)01211-2]

The Tonks–Frenkel instability[1,2] of the boundary of a conducting liquid in a strong electric field plays an important role in the general problem of dielectric strength. This instability leads to the avalanche-like growth of surface perturbations[3] and the appearance of regions of high energy concentration whose breakup is accompanied by intense emission processes.[4,5] The significant nonlinearity of these phenomena necessitates the construction of a theoretical model of the advanced stages of Tonks–Frenkel instability, in particular identifying the conditions for the explosive growth of perturbations.

The dispersion law for waves at the plane surface of an ideally conducting liquid in an external electric field E has the form:[6]

$$\omega^2 = gk + \frac{\alpha}{\rho}k^3 - \frac{E^2}{4\pi\rho}k^2,$$

where g is the acceleration due to gravity, α is the coefficient of surface tension, and ρ is the density of the medium. It can be seen that when the energy density of the field $W = E^2/(8\pi)$ exceeds the critical value $W_c = \sqrt{g\alpha\rho}$ the surface is unstable, and for low supercriticalities $\varepsilon = (W - W_c)/W_c$ perturbations grow with wave numbers close to $k = k_0 = \sqrt{g\rho/\alpha}$. In this situation it is possible to study the nonlinear dynamics of the surface perturbations using equations for the envelopes.

We shall consider the potential motion of an ideal incompressible conducting liquid occupying the region $z \leqslant \eta(x,t)$ [the free surface of the liquid is given by the function $z = \eta(x,t)$], in an external electric field directed along the x axis. The velocity potential of the liquid Φ and the electric field potential φ satisfy the Laplace equations

$$\Delta\Phi = 0, \quad \Delta\varphi = 0$$

with the conditions at infinity:

$$\Phi \to 0 \quad z \to -\infty,$$

$$\varphi \to -Ez, \quad z \to \infty,$$

and also as a result of the equipotential surface of the conducting liquid, these potentials satisfy the condition

$$\varphi = 0, \quad z = \eta.$$

The functions $\eta(x,t)$ and $\psi(x,t) = \Phi|_{z=\eta}$ are canonically conjugate quantities[7] so that the dynamic and kinematic conditions at the surface have the form:

$$\psi_t = -\frac{\delta H}{\delta \eta}, \quad \eta_t = \frac{\delta H}{\delta \psi},$$

where the Hamiltonian

$$H = \int_{z\leqslant\eta} \frac{(\nabla\Phi)^2}{2} d^2r - \int_{z\geqslant\eta} \frac{(\nabla\varphi)^2}{8\pi\rho} d^2r + \int \left(\frac{g\eta^2}{2} + \frac{\alpha}{\rho}\left(\sqrt{1+\eta_x^2} - 1\right)\right) dx$$

describes the total energy of the system apart from the constant. This Hamiltonian may be represented as the surface integral:

$$H = \int \frac{\psi}{2}(\hat{T}_+ \hat{k} \hat{T}_+^{-1}\psi - \eta_x \hat{T}_+ \partial_x \hat{T}_+^{-1}\psi)dx - \int \frac{W\eta}{\rho}(\hat{T}_- \hat{k} \hat{T}_-^{-1}\eta + \eta_x \hat{T}_- \partial_x \hat{T}_-^{-1}\eta)dx + \int \left(\frac{g\eta^2}{2} + \frac{\alpha}{\rho}\left(\sqrt{1+\eta_x^2} - 1\right)\right) dx, \tag{1}$$

where the integral operator $\hat{k}$ is expressed in terms of the Hilbert transform $\hat{H}$:

$$\hat{k} = -\frac{\partial}{\partial x}\hat{H}, \quad \hat{H}f = \frac{1}{\pi}\text{P.V.}\int_{-\infty}^{\infty} \frac{f(x')}{x'-x}dx',$$

and the nonlinear operators $\hat{T}_\pm$ are given by

$$\hat{T}_\pm = \sum_{n=0}^{\infty} \frac{(\pm\eta)^n \hat{k}^n}{n!}.$$

Assuming that the supercriticality $|\varepsilon|$ and the characteristic angles of inclination of the surface $|\nabla\eta|$ are small, we convert to the envelopes by using the substitutions

$$\eta = A(x,t)e^{ik_0x} + A^*(x,t)e^{-ik_0x} + 2k_0A^2e^{2ik_0x} + 2k_0A^{*2}e^{-2ik_0x},$$

$$\psi = B(x,t)e^{ik_0x} + B^*(x,t)e^{-ik_0x},$$

in which $k_0 \to 2k_0$ interaction is taken into account. Substituting these expressions into the Hamiltonian (1) and performing the necessary averaging, we obtain to within the fourth order in terms of amplitude:

$$H = \int \left(k_0|B|^2 - \frac{\varepsilon\omega_0^2}{k_0}|A|^2 + \frac{\omega_0^2}{2k_0^2}|A_x|^2 - \frac{11\omega_0^2k_0}{8}|A|^4 \right) dx,$$

where $\omega_0^2 = 2gk_0$. After scaling

$$\omega_0 t \to t, \quad \sqrt{2}k_0x \to x, \quad \sqrt{11/4}k_0A \to A$$

the equation for the complex amplitude A corresponding to this Hamiltonian has the form

$$A_{tt} = \varepsilon A + A_{xx} + |A|^2A. \tag{2}$$

That is to say, the envelope of packet A obeys the nonlinear Klein–Gordon equation ($|\phi|^4$) model).

A characteristic feature of Eq. (2) is that the nonlinearity does not stabilize the linear instability but conversely intensifies it, leading to explosive amplitude growth under certain conditions. By analogy with Refs. 8 and 9 where the dynamics of collapse was investigated for the Klein–Gordon equation with various types of nonlinearity, we analyze the time evolution of the norm

$$X = \int |A|^2 dx.$$

We write the Hamiltonian corresponding to Eq. (2) in the form:

$$H = \int \left(\frac{3}{2}|A_t|^2 - \frac{1}{4}(|A|^2)_{tt} - \frac{\varepsilon}{2}|A|^2 + \frac{1}{2}|A_x|^2 \right) dx.$$

Omitting the term with spatial derivatives and using the Cauchy–Buniakowski inequality $X_t^2 \leqslant 4X\int|A_t|^2dx$, we find:

$$H \geqslant \frac{3X_t^2}{8X} - \frac{X_{tt}}{4} - \frac{\varepsilon X}{2}. \tag{3}$$

This majorizing inequality agrees with those obtained in Refs. 8 and 9 apart from the coefficients. Converting to the new variable $Y = X^{-1/2}$ allows us to rewrite inequality (2) in the form of Newton's second law:

$$Y_{tt} \leqslant -\frac{\partial P(Y)}{\partial Y}, \quad P(Y) = -\frac{\varepsilon}{2}Y^2 - \frac{H}{2}Y^4,$$

where Y plays the role of the ''particle'' coordinate and P is its potential energy. Analyzing this inequality for the case when the particle velocity is initially directed toward the origin at time $t=0$: $Y_t(0)<0$, it is easy to observed that Y first vanishes for $\varepsilon>0$ if $U(0)>0$, second for $\varepsilon<0$ and $H<0$, and third for $\varepsilon<0$ and $H>0$ if $U(0)>\varepsilon^2/(8H)$, or $Y^2<|\varepsilon|/(2H)$, where $U = Y_t^2/2 + P(Y)$ is the total particle energy. Quite clearly, if these conditions are satisfied, the norm X goes to infinity within a finite time, which corresponds to explosive amplitude growth. The following estimate holds for the time T of occurrence of singularity:[8,9]

$$T \leqslant \int_0^{Y(0)} \frac{dY}{\sqrt{2U(0) - 2P(Y)}}.$$

Note that part of the criteria for explosive amplitude growth refers to the case when the plane surface is stable with respect to small perturbations ($\varepsilon<0$). This implies that the excitation of instability will have a rigid character.

To sum up, this analysis of the surface behavior of a conducting liquid in an electric field near the instability threshold has shown that in the first nonvanishing order the nonlinearity defines the tendency to explosive perturbation growth.

The author is grateful to E. A. Kuznetsov, A. M. Iskol'dskiĭ, and N. B. Volkov for fruitful discussions.

This work was carried as part of an RFBR project, Grant No. 97-02-16177.

[1] L. Tonks, Phys. Rev. **48**, 562 (1935).
[2] Ya. I. Frenkel', Zh. Tekh. Fiz. **6**, 347 (1936).
[3] M. D. Gabovich and V. Ya. Poritskiĭ, JETP Lett. **33**, 304 (1981).
[4] L. I. Pranevichyus, I. Yu. Bartashyus, and V. I. Ilgunas, Izv. Vyssh. Uchebn. Zaved. Fiz. **4**, 44 (1969).
[5] I. Yu. Bartashyus, L. I. Pranevichyus, and G. N. Furseĭ, Zh. Tekh. Fiz. **41**, 1943 (1971) [Sov. Phys. Tech. Phys. **16**, 1535 (1971)].
[6] L. D. Landau and E. M. Lifshitz, *Electrodynamics of Continuous Media*, 2nd ed. (Pergamon Press, Oxford, 1984; Nauka, Moscow, 1982).
[7] V. E. Zakharov, Prikl. Mekh. Tekh. Fiz. **2**, 86 (1968).
[8] E. A. Kuznetsov and P. M. Lushnikov, Zh. Éksp. Teor. Fiz. **108**, 614 (1995) [JETP **81**, 332 (1995)].
[9] E. M. Maslov and A. G. Shagalov, Phys. Lett. A **239**, 46 (1998).

Translated by R. M. Durham

Abbreviation of description and effective characteristics

G. E. Skvortsov

St. Petersburg State University
(Submitted July 9, 1999)
Pis'ma Zh. Tekh. Fiz. **25**, 70–77 (November 12, 1999)

A universal projectional method of abbreviating description is given and its application is demonstrated for all levels. Effective characteristics obtained as a result of this abbreviation are considered. Their properties and behavior are discussed for a wide range of measures of action together with the effects induced by them. © *1999 American Institute of Physics.* [S1063-7850(99)01311-7]

1. A study of processes of increasing intensity inevitably involves taking into account increasingly deeper structural levels of systems and an increasing number of quantities involved in the process. A similar situation arises for regimes of structural transitions when a system ''opens'' and reacts to a multiplicity of external factors. In both cases the dimensions of the ''action space'' increase substantially.

At the same time, any observation is limited to a finite number of quantities. Consequently, a disparity ensues between the increase in the dimensions of the process and the limited possibilities of observing and describing it.

A natural, and essentially the only way, of solving this problem is to use a systematic abbreviation of description. In this case, the number of determining quantities only increases slightly with an overall reduction in the dimensions of the description and this is accompanied by a transition to effective characteristics.

The fundamental indicator of the latter is a dependence on the measure of action, i.e., these are essentially nonequilibrium characteristics. Such characteristics include the effective mass, quasi-energy, and nonequilibrium susceptibilities. In general, as we know, effective characteristics have an operator dependence on the measure of action.[1,2]

In specific problems from various fields (nuclear theory, molecular dynamics, kinetics, hydrodynamics) the transition to effective characteristics is usually made by using phenomenological models. Such models cannot generally be used to interpolate for essentially nonequilibrium regimes, i.e., they cannot solve the fundamental problem.

It should be noted that in many cases, nonequilibrium characteristics must be dealt with initially, since they have no limits as the measure of action tends to zero. Examples of this type are cited in Refs. 3 and 4.

Note that in the general context, according to the postulate of universal coupling, all the characteristics of nonequilibrium systems are effective.

2. Here we describe a universal method of abbreviating description and going over to effective characteristics.

The method of projecting the initial values and equations onto suitable half-spaces and obtaining closed equations for the components of interest is universal and extremely convenient. This method can be successfully used for abbreviating descriptions of various types and on various levels.[5–7]

We present the general scheme of the projectional method and isolate the effective characteristics thus obtained.

The initial description of the dynamics of a system is given by the evolution equation for the set of the quantity $F=\{f_x(X_x t)\}$

$$\partial_t F=\mathcal{E}[F]+Q, \tag{1}$$

where X_s is the set of general coordinates, and $Q=\{q_s\}$ is the source term. This equation describes the system at a more detailed level than that in which we are ultimately interested. It may be nonconstructive, such as the Liouville equation for 10^{20} particles. What is important is that by abbreviating the description, this equation may be used as the basis to go over to the next, less detailed but more constructive, level of description.

The description of any level is abbreviated by projecting it onto a subspace PF of smaller dimensions

$$F=PF+P_\perp F\equiv F_p+F_\perp, \quad P_\perp\equiv(I-P),$$

$$P^+P=I_p, \quad P^+P_\perp=0, \quad P=\sum_m P_m. \tag{2}$$

This representation is similar to an expansion as a Fourier series, F_p is the finite number of first terms, and $F_\perp$ is the residue.

Dividing Eq. (1) as in Eq. (2) and projecting onto the subspaces F_p and $F_\perp$, we obtain the following two equations:

$$\partial_t F_p=\mathcal{E}_p[F_p]+\mathcal{E}_p[F_\perp]+P\Delta\mathcal{E}[F_p+F_\perp]+Q_p, \tag{3}$$

$$\partial_t F_\perp=\mathcal{E}_\perp[F_\perp]+\mathcal{E}_\perp[F_p]+P_\perp\Delta\mathcal{E}[F_p+F_\perp]+Q_\perp, \tag{4}$$

$$\Delta O[f+\varphi]\equiv O[f+\varphi]-O[f]-O[\varphi],$$

where O is an arbitrary operator (taken to abbreviate the expressions for which P and ∂_t commute). The first equation (system) gives the basis of the abbreviated description at the required level, and the second is used for closure.

We substitute the operator solution of Eq. (4)

$$F_\perp=R_\perp[\mathcal{E}_\perp[F_p]+Q_\perp],$$

$$R_\perp[\bullet]=\{\partial_t-\mathcal{E}_\perp[\bullet]-P_\perp\Delta\mathcal{E}[F_p+\bullet]\}^{-1}, \tag{5}$$

into Eq. (3) and obtain a closed system of abbreviated description

$$\partial_t F_p = \mathcal{E}_p[F_p] + \partial_t \hat{F}_p + Q_p, \tag{6}$$

$$\partial_t \hat{F}_p = \mathcal{E}_p\{R_\perp[\mathcal{E}_\perp(F_p)]\} + \mathcal{E}_p[R_\perp(Q_\perp)] + \ldots . \tag{7}$$

The quantity $\partial_t \hat{F}_p$ is usually called the ''product'' and the expressions (7) are closing relations. In hydrodynamics, these determine the general transport laws and transport operators.

The relationships (7) determine effective characteristics of a different type. Taking into account the form of the resolvent (5), these indicate the qualitative dependence of the effective characteristics on the measure of action. In particular, in the lowest order in terms of small measures of action, equilibrium characteristics are obtained (coefficients of proportionality between ''fluxes'' and ''forces''). In the opposite limiting case of very large measures of action, the resolvent defines the effective characteristics in the form of ''decaying operators.'' For example, for a large high-speed measure of the measures of action we have the effective characteristics $\sim R \sim \partial_t^{-1}$.

Realizing the right-hand sides of the equations (6), and principally the relations (7) for various systems and levels of description is a key problem in dynamic theory.

A very simple example of a general scheme of abbreviated description involves reducing the two linear equations

$$d_t x_i = \nu_{ij} x_j + q_i \quad (i = 1,2)$$

to a single one (for $x_1 \equiv y$)

$$d_t y = \nu_{11} y_1 + \nu_{12}[d_t - \nu_{22}]^{-1}[\nu_{21} y + q_2] + q_1. \tag{8}$$

In this case, the effective relaxation operator has the form $\tilde{\nu}_{11} = \nu_{11} + \nu_{12}[d_t - \nu_{22}]^{-1}\nu_{21}$. Quite clearly, at low speed $d_t \to 0$ this is given by $\nu_{11} - \nu_{12}\nu_{21}/\nu_{22}$, and at high speed this operator is ν_{11}.

In this way Maxwell and Boltzmann, followed by Leontovich and Mandelstam derived relaxation theory from a moment system.

3. Applying this general scheme to the dynamic description of a system of $N(\sim 10^{20})$ particles with creation and annihilation, we obtain a general kinetic equation.

This equation describes the evolution of a set of distribution functions $F(\Gamma_n, \overline{x}, t) = \{f_x(\Gamma_s, \overline{x}, t)\}$ of interacting complexes of structure-kinetic elements $(s = 1,2, \ldots n)$, $\Gamma_s = (\overline{p^s}, \overline{x^s}, j^s)$, where p^s, x^s, j^s are the momenta, coordinates, and internal characteristics of the s complexes. This has the form

$$\partial_t F = -\mathbf{V} \bullet \nabla F - \mathcal{F}[F] - I[F] + Q, \tag{9}$$

where $\mathbf{V}$ is the velocity of the s-complex, ∇ is the gradient, and $\mathcal{F}[\,]$ is the operator of the forces acting on the complex. The strong interaction operator $I[F]$ takes into account all possible creation and annihilation processes of s-complexes and also delay and nonlocality in the collision region.

The simplest variant of Eq. (9) for a low-density gas consisting of structureless particles is the Boltzmann equation.

Equation (9) is extremely complex and specifying it for specific systems is by no means easy and its solution is an open-ended problem.

In view of this, a suitable objective is to use this equation as the basis of a macroscopic theory describing regimes over a wide range of nonequilibrium.

Such a theory for liquid systems (superhydrodynamics) was presented in Ref. 5, and its linear variant was analyzed fairly comprehensively in Refs. 4, 8, and 9. A fundamental position in this theory is occupied by the effective susceptibilities: the operators for diffusion, thermal diffusion, viscosity, viscothermal conductivity, and so on, which are determined by substituting the operator $\mathcal{E}$ in the form of the right-hand side of Eq. (9) into relation (7).

4. Using the effective characteristics (susceptibilities) in the complete macroscopic theory (superhydrodynamics) reveals a wide range of effects which are not ''seen'' in kinetic theory and are absent in classical theories.

In view of their practical value, we indicate the basic classes of these effects.

The first class are cross effects which are fully represented in superhydrodynamics: these include thermoviscous, hydro-visco-thermoconducting, and so on.[4] These effects are generally small under weak nonequilibrium, but for large gradients they are comparable with diagonal effects (viscosity, thermal conductivity).

Relaxation aftereffects are well known; Boltzmann was one of the first to observe these.

Over the last few decades nonlocal effects indicated by superhydrodynamics have become acknowledged for low-temperature conditions, electromagnetoactive media, and low-density gases.

Effects of ultralarge susceptibilities are ascribed to the form of the resolvent (5) provided that the inverse operator is small (which corresponds to instability of the structure). In particular, an effect of infinite conductivity for the threshold value of the electric field was indicated in Ref. 9.

A whole range of effects related to characteristic features in the dependences of the effective characteristics (susceptibilities) on the measure of action were described in Ref. 10.

Hence, nonequilibrium of the effective characteristics and its adequate reflection are extremely important.

5. In addition to the properties of indicating effects, abbreviation of description plays an important computational role.

Computational advantages are well known when problems involving the dynamics of systems with an infinite number of degrees are reduced to a finite system of ordinary differential equations.

This is generally accomplished by means of general Fourier series and these are usually truncated, i.e., $F_\perp = 0$ is assumed.

This method of closure is generally inadequate, and its use for an approximation even of very large dimensions is ineffective. This is demonstrated by the example of the problem of sound at frequencies higher than the characteristic internal frequency.[11] Using more that five hundred moments[12] did not produce any agreement with the experiment, whereas the choice of the first five moments as F_p (for

the one-dimensional problem) within the limits of the projectional method yielded complete agreement.

Thus, it is recommended that a complete projectional scheme should always be used to reduce to a finite-dimensional problem and then suitable approximations should be used to realize the relations (7).

6. When analyzing the dynamics of finite-dimensional systems, it is useful to abbreviate the description by reducing the number of equations or isolating the regular component of the process in a series of ratios.

We shall demonstrate an abbreviated description for a system of three equations with quadratic nonlinearity

$$d_t x_i = -\nu_i x_i + \sum_{j\neq i}^{3} \nu_{ij} x_j + \sum_{j,e} \nu_{ije} x_j x_e + q_i, \tag{10}$$

where $\nu_i > 0$, ν_{ij}, ν_{ije} are constant velocity coefficients. The system (10) includes most known models (Volterra, Lorentz, Belousov–Zhabotinskiĭ, and so on).

For the abbreviated description, i.e., a reduction in the number of equations, we shall assume, in accordance with the general recommendation, that the value of x_2 has the longest lifetime and the lowest frequency in the linear approximation. In view of this, it is advisable to reduce the values of x_1 and x_3.

As usual, we shall consider a normal reaction, i.e., we shall assume $x_{1,3}(t=0)=0$. In order to make the final expressions less cumbersome, we retain one nonlinear off-diagonal term with ν_{112}, ν_{231}, ν_{323} in each equation and we assume $q_1 \equiv q_3 = 0$.

Taking into account these simplifications, the final expression for $x_2 \equiv y$ has the form

$$d_t y = -\nu_2 y + \sum_{i=1,3} \nu_{2i} \hat{x}_i[y] + \nu_{213} \hat{x}_1[y] \hat{x}_3[y] + q(t), \tag{11}$$

$$\hat{x}_1[y] = \int_0^t d\tau \exp\left\{ -\int_\tau^t [\nu_1 - \nu_{112} y(\tau')] d\tau' [\nu_{12} y(\tau) + \nu_{13} \hat{x}_3(y)] \right\} \equiv \nu_{12} R_{12}[y,y] + \nu_{13} R_{12}[y,\hat{x}_3], \tag{12}$$

$$\hat{x}_3[y] = R_{32}[\nu_{31}\nu_{12} R_{12}[y,y] + \nu_{32} y],$$

$$R_{32} \equiv [d_t + \nu_3 + \nu_{13}\nu_{31} R_{12}[y,\bullet] - \nu_{323} y]^{-1}. \tag{13}$$

This equation (11)–(13) is considerably more complex than its prototype $(10)_2$ although being a single entity it has many advantages over the system (10). This can be used as a convenient example to demonstrate all known characteristics: auto-oscillations, time bifurcations, strange attractor, and transition to dynamic chaos. It is also convenient for using approximate methods, particularly using averaging and isolating vibrational effects.

These topics will be considered in a special study.

7. To conclude our discussion of a series of abbreviations, we isolate the main component of the projectional method and indicate its role in various problems.

The main component involves allowing for the characteristic features of the resolvent of abbreviated description (5) when realizing the closing relations and the effective characteristics.

The characteristic features of the resolvent: asymptotic behavior at high degrees of nonequilibrium, jumps, and going to infinity on the spectrum, play an important role in fundamental and applied problems.

In the problem of a transition from a reversible to an irreversible description (Bogolyubov, Fock and Krylov, Prigogine) a key role is played by the characteristics of the resolvent attributed to the continuous spectrum. Allowance for the continuous spectrum combined with abbreviated description averaging ensures a transition to irreversibility.

In computational problems using the general Fourier series method, it is advisable to use a resolvent form of closure, as shown by the example of the sound problem. This can allow for the spectral characteristics more adequately that the usual procedure of making the residue zero.

The successful application of effective characteristics over a wide range of conditions presupposes a suitable interpolation based on exact operator expressions. Even a very approximate representation of the resolvent can give more successful expressions for the effective characteristics such as the expression for the effective conductivity of a turbulent plasma in a magnetic field.[13]

[1] G. E. Skvortsov, Pis'ma Zh. Tekh. Fiz. **23**(22), 7 (1997) [Tech. Phys. Lett. **23**, 861 (1997)].
[2] G. E. Skvortsov, Pis'ma Zh. Tekh. Fiz. **24**(19), 7 (1998) [Tech. Phys. Lett. **24**, 749 (1998)].
[3] G. E. Skvortsov, Zh. Éksp. Teor. Fiz. **57**, 2054 (1969) [Sov. Phys. JETP **30**, 1114 (1969)].
[4] G. E. Skvortsov, Zh. Éksp. Teor. Fiz. **63**, 502 (1972) [Sov. Phys. JETP **36**, 266 (1972)].
[5] G. E. Skvortsov, Vestn. Leningr. Gos. Univ. **13**, 94 (1979).
[6] I. I. Blekhman, *What Can Vibration Be?*, Moscow (1988), 208 pp.
[7] G. E. Skvortsov, Zh. Tekh. Fiz. **59**(3), 62 (1989) [Sov. Phys. Tech. Phys. **34**, 289 (1989)].
[8] G. E. Skvortsov, Zh. Éksp. Teor. Fiz. **68**, 956 (1975) [Sov. Phys. JETP **41**, 473 (1975)].
[9] E. N. Perevoznikov and G. E. Skvortsov, Zh. Tekh. Fiz. **61**(9), 1 (1991) [Sov. Phys. Tech. Phys. **36**, 967 (1991)].
[10] G. E. Skvortsov, Pis'ma Zh. Tekh. Fiz. **23**(6), 85 (1997); **23**(7), 23 (1997) [Tech. Phys. Lett. **23**, 246 (1997); **23**, 261 (1997)].
[11] G. E. Skvortsov, Zh. Éksp. Teor. Fiz. **49**, 1248 (1965).
[12] C. Pekeris, Z. Alterman, L. Finkelstein, and K. Frankowski, Phys. Fluids **5**, 1608 (1962).
[13] A. S. Dmitriev and O. A. Sinkevich, Teplofiz. Vys. Temp. **15**, 489 (1997).

Translated by R. M. Durham

Percolation shunting of an electrified surface

Yu. I. Kuz'min

A. F. Ioffe Physicotechnical Institute, Russian Academy of Sciences, St. Petersburg
(Submitted July 9, 1999)
Pis'ma Zh. Tekh. Fiz. **25**, 78–85 (November 12, 1999)

Results are presented of investigations of the surface relaxation of electret charge. It is established that when the electret is exposed to increased moisture, the charge transfer is of a percolation nature. Characteristics of the adsorption and growth of electrically conducting phase nuclei during the formation of a percolation cluster at an electrified surface are studied. The critical index of the correlation length of the percolation cluster is determined and shows good agreement with known theoretical estimates. © *1999 American Institute of Physics.* [S1063-7850(99)01411-1]

In the present paper an analysis is made of the surface relaxation of the charge of electrets exposed to moisture from the surrounding atmosphere. Particular attention is paid to adsorption and nucleation of an electrically conducting phase during percolation charge transfer over the electrified surface. The analysis is made using the percolation model of electret charge relaxation[1] based on the combined application of percolation theory[2–4] and the Kolmogorov model[5] for the kinetics of two-dimensional nucleation. These surface relaxation processes of the charge determine the stability of electrets in various devices under real operating conditions, whereas charge transfer across the bulk of the dielectric appears mainly when studying the physical properties of electret materials using various methods of thermally stimulated discharge.

Adsorption of water leads to the appearance of conducting channels on the electrified surface which substantially alter its electrical properties. Since water is a considerably better electrical conductor than the electret material, these channels shunt the surface of the sample, resulting in strong local inhomogeneity of the surface electrical conductivity. When the fraction of the surface coated with adsorbate reaches the percolation threshold, the conducting channels form an infinite percolation cluster along which the excess charges flow off. This cluster shunts the surface of the sample so that all parts of the electrified surface adjacent to the percolation cluster stop making any contribution to the surface potential of the electret U. From this it follows that $U \propto 1-P$, where P is the density of the percolation cluster, which is equal to the probability that a randomly located surface point belongs to an infinite cluster. The density of the percolation cluster depends on the fraction of the surface occupied by the adsorbate θ at time t: $P=P(\theta)$, where $\theta=\theta(t)$. In order to determine the adsorption kinetics, we shall use the Kolmogorov theory which describes the growth of new-phase nuclei in a steady-state reaction space of arbitrary dimensions.[5] It is taken that all the initial assumptions of this theory are satisfied (unbounded reaction space, Poisson nucleation law, geometric similarity of nuclei, uniform growth rate).

In this case, for any time after electrification, which has taken place at $t=\tau_0$, the kinetics of the adsorbed phase on the electret surface has the form

$$\theta(t)=1-Q(\tau_0,t)\exp\left(-\int_{\tau_0}^{t}\alpha(\zeta)S(R_2(\zeta,t))d\zeta\right), \quad (1)$$

where

$$Q(\tau_0,t)\equiv\exp\left(-\int_{0}^{\tau_0}\alpha(\zeta)S(R_1(\zeta,\tau_0)+R_2(\tau_0,t))d\zeta\right). \quad (2)$$

The functional $R(\zeta,t)\equiv\int_{\zeta}^{t}v(\eta)d\eta$ determines the radius which a nucleus formed at time ζ will have by time t, $v=v(t)$ is the growth rate of the nucleus, $S=S(R)$ is the area of an isolated nucleus of radius R, and $\alpha=\alpha(t)$ is the rate of nucleation, which is equal to the average number of adsorption centers formed per unit area per unit time. The relationship $R=R(\zeta,t)$ determines the geometric growth law for the adsorbate nuclei. A nucleus formed after electrification has the radius $R=R_2(\zeta,t)$; otherwise the radius is $R=R_1(\zeta,t)$ before electrification and $R=R_1(\zeta,\tau_0)+R_2(\tau_0,t)$ during subsequent growth. The function $Q(\tau_0,t)$, as given by formula (2), describes the growth of all nuclei formed before electrification and is numerically equal to the fraction of the electret surface not occupied by such nuclei at time t. From the time of fabrication of the future electret material ($t=0$) until electrification ($t=\tau_0$), the surface of the material interacts with the surrounding medium. After thermodynamic equilibrium has been established, the fraction of the surface occupied by the adsorbate will remain constant provided that the sample is under controlled steady-state conditions. In this case, $Q(\tau_0,t)$ may be replaced by the time-independent function $Q(\tau_0)$ which is equal to the fraction of the surface left free of adsorbate before electrification. Electrification is accompanied by the formation of a large number of new nucleation centers as a result of which the adsorption process is intensified appreciably, being activated by the self-induced electric field of the electret. Good agreement with the experimental data on the decay of the surface potential of Teflon electrets is achieved by using the following expression for the rate of nucleation:

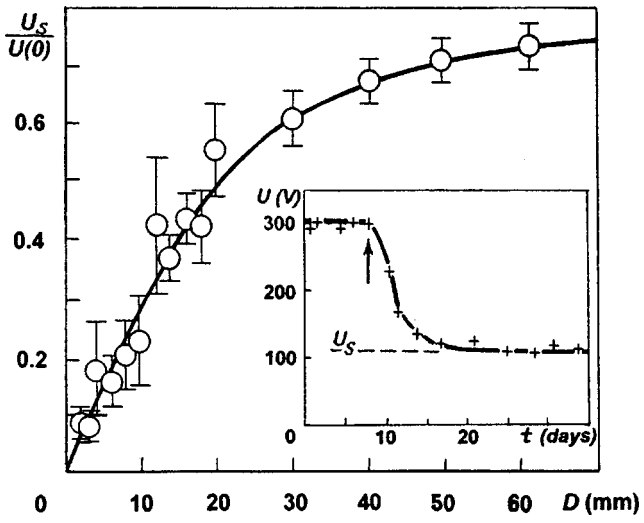

FIG. 1. Limiting values of the surface potential U_s for electrets of various sizes. The confidence interval is given for 95% probability. The inset shows the characteristic decay curve of the surface potential for a Teflon electret having the area $D^2=10\times10\ \text{mm}^2$ at room temperature and 98% relative humidity. The arrow indicates the percolation transition.

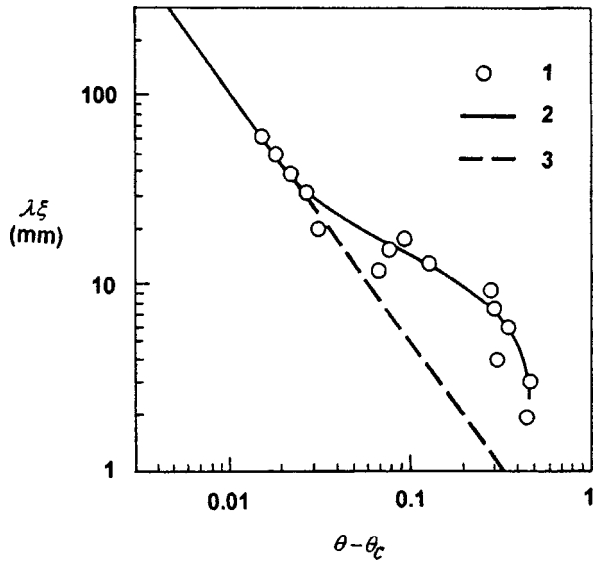

FIG. 2. Estimate of the critical index of the correlation length: *1* — experimental data, *2* — optimum approximation, and *3* — scaling asymptote.

$\alpha(t)=\beta\delta(t-\tau_0)+\alpha_0$, where β is the concentration of nucleation centers appearing during electrification, $\delta(t)$ is the Dirac delta function, and α_0 is the constant rate of spontaneous nucleation which continues over the entire electret discharging process. Thus, both instantaneous nucleation during electrification and the constant nucleation during subsequent storage (operation) of the electret are taken into account.

After shifting the time measurement by the interval τ_0, which corresponds to electrification at $t=0$, Eq. (1) may be simplified:

$$\theta(t)=1-Q(0)\exp\left(-\int_0^t \alpha(\zeta)S(R_2(\zeta,t))d\zeta\right). \qquad (3)$$

As the surface of the electret fills with adsorbate, a percolation cluster forms. The stability of the electret charge is highest until the fraction of the surface occupied by the adsorbate exceeds the percolation threshold. As soon as an infinite cluster forms, a percolation transition takes place and the surface potential of the electret begins to fall. The inset to Fig. 1 shows the characteristic decay curve of the surface potential for the case where a percolation transition took place eight days after electrification. When an infinite cluster forms before the end of electrification, the electret undergoes catastrophic discharging (percolation breakdown). Both types of percolation transitions have been observed experimentally.[6,7]

As the electrified surface becomes covered with a network of conducting channels, the discharging process slows down: after a relatively rapid drop observed after the percolation transition, the surface potential reaches saturation, with only a slight variation around some limiting value U_S (inset to Fig. 1). In this case, the correlation length of the percolation cluster becomes considerably shorter than the characteristic geometric dimension of the electret.

The percolation nature of the surface relaxation of electret charges is confirmed by the good agreement between the experimental and theoretical values of the critical index of the correlation length. In accordance with the concept of scale invariance,[4,8–10] the correlation length is the only geometric dimension characterizing a percolation cluster near the percolation threshold. We assume that when the surface potential saturates, the correlation length ξ is proportional to the characteristic electret dimension D. This means that the limiting value of the surface potential can be defined as $U_S=U(t)=t_S|\xi\propto D)$, where t_S is the time at which saturation is reached. Thus, when the surface potential saturates, the correlation length, apart from the constant factor λ, is equal to the electret dimension: $D=\lambda\xi$. From this it follows that large electrets should have high limiting values of the surface potential. Figure 1 gives experimental data which support this conclusion for Teflon electrets exposed to 98% humidity at room temperature for three months. Teflon was selected because it is one of the best electret materials. The points for $D=2$ mm and $D=3$ mm were obtained by averaging the limiting surface potential over nine identical samples, and the other points were obtained by averaging over five. The initial surface potential was $U(0)=300$ V for all the electrets whereas the limiting values under saturation were between 30 V and 210 V depending on the electret size. Since the surface potential is uniquely determined by the density of the percolation cluster which in turn depends on the fraction of the surface coated with adsorbate, the experimental data on the limiting surface potentials of electrets of different sizes can be used to obtain the dependence of $\lambda\xi$ on θ. The result is plotted in Fig. 2. Each point on the graph was obtained by converting the limiting surface potential (Fig. 1) into the difference between the fractions of surface occupied by adsorbate and the percolation threshold θ_C: ($\theta_C=0.5$ for two-dimensional continual percolation).

The correlation length near the percolation threshold obeys the following scaling law:[8,9]

$$\xi \propto |\theta - \theta_C|^{-\nu}, \quad 0 < \theta - \theta_C \ll 1, \tag{4}$$

where ν is the critical index of the correlation length for two-dimensional percolation. Thus, the value of this index can be determined from the slope of the scaling asymptote of the function $\{\lambda \xi vs(\theta - \theta_C)\}$, plotted on a logarithmic scale. A corresponding plot is shown in Fig. 2. An optimum approximation can be used to find the slope of the asymptote near the percolation threshold where relation (4) is valid. The critical index of the correlation length thus determined was $\nu = 1.4 \pm 0.1$, which agrees with known theoretical estimates for two-dimensional percolation.[4,8,11]

The formation of a percolation cluster near the percolation threshold is closely related to the growth of adsorbate nuclei. Here we studied the relationship between the local growth rate of conducting-phase nuclei and the integral propagation velocity of the potential drop accompanying the formation of conducting channels on the electrified surface. This potential drop propagates as the various surface points become electrically coupled during the formation of the percolation cluster. The integral propagation velocity V of the potential drop is appreciably higher than the local growth rate of an isolated nucleus v: $V = (2n-1)$, where n is the number of nucleation centers over the distance $L(t) = \int_0^t V(\eta) d\eta$ covered by the potential drop in the time t. Measurements were made of the limiting distances $L(\infty)$ over which the surface potential drop propagates on an electrified surface exposed to increased moisture. Data on the adsorption of water on Teflon were analyzed using equations for the three main adsorption isotherms: Brunauer–Emmett–Teller, Langmuir, and Henry. It was found that the growth rate of adsorbate nuclei is well approximated by the exponential law: $v(t) = v_0 \exp(-t/\tau)$, where τ is the relaxation time of the growth rate and $v_0 \equiv 1/(2\tau\beta^{1/2})$. For exponential relaxation of the growth rate the limiting distance $L(\infty)$ covered by the potential drop over an infinitely long time is finite whereas for a constant or hyperbolically decaying growth rate this distance becomes infinitely long. The exponential relaxation of the growth rate was also confirmed directly by the possibility of linearizing the experimental data with respect to the limiting propagation distances of the surface potential drop in terms of the coordinates: $\{\ln(L(\infty) - L(t)) vst\}$.

To sum up, it has been established that the charge transfer over an electrified surface is of a percolation nature as a result of the adsorption of a conducting phase stimulated by the electric field. If the adsorption and nucleation kinetics accompanying the formation of a percolation cluster are known, the surface relaxation of the charge can be described quantitatively and the stability of electrets under real operating conditions can be predicted.

[1] Yu. I. Kuz'min and V. N. Tairov, Zh. Tekh. Fiz. **54**, 964 (1984) [Sov. Phys. Tech. Phys. **29**, 575 (1984)].
[2] S. R. Broadbent and J. M. Hammersley, Proc. Cambridge Philos. Soc. **53**, 629 (1957).
[3] J. M. Hammersley and S. R. Broadbent, Proc. Cambridge Philos. Soc. **53**, 641 (1957).
[4] D. Stauffer, Phys. Rep. **54**(1), 2 (1979).
[5] A. N. Kolmogorov, Izv. Akad. Nauk SSSR, Ser. Mat. 355 (1937).
[6] Yu. I. Kuzmin, N. S. Pshchelko, I. M. Sokolova, and V. I. Zakrzhevskiy, *The Percolation Behavior of Electrets in the Presence of Water Condensation*, in *Proceedings of the Eighth International Symposium on Electrets*, edited by J. Lewiner, D. Morisseau, and C. Alquié, ESPCI, IEEE (Paris, France, 1994), pp. 124–129.
[7] B. Cantaloube, G. Dreyfus, and J. Lewiner, J. Polym. Sci., Part B: Polym. Phys. **17**(1), 95 (1979).
[8] P. G. de Gennes, *Scaling Concepts in Polymer Physics* (Cornell University Press, Ithaca, NY, 1979; Mir, Moscow, 1982).
[9] H. Kesten, *Percolation Theory for Mathematicians* (Birkhauser, Boston, MA, 1982; Mir, Moscow, 1986).
[10] K. Sumithra and A. Baumgaertner, J. Chem. Phys. **110**, 2727 (1999).
[11] J. Kurkijarvi and T. C. Padmore, J. Phys. A **8**, 683 (1975).

Translated by R. M. Durham

Electrical tuning of the dispersion characteristics of spin waves in metal–ferroelectric–ferrite–ferroelectric–metal layered structures

V. E. Demidov and B. A. Kalinikos

St. Petersburg State Electrotechnical University
(Submitted July 6, 1999)
Pis'ma Zh. Tekh. Fiz. **25**, 86–94 (November 12, 1999)

A theoretical analysis is made of the spin wave spectrum in a tangentially magnetized metal–ferroelectric–ferrite–ferroelectric–metal layered film structure. An analysis is made of the dispersion dependences of the transverse spin waves for the technically simplest layered structure. It is shown that a change in the permittivity of the ferroelectric film by a factor of two may change the wave number of the spin wave, which can reach $40\,\mathrm{cm}^{-1}$ and consequently changes the phase shift of the wave to 10π rad over a propagation length of 1 cm. © *1999 American Institute of Physics.* [S1063-7850(99)01511-6]

One of the main advantages of spin-wave devices for processing microwave signals is that these can be tuned electrically. This tuning is accomplished by varying the intensity of the magnetizing field in which the ferrite film is situated. This type of magnetic tuning can change the characteristics of devices over a wide range. However, it has many disadvantages which include the comparatively cumbersome magnetic systems, the low tuning speed, and high energy consumption.

Recently published studies have examined the use of ferroelectric materials for tuning microwave devices. The renewed interest in this problem, which was earlier studied intensively in the seventies,[1] is attributable to the significant successes recently achieved in the synthesis of high-quality ferroelectric films. Modern ferroelectric films have high permittivities which can be varied widely by applying an external electric field, and they have a low dielectric loss tangent at microwave frequencies.[2] Nonlinear ferroelectric film capacitors have been used to develop various microwave devices such as filters, phase shifters, switches, and so on (see, for example, Ref. 3). Studies of the tuning speed of these devices have shown that the characteristic times of variation of the permittivity of ferroelectric films exposed to voltage videopulses do not exceed a few tens of nanoseconds.[4]

The aim of the present study is to make a theoretical analysis of the spectrum of dipole-exchange spin waves in tangentially magnetized metal–ferroelectric–ferrite–ferroelectric–metal (MFFFM) layered film structures and to examine the possibility of using these structures in electrically tunable microwave devices. The physical prerequisite for this study was that by slowing the electromagnetic waves in the ferrite medium, the wave number shift accompanying the change in permittivity may appreciably exceed that for fast waves in a pure dielectric waveguide.

The spectrum of dipole-exchange spin waves in metal–dielectric–ferrite–dielectric–metal (MDFDM) layered structures was analyzed in Ref. 5. However, the theory in Ref. 5 was constructed in the magnetostatic approximation, i.e., neglecting the electromagnetic delay, which means that these results cannot be used to describe MFFFM structures.

In the present study the problem of the wave spectrum in an MFFFM structure was solved by jointly integrating the equation of motion for the magnetization and the complete system of Maxwell equations. For this we used a theoretical approach based on the Green functions of the system of Maxwell equations, developed earlier to describe the properties of dipole-exchange spin waves in ferromagnetic films.[5,6] An analysis was made of a plane-parallel layered structure unbounded in the YZ plane, consisting of an isotropic ferromagnetic film of thickness L having the saturation magnetization M_0 and permittivity ϵ_L, separated on both sides from ideally conducting metal screens by dielectric layers having thicknesses a and b and permittivities ϵ_A and ϵ_B, respectively (Fig. 1). The ferromagnetic film was magnetized to saturation by a uniform static magnetic field of intensity H_0 applied along the Z axis. In order to solve the problem, we assumed that inhomogeneous plane waves $\exp(i\times(\omega t-k_\zeta\zeta))$ having the wave number k_ζ lying in the YZ plane can propagate in an arbitrary direction to the static magnetic field. The direction of wave propagation was defined by the angle φ.

As a result, we obtained a transcendental dispersion equation which describes the relationship between the wave frequency ω and the wave number k_ζ. For the nth natural wave this equation has the form:

$$(\Omega_{nk}-\omega_M A_n^{xx})[\Omega_{nk}-\omega_M(A_n^{yy}\cos^2\varphi+A_n^{zz}\sin^2\varphi)] - (\omega_n+\omega_M A_n^{xz}\sin\varphi)(\omega_n-\omega_M A_n^{zx}\sin\varphi)=0, \quad (1)$$

where

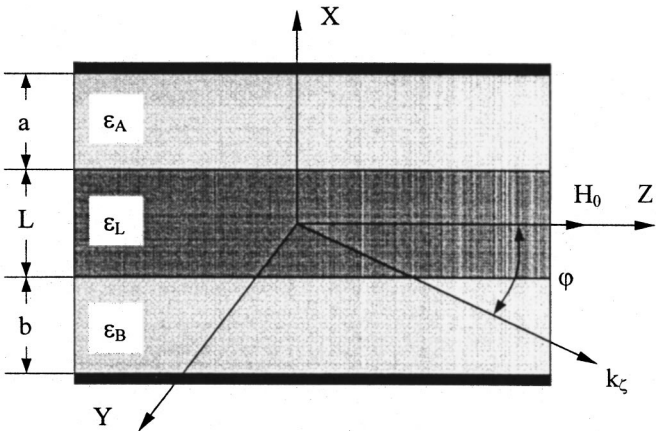

FIG. 1. Structure geometry.

$$A_n^{xx}=\frac{k_0^2-\kappa_n^2}{\gamma^2+\kappa_n^2}-\frac{k_\zeta^2\gamma}{\sinh(\gamma d)(\gamma^2+\kappa_n^2)^2}\frac{2}{L(1+\delta_{0n})}\times(C_n^{10}\cosh(\gamma b)-C_n^{11}\cosh(\gamma a))+\frac{k_\zeta^2}{\gamma N}\frac{1}{\gamma_L^2+\kappa_n^2}\frac{2}{L(1+\delta_{0n})}\times\left[T_BI_n^1+T_B\frac{\gamma_L}{\gamma_B}\tanh(\gamma_Bb)I_n^2+T_AI_n^3+T_A\frac{\gamma_L}{\gamma_A}\tanh(\gamma_Aa)I_n^4\right],$$

$$A_n^{yy}=\frac{k_0^2}{\gamma^2+\kappa_n^2}+\frac{k_0^2\gamma}{\sinh(\gamma d)(\gamma^2+\kappa_n^2)^2}\frac{2}{L(1+\delta_{0n})}\times(C_n^{9}\sinh(\gamma b)-C_n^{12}\sinh(\gamma a))+\frac{k_0^2\gamma_L}{\gamma^2N}\frac{1}{\gamma_L^2+\kappa_n^2}\frac{2}{L(1+\delta_{0n})}\times\left[T_BI_n^5+T_B\frac{\gamma_L}{\gamma_B}\tanh(\gamma_Bb)I_n^6+T_AI_n^7+T_A\frac{\gamma_L}{\gamma_A}\tanh(\gamma_Aa)I_n^8\right],$$

$$A_n^{xz}=\frac{k_\zeta\gamma^2}{\sinh(\gamma d)(\gamma^2+\kappa_n^2)^2}\frac{2}{L(1+\delta_{0n})}\times(C_n^{9}\cosh(\gamma b)+C_n^{12}\cosh(\gamma a))-\frac{k_\zeta}{N}\frac{1}{\gamma_L^2+\kappa_n^2}\frac{2}{L(1+\delta_{0n})}\times\left[T_BI_n^6+T_B\frac{\gamma_L}{\gamma_B}\tanh(\gamma_Bb)I_n^5+T_AI_n^8+T_A\frac{\gamma_L}{\gamma_A}\tanh(\gamma_Aa)I_n^7\right],$$

$$A_n^{zx}=\frac{k_\zeta\gamma^2}{\sinh(\gamma d)(\gamma^2+\kappa_n^2)^2}\frac{2}{L(1+\delta_{0n})}(C_n^{10}\sinh(\gamma b)+C_n^{11}\sinh(\gamma a))-\frac{k_\zeta}{N}\frac{\gamma_L}{\gamma}\frac{1}{\gamma_L^2+\kappa_n^2}\frac{2}{L(1+\delta_{0n})}\times\left[T_BI_n^2+T_B\frac{\gamma_L}{\gamma_B}\tanh(\gamma_Bb)I_n^1+T_AI_n^4+T_A\frac{\gamma_L}{\gamma_A}\tanh(\gamma_Aa)I_n^3\right],$$

$$A_n^{zz}=-\frac{\gamma^2}{\gamma^2+\kappa_n^2}+\frac{\gamma^3}{\sinh(\gamma d)(\gamma^2+\kappa_n^2)^2}\frac{2}{L(1+\delta_{0n})}\times(C_n^{9}\sinh(\gamma b)-C_n^{12}\sinh(\gamma a))+\frac{\gamma_L}{N}\frac{1}{\gamma_L^2+\kappa_n^2}\frac{2}{L(1+\delta_{0n})}\times\left[T_BI_n^5+T_B\frac{\gamma_L}{\gamma_B}\tanh(\gamma_Bb)I_n^6+T_AI_n^7+T_A\frac{\gamma_L}{\gamma_A}\tanh(\gamma_Aa)I_n^8\right],$$

$$N=\sinh(\gamma d)\left[\cosh(\gamma_LL)\left(\frac{\gamma_L}{\gamma_B}\tanh(\gamma_Bb)+\frac{\gamma_L}{\gamma_A}\tanh(\gamma_Aa)\right)+\sinh(\gamma_LL)\times\left(1+\frac{\gamma_L^2}{\gamma_A\gamma_B}\tanh(\gamma_Aa)\tanh(\gamma_Bb)\right)\right],$$

$$T_A=\sinh(\gamma a)-\frac{\gamma}{\gamma_B}\tanh(\gamma_Bb)\cosh(\gamma a),$$

$$T_B=-\sinh(\gamma b)+\frac{\gamma}{\gamma_A}\tanh(\gamma_Aa)\cosh(\gamma b),$$

$$I_n^1=-1/4(C_n^1K_n^++C_n^5K_n^-)+D_nC_n^{10},$$

$$I_n^2=-1/4(C_n^2K_n^+-C_n^6K_n^-)+D_nC_n^{10},$$

$$I_n^3=1/4(C_n^3K_n^++C_n^7K_n^-)-D_nC_n^{11},$$

$$I_n^4=1/4(C_n^4K_n^++C_n^8K_n^-),$$

$$I_n^5=-1/4(C_n^1K_n^+-C_n^5K_n^-)+D_nC_n^{9},$$

$$I_n^6=-1/4(C_n^2K_n^+-C_n^6K_n^-)+D_nC_n^{9},$$

$$I_n^7=-1/4(C_n^3K_n^+-C_n^7K_n^-),$$

$$I_n^8=1/4(C_n^4K_n^+-C_n^8K_n^-)+D_nC_n^{12},$$

$$K_n^+=\frac{\gamma_L}{\gamma+\gamma_L}+\frac{\gamma_L(\gamma+\gamma_L)-2\kappa_n^2}{(\gamma+\gamma_L)^2+(2\kappa_n)^2},$$

$$K_n^- = \frac{\gamma_L}{\gamma - \gamma_L} + \frac{\gamma_L(\gamma - \gamma_L) - 2\kappa_n^2}{(\gamma - \gamma_L)^2 + (2\kappa_n)^2},$$

$$C_n^1 = \cosh((\gamma + \gamma_L)L + \gamma a) - \cosh(\gamma a),$$

$$C_n^2 = \sinh((\gamma + \gamma_L)L + \gamma a) - \sinh(\gamma a),$$

$$C_n^3 = \cosh(\gamma_L L - \gamma b) - \cosh(\gamma(L + b)),$$

$$C_n^4 = \sinh(\gamma_L L - \gamma b) + \sinh(\gamma(L + b)),$$

$$C_n^5 = \cosh((\gamma - \gamma_L)L + \gamma a) - \cosh(\gamma a),$$

$$C_n^6 = \sinh((\gamma - \gamma_L)L + \gamma a) - \sinh(\gamma a),$$

$$C_n^7 = \cosh(\gamma_L L + \gamma b) - \cosh(\gamma(L + b)),$$

$$C_n^8 = \sinh(\gamma_L L + \gamma b) - \sinh(\gamma(L + b)),$$

$$C_n^9 = -\sinh(\gamma a)(-1)^n + \sinh(\gamma(L + a)),$$

$$C_n^{10} = -\cosh(\gamma a)(-1)^n + \cosh(\gamma(L + a)),$$

$$C_n^{11} = -\cosh(\gamma b)(-1)^n - \cosh(\gamma(L + b)),$$

$$C_n^{12} = \sinh(\gamma b)(-1)^n - \sinh(\gamma(L + b)).$$

The following notation is introduced above:

$$D_n = \frac{\gamma \gamma_L}{\gamma^2 + \kappa_n^2},$$

$$\gamma^2 = k_\zeta^2 - k_0^2, \quad k_0^2 = \omega^2 \epsilon_0 \mu_0,$$

$$\gamma_L^2 = k_\zeta^2 - k_L^2, \quad k_L^2 = \omega^2 \epsilon_0 \mu_0 \epsilon_L,$$

$$\gamma_A^2 = k_\zeta^2 - k_A^2, \quad k_A^2 = \omega^2 \epsilon_0 \mu_0 \epsilon_A,$$

$$\gamma_B^2 = k_\zeta^2 - k_B^2, \quad k_B^2 = \omega^2 \epsilon_0 \mu_0 \epsilon_B,$$

$$d = a + b + L.$$

The remaining notation is the same as in Ref. 5.

This equation is approximate since it was obtained in the first order of perturbation theory. The limits of validity of this approximation were investigated in Ref. 6.

The expressions for the matrix elements A_{ij}^n are given for the case of exchange boundary conditions corresponding to free surface spins. This case is the most favorable from the point of view of the influence of the properties of the ferroelectric layers on the spin wave spectrum.

The dispersion equation (1) was solved numerically for various values of the parameters. As a result, it was established that a change in the permittivity of the ferroelectric layers has the greatest influence on the dispersion of spin waves propagating perpendicular to the static magnetizing field ($\varphi = 90°$).

Figure 2a gives dispersion dependences of the spin wave in the lowest mode $n = 0$ for the technically simplest variant of a layered structure. This structure is a ferrite film having a thick substrate of low permittivity on one side and a ferroelectric film on which a metal control structure is formed, on the other. The figure only shows the slow branches of the spectrum. For thicknesses $a = 50$, 100, and 200 μm, the electromagnetic (fast) waves have cutoff frequencies of 50, 25, and 12 GHz, respectively. The corresponding dependences $\omega(k_\zeta)$ are not plotted in the figure. For the calculations we took: $L = 20\,\mu$m, $b \to \infty$, $\epsilon_L = 14$, $\epsilon_B = 14$, $\epsilon_A = 1000$, $M_0 = 1750$ G, $H_0 = 3000$ Oe. The figures on the curves correspond to the thickness of the ferroelectric layer a.

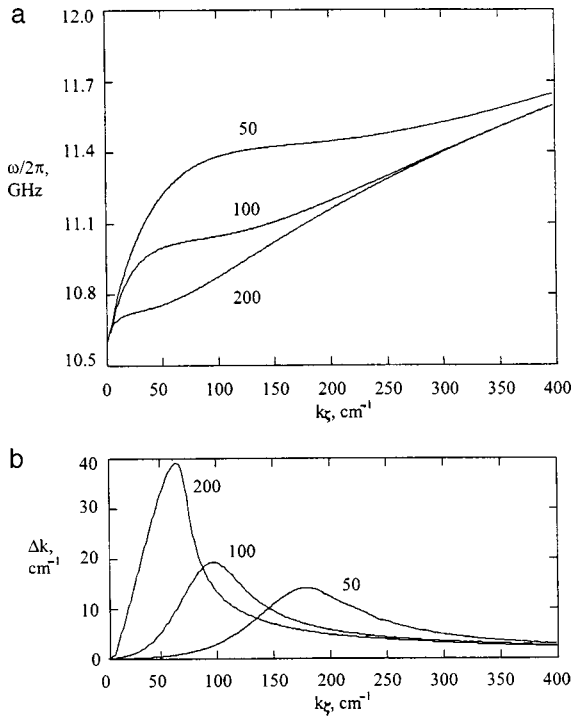

FIG. 2. Dispersion characteristics (a) and wave number shift as a function of the absolute value of the wave number when ϵ_A varies between 1000 and 500 for various dielectric layer thicknesses (b).

Figure 2b gives the wave number shift Δk as a function of the absolute value of the wave number k_ζ when ϵ_A varies between 1000 and 500 (the selected values of ϵ_A correspond to the characteristics of existing ferroelectric film materials). It can be seen that this dependence has a maximum. The position and magnitude of the maximum depend on the thickness of the ferroelectric layer. As a increases, the maximum shifts toward lower wave numbers and increases in

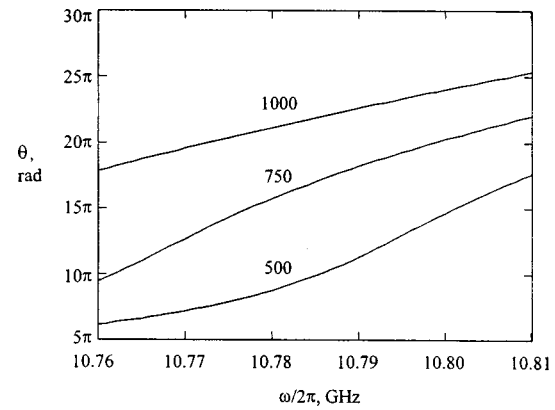

FIG. 3. Frequency dependence of the wave phase shift over a 1 cm propagation length for various values of ϵ_A.

absolute value. For $a=200\,\mu$m the shift Δk has values of around $40\,\mathrm{cm}^{-1}$.

This nonmonotonic behavior of $\Delta k(k_\zeta)$ can be attributed to ''repulsion'' of the dispersion branches of the fast and slow waves. The thicker the dielectric layer, the closer lie the branches of the spin and fast electromagnetic waves and the stronger their hybridization. A change in ϵ_A leads to a proportional change in the cutoff frequency and this is accompanied by a change in the hybridization. The optimum situation from the point of view of controlling the spin wave spectrum is achieved for those values of H_0, a, and ϵ_A for which the cutoff frequency of the fast waves is slightly higher than the beginning of the spin wave spectrum. For $H_0=3000\,\mathrm{Oe}$ and $\epsilon_A=1000$ the optimum value of a is around $200\,\mu$m.

An investigation of the wave number shift as a function of the ferrite film thickness showed that an increase in L ''amplifies'' the tuning. However, for films more than $50\,\mu$m thick the $\omega(k_\zeta)$ spectrum becomes highly nonmonotonic, which may be inconvenient for constructing specific devices.

Figure 3 shows calculated characteristics of a phase shifter using a metal–ferroelectric–ferrite structure with the parameters described above for the case $a=200\,\mu$m. The wave propagation length was taken to be 1 cm. The numbers on the curves correspond to the values of ϵ_A used in the calculations. It can be seen that when the permittivity of the ferroelectric film decreases from 1000 to 500, a change in the phase shift is observed which reaches 10π rad in a frequency range of a few tens of megahertz.

These results show that layered MFFFM structures can be used in practice to fabricate spin-wave devices whose operating characteristics are effectively controlled by an electric field.

This work was financed by the Russian Foundation for Basic Research (Grant No. 99-02-16370) and by the Ministry of General and Professional Education of the Russian Federation (Grant No. 97-8.3-13).

[1] *Ferroelectrics in Microwave Technology*, edited by O. G. Vendik (Sovetskoe Radio, Moscow, 1979), 272 pp.
[2] M. J. Lancaster, J. Powell, and A. Porch, Supercond. Sci. Technol. **11**, 1323 (1998).
[3] A. A. Golovkov, D. A. Kalinikos, A. B. Kosyrev, and T. B. Samoilova, Electron. Lett. **34**, 1389 (1998).
[4] A. B. Kozyrev, O. I. Soldatenkov, and A. V. Ivanov, Pis'ma Zh. Tekh. Fiz. **24**(19), 19 (1998) [Tech. Phys. Lett. **24**, 755 (1998)].
[5] V. F. Dmitriev and B. A. Kalinikos, Izv. Vyssh. Uchebn. Zaved. Fiz. **31**(11), 24 (1988).
[6] B. A. Kalinikos, Izv. Vyssh. Uchebn. Zaved. Fiz. **24**(8), 42 (1981).

Translated by R. M. Durham

Instability of the stressed surface of a highly viscous liquid

D. F. Belonozhko and A. I. Grigor'ev

P. G. Demidov State University, Yaroslavl
(Submitted July 12, 1999)
Pis'ma Zh. Tekh. Fiz. **25**, 1–6 (November 26, 1999)

A new type of hydrodynamic instability is observed in a highly viscous liquid whose free surface is exposed to an external force acting at a certain angle to the normal. The physical reason for this instability is the redistribution of energy between the tangential and normal components of the free surface stresses. © *1999 American Institute of Physics.* [S1063-7850(99)01611-0]

The formation of a wave-like relief on an initially flat surface of a highly viscous material exposed to some force when both normal and tangential stresses are created on the surface is well-known and utilized in engineering and technology. Examples may include shock welding (explosive welding) or the formation of a wavy relief on a solid silicon surface exposed to a high-energy atomic beam.[1,2] The experimental data forming the basis of these phenomena have not yet received an adequate theoretical interpretation and in this context the problem solved below is of some interest.

1. We shall assume that a planar liquid film of density ρ, kinematic viscosity ν, and thickness d on a solid substrate in a gravitational field $\mathbf{g}$ is exposed to a continuous force as a result of a momentum flow, oblique with respect to the normal, imparted for example by some material beam, being incident on its free surface. The capillary motion spectrum in the liquid layer needs to be determined.

Let us assume that $\Pi^*_{ij}=\rho^* U^*_i U^*_j$ is the tensor of the momentum flow density of the external force above the surface of the liquid, where U_i are the components of the beam velocity and ρ^* is its bulk density.[2] For simplicity we shall solve the two-dimensional problem using XZ Cartesian coordinates with the Z axis directed vertically upward ($\mathbf{n}_z \| -\mathbf{g}$), when the equation for the perturbed free liquid interface has the form $z=\xi(x,t)$, that for the unperturbed interface is $z=0$, and the solid bottom is located at $z=-d$. Phenomena associated with an influx of material into the liquid will be neglected. Neglecting small-amplitude waves, the complete mathematical formulation of the problem has the form:

$$\frac{\partial \mathbf{U}}{\partial t}+(\mathbf{U}\cdot\nabla)\mathbf{U}=-\frac{1}{\rho}\nabla P+\Delta\mathbf{U}+\mathbf{g}; \tag{1}$$

$$\operatorname{div}\mathbf{U}=0; \tag{2}$$

$$z=\xi; \quad \frac{\partial \xi}{\partial t}=U_z-U_x\frac{\partial \xi}{\partial x}; \tag{3}$$

$$\Pi^*_{ij}n^*_j+\Pi_{ij}n_{ij}=P_\gamma n_i; \tag{4}$$

$$P_\gamma=-\frac{\partial^2 \xi}{\partial x^2}; \quad n_i=\begin{bmatrix} -\dfrac{\partial \xi}{\partial x} \\ 1 \end{bmatrix}; \quad n^*_i=\begin{bmatrix} \dfrac{\partial \xi}{\partial x} \\ -1 \end{bmatrix};$$

$$\Pi^*_{ij}=\begin{bmatrix} \rho^*(U^*_x)^2 & \rho^* U^*_x U^*_z \\ \rho^* U^*_x U^*_z & \rho^*(U^*_x)^2 \end{bmatrix};$$

$$\Pi_{ij}=\begin{bmatrix} \rho U_x^2+P-2\rho\nu\dfrac{\partial U_x}{\partial x} & \rho U_x U_z-\rho\nu\left(\dfrac{\partial U_x}{\partial z}+\dfrac{\partial U_z}{\partial x}\right) \\ \rho U_x U_z-\rho\nu\left(\dfrac{\partial U_x}{\partial z}+\dfrac{\partial U_z}{\partial x}\right) & \rho U_x^2+P-2\rho\nu\dfrac{\partial U_x}{\partial x} \end{bmatrix};$$

$$z=-d; \quad U_x=U_z=0. \tag{5}$$

Here P_γ is the Laplace pressure below the distorted liquid surface,[3] γ is the surface tension, n_i is the column of vector coordinates of the normal external to the liquid surface, n^*_i is the column vector of the internal normal, and the square matrices Π^*_{ij} and Π_{ij} are made up of the components of the momentum flow density tensors above and below the perturbed surface.[3]

It is difficult to obtain a correct solution of the formulated problem by perturbation theory methods because of the presence of the term $(\mathbf{U}\cdot\nabla)\mathbf{U}$ in Eq. (1), which generally has components of all orders of smallness. However, the proximity of the bottom and the high viscosity of the liquid may create conditions when this term can be neglected, at least to a first approximation. An analysis of the problem (1)–(5) in the zeroth approximation showed that if the following condition is satisfied

$$U_0^* \ll \frac{\omega_0}{k}; \quad U_0^* \equiv |U_x^* U_z^*| \frac{\rho^* d}{\rho \nu}; \quad \omega_0^2 \equiv \frac{k}{\rho}(\gamma k^2 + \rho g),$$

the term $(\mathbf{U}\cdot\nabla)\mathbf{U}$ has no more than the first order of smallness with respect to the perturbation amplitude ξ (U_0^* is the velocity of the steady-state surface flow of liquid induced by the tangential stress and ω_0 is the oscillation frequency corresponding to the wave number k for a nonviscous, infinitely deep liquid). In compact form, the condition for neglecting the nonlinear term in Eq. (1) has the form:

$$\frac{|U_x^* U_z^*| d}{\nu \sqrt{\gamma k/\rho + g/k}} \frac{\rho^*}{\rho} \ll 1. \tag{6}$$

2. We shall assume that condition (6) is satisfied so that we can linearize the problem (1)–(5) and can use a classical method[3,4] to investigate its stability with respect to perturbations of the type $\xi = \xi_0 \exp(st - ikx)$, where s is the complex frequency and k is the wave number. In dimensionless variables in which $\rho = \gamma = g = 1$, the dispersion equation for the linearized problem is given by:

$$\begin{aligned} & k^2 q\left[4s(k^2+q^2) - (3k^2+q^2)\frac{W}{\nu}\right] + \frac{s\omega_0^2}{\nu^2} \\ & \times [k\cosh(kd)\sinh(qd) - q\sinh(kd)\cosh(qd)] \\ & - 2k^3 q\left[2s - \frac{W}{\nu}\right][k\cosh(kd)\cosh(qd) \\ & - q\sinh(kd)\sinh(qd)] + (k^2+q^2)\left[s(k^2+q^2) - k^2\frac{W}{\nu}\right] \\ & \times [k\cosh(kd)\cosh(qd) - q\sinh(kd)\sinh(qd)] = 0; \end{aligned} \tag{7}$$

$$\omega_0^2 \equiv k(k+1); \quad q^2 \equiv k^2 + s/\nu;$$

$$W \equiv \frac{\rho^*}{\rho}\left[\frac{\rho}{g\gamma}\right]^{\frac{1}{2}}[(U_x^*)^2 - (U_z^*)^2].$$

In formula (7) the quantities kd, qd, and W are dimensionless by definition and the variables k, s, and ν are dedimensionalized to their typical scales:

$$k' = \sqrt{\frac{\rho g}{\gamma}}; \quad s' = \left[\frac{g^3\rho}{\gamma}\right]^{\frac{1}{4}}; \quad \nu' = \left[\frac{\gamma^3}{g\rho^3}\right]^{\frac{1}{4}}.$$

3. A numerical analysis of the dispersion equation (7) showed that under the conditions described the surface of the liquid may become unstable (see Figs. 1 and 2). It can be seen from Fig. 1 that by increasing the horizontal velocity component of the beam incident on the free surface of the liquid (by increasing the parameter W), we can provoke the evolution of aperiodic instability which occurs in this case when $W \geqslant 2$ (positive part of branch *2*). In these calculations the depth of the liquid is finite ($kd = 1$) and the liquid itself is highly viscous ($|s/\nu k^2| \ll 1$). This explains why only aperiodic motion occurs for $W = 0$ and in its vicinity. It can be seen from Fig. 1 that for $W < 0$ oscillatory motion also occurs. Equation (7) has an infinite number of solutions,[5] but only the roots associated with the unstable branch are shown in the figures.

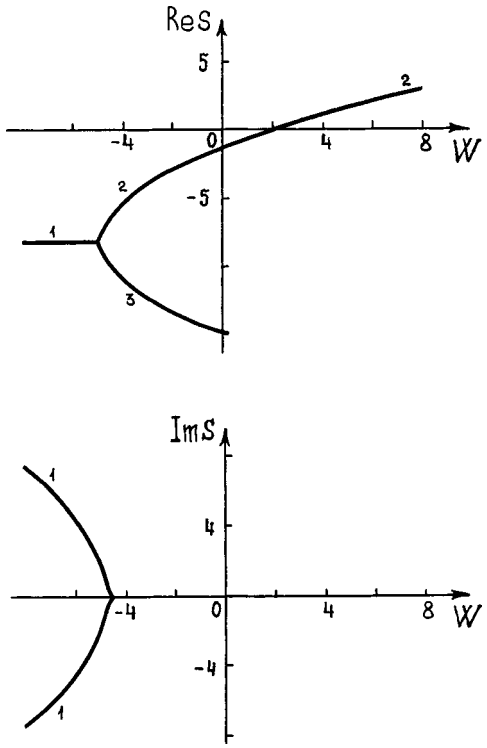

FIG. 1. Real $\mathrm{Re}\, s = \mathrm{Re}\, s(W)$ and imaginary $\mathrm{Im}\, s = \mathrm{Im}\, s(W)$ parts of the complex frequency as a function of the parameter W plotted for $k = 5$, $\nu = 0.5$, and $kd = 1$.

Instability of the small-scale motion can only be excited when the energy of the external action increases substantially, as can be seen from Fig. 2 which was obtained for $k = 100$ and the previous values of the other parameters. Instability is only observed for $W > 40$ but the oscillatory branches lie outside the range of the calculations.

It is easy to calculate that if $|U_x/U_z| = 10$, then for those values of the variables for which Fig. 1 is plotted, the following inequality is satisfied

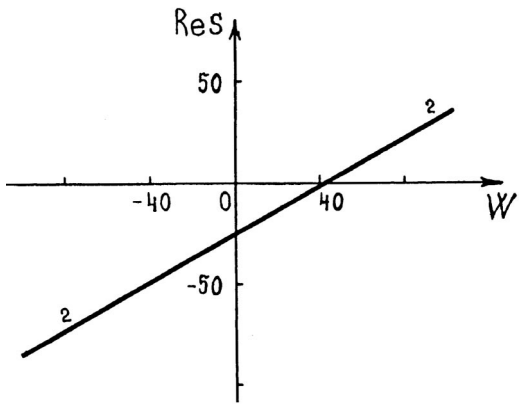

FIG. 2. Part of branch *2* entering the region $\mathrm{Re}\, s > 0$ on the dependence of the real part of the complex frequency $\mathrm{Re}\, s = \mathrm{Re}\, s(W)$ on the parameter W plotted for $k = 100$, $\nu = 0.5$, and $kd = 1$. Branches *1* and *3* lie outside the given range of W and $\mathrm{Re}\, s$ values.

$$\frac{|U_x^* U_z^*| d}{\nu\sqrt{\gamma k/\rho + g/k}} \frac{\rho^*}{\rho} < 0.2 \frac{\rho^*}{\rho}.$$

Thus, in accordance with condition (6), these calculations are reliable when the mass density of the beam is lower than the liquid density.

4. To conclude, a layer of highly viscous liquid of finite depth is unstable with respect to tangential stresses created by a continuous flow of momentum entering the liquid. The instability is observed in a linearized hydrodynamic model and exhibits aperiodic behavior. The physical nature of the instability is evidently caused by the energy of the tangential stresses at the free surface being transferred to the energy of the normal stresses.

[1] A. N. Dermin and A. N. Mikhaĭlov, in *Proceedings of the Fourth International Symposium on the Explosive Treatment of Metals* (Gottwaldov, Czechoslovakia, 1979) pp. 29–39.
[2] S. K. Aslanov, in *Abstracts of Papers presented at the 18th Conference of CIS Countries on ''Dispersed Systems''* (Odessa, Russia, 1998), pp 16–17.
[3] L. D. Landau and E. M. Lifshitz, *Fluid Mechanics*, (2nd ed., Pergamon Press, Oxford, 1987; 3rd. ed., Nauka, Moscow, 1986, 733 pp).
[4] V. G. Levich, *Physicochemical Hydrodynamics* (Fizmatgiz, Moscow, 1959), 699 pp.
[5] A. I. Grigor'ev, S. O. Shiryaeva, V. A. Koromyslov, and D. F. Belonozhko, Zh. Tekh. Fiz. **67**(8), 27 (1997) [Tech. Phys. **42**, 884 (1997)].

Translated by R. M. Durham

Influence of Na^+, Ca^{2+}, and D_2O ions on the kinetics of heterophase density fluctuations in a lipid bilayer

D. B. Berg and D. P. Kharakoz

Institute of Industrial Ecology, Urals Branch of the Russian Academy of Sciences, Ekaterinburg Institute of Theoretical and Experimental Biophysics, Pushchino

(Submitted July 19, 1999)
Pis'ma Zh. Tekh. Fiz. **25**, 7–13 (November 26, 1999)

Experimentally measured temperature dependences of the velocity and absorption of ultrasound (7 MHz) were used to calculate the temperature dependences of the effective relaxation time τ_{eff} of the nucleation process near the phase-transition temperature T_t in phospholipid bilayers. It is observed that τ_{eff} is weakly sensitive to the ion composition of the medium and highly sensitive to the curvature of the bilayer and the replacement of H_2O by D_2O.
 [S1063-7850(99)01711-5]

Frenkel's theory states that near the phase-transition temperature subcritical new-phase nuclei consisting of heterophase density fluctuations, appear and decay spontaneously within the dominant phase.[1,2] In a bilayer of amphiphilic phospholipid molecules having smectic liquid-crystal ordering, ''crystallization–melting'' of hydrocarbon chains has been observed as a result of a temperature-induced phase transition.[3] Their conformational changes influence the compressibility of the heterogenous medium, which can be detected by an ultrasound technique.[4] In the liquid phase of a bilayer, heterophase density fluctuations in the form of two-dimensional solid-phase nuclei in the lamellar plane of the lipid bilayer have been observed near the phase transition temperature T_t (Ref. 5). The kinetics of the fluctuations are directly related to the probability of the formation of a critical nucleus and the kinetics of the transition to the solid state.[6] We know that the phase transition temperature is influenced by many factors, such as the ion composition of the aqueous phase.[3] No data are available on the influence of these factors on the kinetics of heterophase fluctuations.

In the present paper we investigate the influence of Na^+ and Ca^{2+} ions, how replacing H_2O with D_2O, and the curvature of the bilayer on the effective relaxation time of heterophase density fluctuations in bilayer vesicles of 1,2-dipalmitoyl-sn-glycero-3-phosphatidylcholine (DPPC). We used synthetic lyophilized DPPC supplied by Sigma (USA), better than 99% pure. Large multilamellar (multilayer) vesicles 500–1000 nm in diameter were prepared by dissolving the lipid in an organic solvent, followed by vacuum drying and dispersion in aqueous media[7] having various salt and isotopic compositions: H_2O (doubly distilled), D_2O (99.9% pure), solutions of analytical-grade NaCl (10 and 100 mM) and $CaCl_2$ (11.38 and 113.8 mM). This ensured that the composition of the aqueous medium was identical inside and outside each vesicle. The lipid concentration in the suspen-

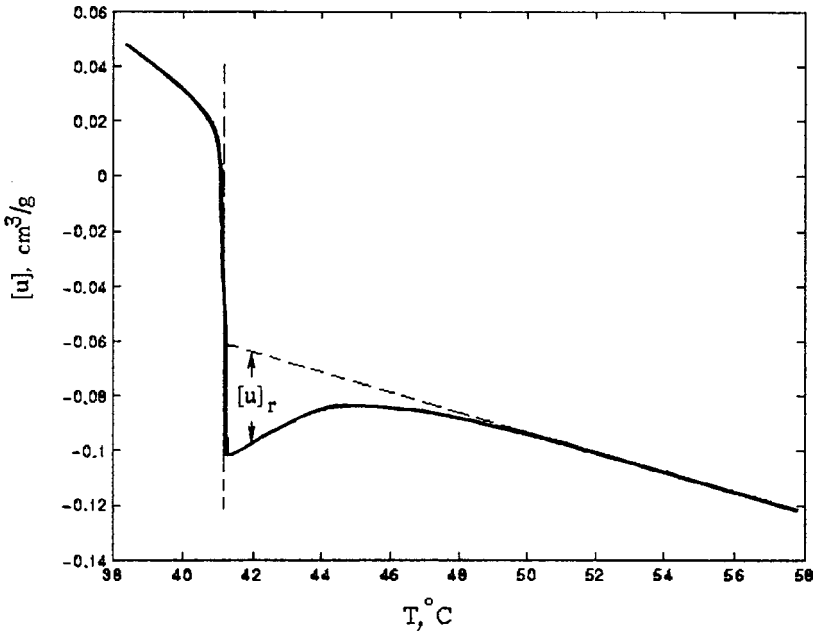

FIG. 1. Specific velocity of sound; the phase transition temperature (41.3°) is determined by linearly extrapolating the low- and high-temperature regions of the curve to the midpoint of the phase transition (vertical line).

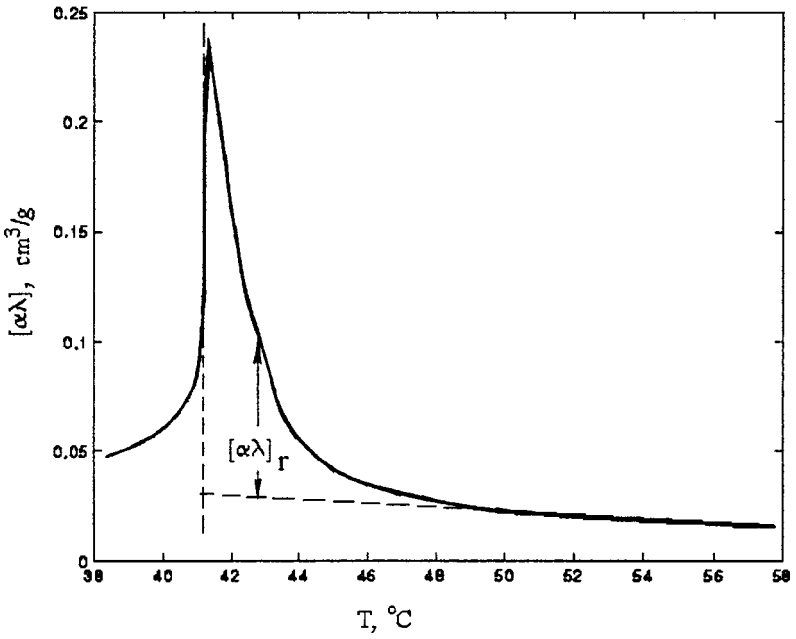

FIG. 2. Specific absorption.

sion was 1–5 mg/ml. Small, single-lamellar vesicles 15–50 nm in diameter were prepared from multilamellar vesicles by sonic treatment and centrifuging, using a technique described by Mendelsohn and Sunder.[8] Single-lamellar vesicles were converted into large vesicles by a ''freezing–thawing'' method[9] (five cycles).

Measurements of the velocity and absorption of ultrasound were made using a ultrasound differential fixed-path interferometer, consisting of two identical acoustic cavities.[10] The frequency range of the resonance peaks was 6.9–7.3 MHz. The velocity of sound can be measured with a relative error of 1×10^{-3} % and the absorption with a 1% error. Their temperature dependences were measured simultaneously for the same sample under heating (0.2 K/min). By comparing the acoustic characteristics of the lipid suspension and the aqueous medium without lipid, we determined the specific velocity of sound $[u]\equiv(u-u_0)/u_0c$ and the specific absorption of sound per wavelength $[\alpha\lambda]\equiv(\alpha\lambda-\alpha\lambda_0)/c$, where u and u_0 are the velocity of sound in the suspension and the aqueous medium, respectively, $\alpha\lambda$ and $\alpha\lambda_0$ are the absorption per wavelength in the suspension and the aqueous medium, and c is the lipid concentration. The value of $[u]$ consists of two components: an instantaneous component $[u]_\infty$ which is determined by the compressibility of the system in the absence of heterophase fluctuations and a relaxational component $[u]_r$, caused by the growth and decay of heterophase fluctuations: $[u]=[u]_\infty+[u]_r$.

The specific absorption $[\alpha\lambda]$ consists of the classical absorption $[\alpha\lambda]_{cl}$, caused by the shear viscosity of the medium and the relaxational absorption $[\alpha\lambda]_r$, caused by the

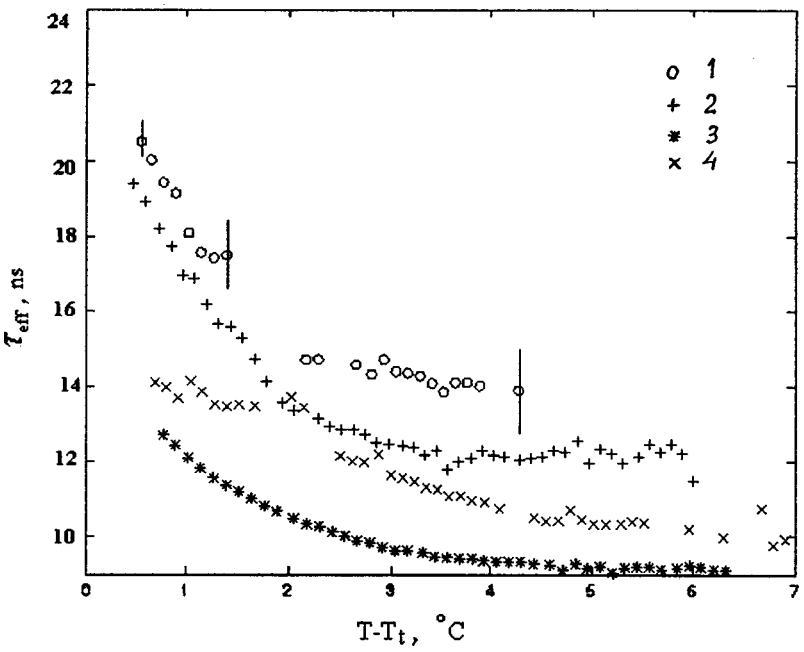

FIG. 3. Effective relaxation times; $T-T_t$ is the difference between the measurement temperature T and the phase transition temperature T_t; *1*—multilamellar vesicles in H_2O, *2*—multilamellar vesicles in H_2O and $CaCl_2$ (11.38 mM), *3*—multilamellar vesicles in D_2O, and *4*—single-lamellar vesicles in H_2O.

TABLE I. Phase transition temperatures and changes in the effective relaxation time of heterophase density fluctuations in vesicles of synthetic dipalmitoylphosphatidylcholine in aqueous media having different salt and isotopic compositions and different membrane curvature.

Composition of system	Value of T_t^*, °C	Shift of T_t^{**}, °C	Change in τ_{eff}^{***}
Multilamellar vesicle in H_2O	41.29	–	–
The same, in the presence of:			
NaCl, 10 mM	41.42	0.13	None
NaCl, 100 mM	41.49	0.20	None
$CaCl_2$, 11.38 mM	41.90	0.61	Decreases slightly
$CaCl_2$, 113.8 mM	42.90	1.61	None
Multilamellar vesicle in D_2O	41.70	0.41	Halved
Single-lamellar vesicle in H_2O	38.23	−3.06	Reduced 1.5 times
Multilamellar vesicle from single-lamellar ones	41.36	–	None

* –determined with an accuracy better than ±0.04 °C.
** –calculated as the difference between T_t in this system and T_t in large multilamellar vesicles in H_2O.
*** –relative to the value of τ_{eff} for large multilamellar vesicles in H_2O (Fig. 3).

dissipation of ultrasonic oscillation energy in the relaxation process: $[\alpha\lambda]=[\alpha\lambda]_{\text{cl}}+[\alpha\lambda]_r$. According to Mitaku *et al.*[11] the measured absorption for dilute lipid suspensions in the megahertz frequency range is only ascribed to the relaxational component: $[\alpha\lambda]\approx[\alpha\lambda]_r$. It contains contributions of all types of fluctuations including heterophase ones. The relaxation of the heterophase density fluctuations is a consequence of the variable pressure at ultrasound frequencies.

The figures give estimates of the kinetics of heterophase density fluctuations in a lipid liquid-crystal bilayer obtained by an ultrasound technique.[5]

Figures 1 and 2 give temperature dependences of the specific velocity and absorption of sound (subsequently referred to as ''velocity'' and ''absorption'' respectively) in suspensions of multilamellar vesicles of DPPC in pure water. In the phase transition region the profile of the velocity curve differs substantially from the simple sigmoidal curve which would be predicted from the ratio of the contributions of the two lipid states. This behavior can be attributed to the relaxation of heterophase density fluctuations which leads to additional compressibility near the transition.[5] The relaxation components of the velocity and absorption may be determined by linearly extrapolating the temperature dependences $[u]$ and $[\alpha\lambda]$ from the high-temperature range where the relaxational contribution is negligible. The relaxational components $[u]_r$ and $[\alpha\lambda]_r$ are then defined as the difference between the experimental curve and the extrapolated curve in Figs. 1 and 2 (for details see Refs. 5 and 12).

For a process with a single relaxation time the ratio of the quantities $[\alpha\lambda]_r$ and $[u]_r$ is related to the relaxation time τ by the following relation: $\tau=-[\alpha\lambda]_r/(2\pi\omega[u]_r)$, where ω is the angular frequency of the ultrasound.[13] Since the real process is described by the spectrum of relaxation times of the heterophase density fluctuations, this relationship gives an effective value τ_{eff}. This is an averaged characteristic of that part of the spectrum of relaxational processes which contribute to the velocity and absorption measured at frequency ω.

In an ionic medium (Fig. 3, Table I) the phase transition temperature T_t increases. The shift increases with increasing salt concentration, which is consistent with the published data.[3] Within measurement error NaCl does not influence τ_{eff}. In a medium containing 11.38 mM $CaCl_2$ we identified a negligible decrease in τ_{eff}, whereas at higher salt concentrations (113.8 mM) the values of τ_{eff} returned to their previous values. This probably indicates that the relaxation time of the heterophase density fluctuations depends nonlinearly on the $CaCl_2$ concentration. Similar nonlinear dependences are known for the density of phospholipid monolayers at the surface of water and the kinetics of formation of liquid-crystal textures in a planar capillary.[14]

Replacing H_2O with D_2O leads to a negligible increase in T_t in large multilamellar vesicles and τ_{eff} is approximately halved (Fig. 3). For small single-lamellar vesicles in H_2O the values of T_t and τ_{eff} are lower than those for large vesicles in H_2O.

After the small vesicles have merged to form large ones, T_t and τ_{eff} have the same values as for large vesicles in H_2O — the large curvature and stress of the bilayer in small vesicles influence both the value of T_t (Ref. 3 and τ_{eff} for the heterophase density fluctuations.

Thus, the kinetics of the heterophase fluctuations are weakly sensitive to changes in the ionic composition of the medium, but the curvature of the bilayer surface and replacing H_2O with D_2O has an appreciable influence on the kinetics.

[1] Ya. I. Frenkel', *Kinetic Theory of Liquids*, edited by N. N. Semenov and A. E. Glauberman (Clarendon Press, Oxford, 1946; Nauka, Moscow, 1975).
[2] A. R. Ubellonde, *Melting and Crystal Structure* (Clarendon Press, Oxford, 1965), 460 pp.
[3] G. Cevc and D. Marsh, *Phospholipid Bilayers. Physical Principles and Models* (Wiley, New York, 1987), 442 pp.
[4] S. Mitaku and T. Date, Biochem. Biophys. Acta **688**, 411 (1982).
[5] D. P. Kharakoz, A. Colotto, C. Lohner, and P. J. Laggner, J. Phys. Chem. **7**, 9844 (1993).
[6] D. P. Kharakoz, Biofizika **40**, 1354 (1995).
[7] V. M. Maynard and F. Dunn, Chem. Phys. Lipids **37**, 1 (1985).
[8] R. Mendelsohn and S. Sunder, Biochem. Biophys. Acta **419**, 563 (1976).
[9] L. D. Bergel'son, *Preparative Biochemistry of Lipids* [in Russian] (Nauka, Moscow 1981), 256 pp.

[10] A. P. Sarvazyan and D. P. Kharakoz, Prib. Tekh. Éksp. No. 3, 203 (1981).
[11] S. Mitaku, T. Jippo, and R. Kataoka, Biophys. J. **42**, 137 (1983).
[12] D. P. Kharakoz, G. V. Shil'nikov, and É. V. Pozharskiĭ, Biofizika **42**, 395 (1997).
[13] D. P. Kharakoz, J. Acoust. Soc. Am. **91**, 287 (1992).
[14] E. V. Popov and E. V. Kononenko, Poverkhnost' No. 5, 123 (1993).

Translated by R. M. Durham

Topological phase in a nonparaxial Gaussian beam

A. V. Volyar, T. A. Fadeeva, and V. G. Shvedov

Simferopol State University
(Submitted July 5, 1999)
Pis'ma Zh. Tekh. Fiz. **25**, 14–20 (November 26, 1999)

An analysis is made of the structure and evolution of the singularities of a nonparaxial Gaussian beam. It is shown that a Gaussian beam may be represented by a family of straight lines lying on the surface of a hyperboloid and that the wavefront of this beam is a function of a point source situated at a point on the z axis with the imaginary coordinate iz_0. The argument of this complex function is the topological phase of the beam which characterizes the rotation of the wavefront. The singularities of a nonparaxial Gaussian beam are located in the focal plane and are annular edge dislocations. Dislocation processes near the constriction of the Gaussian beam only occur as a result of aperture diffraction. © *1999 American Institute of Physics.* [S1063-7850(99)01811-X]

A generally recognized description of laser beams widely used in the literature in the design of laser cavities, the excitation of optical fibers, and in other fields of laser physics is based on the so-called paraxial approximation in the solution of the wave equation.

This arises because the wave equation

$$(\nabla^2 + k^2)\Psi = 0 \tag{1}$$

(k is the wave number) is symmetric along all three spatial coordinates (it is implied that the wave process is steady-state).

Quite clearly, the wave function satisfying this equation should also satisfy these symmetry properties. Hence, if the wave function depends on three coordinates, it is difficult to isolate the one along which the light propagates and at the same time to satisfy the wave equation (1). In order to resolve this situation, it is necessary to use an approximate wave description of the laser beam, assuming that its divergence is low (the radius of the beam constriction is much larger than the wavelength). This means that the second derivative with respect to the selected coordinate can be neglected in the wave equation, thereby destroying the symmetry in the operator of the wave equation. Although this approach offers extensive possibilities for solving many practical problems in laser and fiber optics, it cannot give a correct description of the field transformations in the beam constriction region.

Various mathematical methods of overcoming this difficulty with varying degrees of accuracy have now ben developed (see, for example, Refs. 1–4).

In particular, Berry[5] used an asymptotic estimate of the Fourier integral (an expansion of the field of a Gaussian beam as a series in terms of plane waves in all possible directions) to show that Airy dislocation rings appear near the constriction and that these may be created and annihilated by minuscule perturbations of the beam constriction profile. These processes involving the creation and annihilation of singularities at the wavefront were described by Berry as dislocation reactions.[5]

The aim of the present paper is to study the structure of a nonparaxial Gaussian beam and the dislocation reactions near its constriction by means of a strict analytic solution of the wave equation.

In order to describe a spatially bounded laser beam, it is convenient to represent this as a nonuniform spherical wave, similar to the procedure used for plane waves having a nonuniform amplitude distribution.[6] We can assume for instance, that a point source and a spherical wave sink are located at a point having the imaginary coordinate $z = iz_0$ (Ref. 7).

The distance between the source and some point lying on the surface of the wavefront then becomes a function of a complex variable:

$$R = \sqrt{r^2 + (z - iz_0)^2} = \sqrt{r^2 + z^2 - z_0^2 + 2izz_0}, \tag{2}$$

where $r^2 = x^2 + y^2$ and z_0 is the wave parameter of the beam.

A particular solution of the wave equation (1) may be represented in the form:[8]

$$\Psi(R) = J_{n+1/2}(kR) P_n^l(\cos\Theta) \left\{ \begin{matrix} \cos l\varphi \\ \sin l\varphi \end{matrix} \right\}, \tag{3}$$

where $J_{n+1/2}(x)$ is a spherical Bessel function of the first kind, P_n^l is a Jacobi polynomial, φ is the azimuthal angle, and Θ is a complex angle.

We shall now analyze the structure of a lowest-order nonparaxial Gaussian beam with $l = 0$. We write the solution (3) in the form:

$$\Psi(R) = A_0 \frac{\sin kR}{kR}. \tag{4}$$

In Ref. 9 Volyar *et al.* showed that a paraxial Gaussian beam can be represented as nested hyperboloids of revolution:

$$\frac{x^2 + y^2}{\rho^2} = \frac{(z + iz_0)(z - iz_0)}{z_0^2}. \tag{5}$$

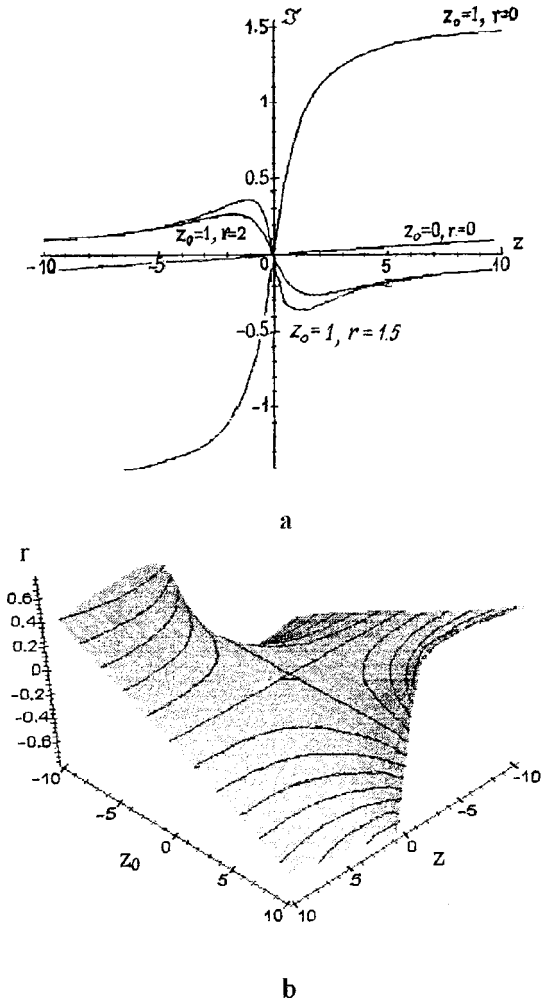

FIG. 1. Topological phase $\mathcal{J}$ of a Gaussian beam as a function of the longitudinal coordinate z for various values of the radial coordinate r and the constriction parameter z_0 (a). Surface of the topological phase $\mathcal{J}(r,z,z_0)=0$ in the spatial coordinates r,z,z_0 (b). All the coordinates are given in units of $1/k$, $k=2\pi/\lambda$ ($\lambda=0.63\ \mu$m).

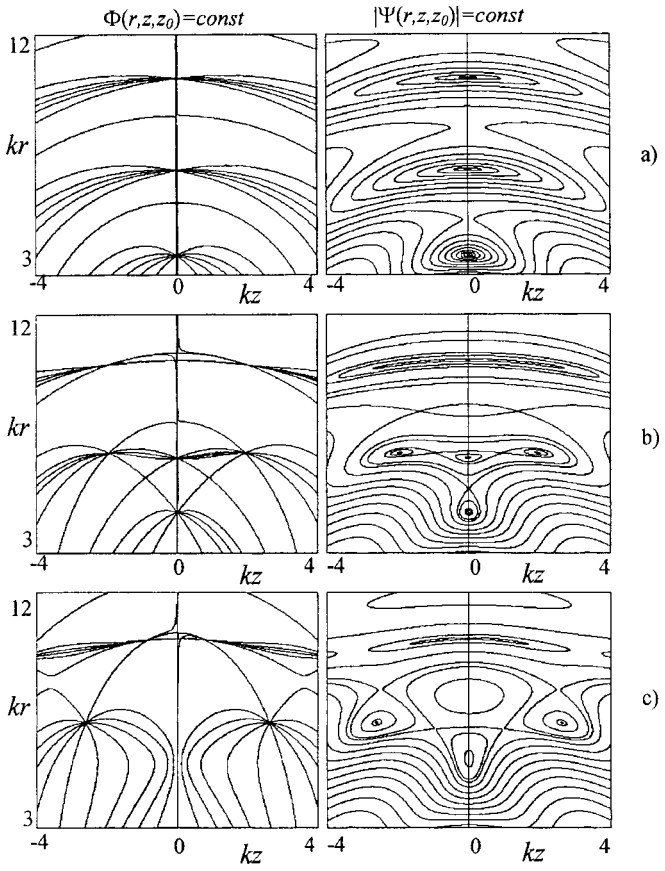

FIG. 2. Dislocation reactions in a nonparaxial Gaussian beam near the constriction for various values of the parameter z_0: a — $kz_0=3$, b — $kz_0=5.884$, and c — $kz_0=8.5$.

On the surface of each hyperboloid, the current vector (Poynting vector) forms two families of straight lines along which the energy propagates, and these are equivalent to the geometric rays described by:

$$\varphi=-\sigma\arctan\frac{z}{z_0}. \tag{6}$$

We then find that during the propagation process each point lying on the wavefront surface is turned through the angle (6) in the plane $z=$const.

The distance along the current line from the constriction plane to a certain point on the wavefront having the coordinates (r,z) is then given by

$$\mathcal{R}^2=x^2+y^2+z^2-\rho^2, \tag{7}$$

where ρ is the radius of the constriction of the hyperboloid of revolution (5) in the constriction plane $z=0$ $(0<\rho<\infty)$.

If we take a constant ray length for $\rho=z_0$, it can be seen from a comparison of Eqs. (2) and (7) that the distance along the ray to the selected point is equal to the real part of the radicand for the complex radius $R=\sqrt{\mathcal{R}^2+iz_0z}$. For constant ray length $\mathcal{R}$, the equation for the wavefront surface has the form:

$$k\mathcal{R}=kz\sqrt{\frac{r^2+z^2+z_0^2}{r^2+z_0^2}}. \tag{8}$$

In particular, provided that $kz_0\gg1$ we obtain from Eq. (8)

$$k\mathcal{R}\approx kz+\frac{kr^2z}{2(z^2+z_0^2)}=kz+\frac{kr^2}{2R(z)}. \tag{9}$$

This expression is exactly the same as the expression for the dynamic phase of a paraxial Gaussian beam.[1] The imaginary part of the complex length (2) is evidently related to the rotation of the beam wavefront. According to Berry,[10] any cyclic change in the parameters of the wave function (for instance, rotation of the wavefront or a change in its shape) induces a topological phase which, in this case, is characterized by the argument of the complex length.

In formal terms, the topological phase of a Gaussian beam is k times smaller than the dynamic phase and is the argument of the complex radius in the denominator of expression (4) $\mathcal{J}=\arg R$:

$$\mathcal{J}=\frac{1}{2}\arctan\frac{z}{r+z_0}-\frac{1}{2}\arctan\frac{z}{r-z_0}. \tag{10}$$

For large Rayleigh lengths ($kz_0 \gg 1$) we find from Eq. (10) that $\mathcal{J} \approx \arctan\frac{z}{z_0}$, i.e., it is the same as the anomalous Gouy phase, as we predicted. A decrease in the parameter z_0 complicates the behavior of the topological phase $\mathcal{J}$ near the focal plane because, in addition to rotation of the wavefront, its buildup process also includes other dynamic processes such a change in the wavefront curvature. For very small values of the parameter z_0, the concept of a wavefront near the focal plane generally becomes physically meaningless since the wave surface becomes unconnected. In this case, the value of $\mathcal{J}$ clearly plays the role of the coefficient of connectedness. Figure 1 shows curves describing the behavior of the topological phase near the beam constriction.

We shall analyze the structure of the phase singularities of a nonparaxial beam near the plane $z=0$. We construct lines of equal phase $\Phi(x,y,z,z_0)=\text{const}$ and equal amplitude $|\Psi|=\text{const}$. These families of curves are plotted in Fig. 2a using the coordinates (r,z). It can be seen that near the constriction of an unbounded nonparaxial Gaussian beam, families of concentric annular dislocations form at the points of intersection of the phase contours. Note that these rings are located at distances $r>z_0$ from the z axis. We did not observe that any slight change in the beam parameter z_0 could cause the creation or annihilation of rings (dislocation reactions), as was postulated in Ref. 5. We merely observed a synchronous change in the position of the dislocation rings accompanying any changes in the radius of the beam constriction. Nevertheless, dislocation reactions begin to take place in the nonparaxial Gaussian beam when the field of this beam is linearly combined with the field of a spherical wave emitted by a point source positioned at the origin $x=y=z=0$.

The result of this addition is manifest in dislocation chain reactions, the creation and annihilation of phase singularities as described by Nye,[11] so that the sum topological index of all the phase singularities and saddles, and also the total topological charge is conserved during the dislocation reactions.

Thus, if the radius of the beam constriction varies very slightly by fractions of a wavelength for certain values of z_0, the wavefront saddle may move with the phase singularity (Fig. 2). At this moment two phase singularities of the same sign and two saddles are created. A further increase in the constriction radius leads to annihilation of the pair of saddles and the pair of singularities, as shown in Figs. 2b and 2c. Attention should be drawn to the subwave scale on which these dislocation reactions take place.

To conclude, the dislocation reactions in a nonparaxial Gaussian beam should be ascribed not to the beam itself but to the diffraction of light observed when this beam propagates through a nontransparent screen with an aperture.

[1] L. W. Davis, Phys. Rev. A **19**, 1177 (1979).
[2] M. Lax, W. Louisell, and B. McKnight, Phys. Rev. A **11**, 1365 (1975).
[3] G. P. Agrawal and D. N. Pattanayak, J. Opt. Soc. Am. **69**, 575 (1979).
[4] C. J. R. Sheppard and S. Saghati, Phys. Rev. A **57**, 2971 (1998).
[5] M. V. Berry, J. Mod. Opt. **45**, 1845 (1998).
[6] M. Born and E. Wolf, *Principles of Optics* (Pergamon Press, Oxford, 1968).
[7] L. B. Felson, J. Opt. Soc. Am. **66**, 751 (1976).
[8] G. N. Watson, *A Treatise on the Theory of Bessel Functions*, 2nd ed. (Cambridge University Press, London, 1945).
[9] A. V. Volyar, V. G. Shvedov, and T. A. Fadeeva, Pis'ma Zh. Tekh. Fiz. **25**(5), 87 (1999) [Tech. Phys. Lett. **25**, 203 (1999)].
[10] M. V. Berry, Proc. R. Soc. London A No. 392, 45 (1984).
[11] J. E. Nye, J. Opt. Soc. Am. A **15**, 1132 (1998).

Translated by R. M. Durham

Infinite anisotropy of the piezoeffect in $PbTiO_3$-based ferroceramic

E. A. Dul'kin, L. I. Grebenkina, D. I. Makar'ev, A. N. Klevtsov, and V. G. Gavrilyachenko

Research Institute of Mechanics and Applied Mathematics, Rostov State University
(Submitted June 7, 1999)
Pis'ma Zh. Tekh. Fiz. **25**, 21–25 (November 26, 1999)

Acoustic emission, dilatometry, and optical microscopy were used to study the polarization of PKR-70 $PbTiO_3$ ferroceramic samples. It was established that in an electric field higher than 2.5 kV/mm the piezoeffect in the samples acquires an infinite anisotropy, accompanied by acoustic-emission and dilatometric anomalies. It is shown that this anisotropy of the piezoeffect is caused by microcracking of the samples in the direction of the polarizing field.
 [S1063-7850(99)01911-4]

Anisotropy of the piezoeffect in ferroceramics is a topical problem because of its scientific importance and obvious technical applications. Theoretical analyses have shown[1–3] that this anisotropy is mainly attributable to the weak anisotropy of the crystal permittivity which is established in $PbTiO_3$-based ferroceramics.[4]

At the Research Institute of Physics at Rostov State University, efficient $PbTiO_3$-based piezomaterials, PKR-67 and PKR-70, have been fabricated in which the ratio of the piezomoduli d_{33}/d_{31} reached values between five and infinity (Refs. 5 and 6). This result was obtained under extreme polarization regimes, in a polarizing field of 4–6 kV/mm at 160° C for at least 30 min, after which the mechanical Q-factor of the radial vibrations of the samples dropped sharply. Studies of the microstructure of the polarized samples revealed substantial rearrangement of the crystallite domain structure as a result of which the 90° domain walls were oriented perpendicular to the direction of the polarizing field E_p. A similar effect was observed by Rastoropov *et al.*[7] in $PbTiO_3$ ceramic with added Ca. In Ref. 5 Grineva *et al.* established a correlation between the abrupt increase in the anisotropy of the piezomodulus d_{33}/d_{31} and a reduction in the mechanical strength of the samples. Etched cleaved sections of these samples revealed microcracks along grain boundaries and in the bulk of the grains, where in this last case the cracks were oriented in the direction of E_p. It was postulated that these microcracks form as a result of 90° reorientations as E_p increases and for $E_p > 8$ kV/mm the ceramic spontaneously broke up.

It follows from all the reasoning put forward above that, in addition to its piezoproperties acquiring infinite anisotropy, $PbTiO_3$ ceramic undergoes cracking during the polarization process which may result in premature fracture of components. The correlation between the observed anisotropy of the piezoproperties and microcracking of the samples has yet to be clarified.

We know that microcracking can be effectively studied using an acoustic emission method. Acoustic emission has already been used to study crack nucleation and growth in $PbTiO_3$ crystals.[8] The deformability of a piezoceramic caused by rearrangement of its domain structure means that dilatometry can be used to study the polarization process of samples.

The aim of the present study is to use acoustic-emission and dilatometric techniques to examine samples of $PbTiO_3$ ceramic during polarization which leads to infinite anisotropy of the piezoeffect.

We investigated samples of PKR-70 piezoceramic in the form of disks 10 mm in diameter and 1 mm thick using a complex method.[9] We measured the acoustic-emission activity $\dot{N}$ and the relative dilatation $\Delta L/L$ when samples placed in an oil-filled cell at $T = 120$° C were exposed to a static electric field increasing at an average rate of 100 V/min.

The results of the measurements are plotted in Fig. 1. It can be seen that as the intensity E_p increases, the samples undergo slight compression and at $E_p = 2.5$ kV/mm we observe a dilatation minimum accompanied by an abrupt surge of acoustic emission activity $\dot{N}$. As E_p increases further, the samples also expand slightly and at $E_p > 3.5$ kV/mm electrical breakdown occurs.

Control samples were polarized as follows: after acoustic-emission signals were detected, we stopped increasing the field E_p, the level reached was held for 30 min, and

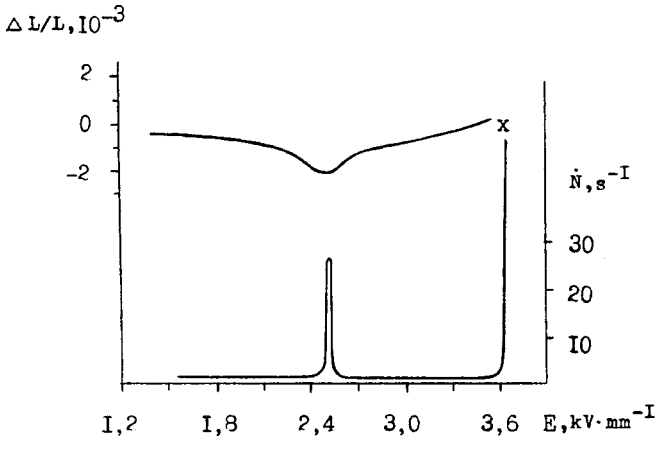

FIG. 1. Acoustic emission activity $\dot{N}$ and relative dilatation $\Delta L/L$ of PKR-70 ferroceramic samples as a function of the polarizing field E_p.

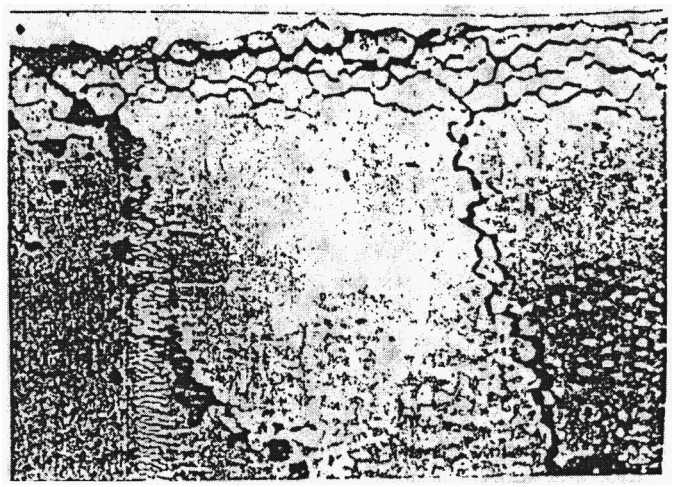

FIG. 2. Photomicrograph of a surface layer PKR-70 ferroceramic illustrating the growth of major cracks in the direction of the polarizing field E_p.

the samples were then cooled to room temperature under the field. Measurements of the electrophysical parameters of the control samples thus polarized showed infinitely anisotropic piezoproperties. It should be noted that this anisotropy is retained after these samples were heated above the Curie temperature and then polarized in fields not exceeding 2.5 kV/mm.

Figure 2 shows a photomicrograph of a cleaved fragment of one of the control samples. In a narrow surface layer we observe mass cracking along grain boundaries, causing grains to be displaced and thus leading to disintegration of the layer. In addition, this mass disintegration in the surface layer promotes the growth of major cracks which penetrate into the samples along grain boundaries in the direction of E_p.

Thus, on the basis of known data and these results, we can describe the polarization process in $PbTiO_3$ ferroceramic samples as follows. After a specific value of E_p has been reached, intensive twinning is initiated inside grains, which is responsible for the dilatation minimum. As a result of the ensuing change in the geometric dimensions of the grains, cracks appear between them, leading to disintegration of the ceramic. This mass cracking generates major cracks which penetrate inside the samples in the direction of E_p and produce acoustic emission. Samples containing cracks have a low mechanical Q factor, low strength, and infinitely anisotropic piezoproperties. It can therefore be confirmed that the infinite anisotropy of the piezoproperties of $PbTiO_3$ ferroceramic, and in particular PKR-70, is caused by cracks in the bulk of the material which are induced by polarization in strong fields.

To conclude, we note that these results indicate that acoustic emission can be effectively used as a method of nondestructive quality control during the polarization of piezoceramics.

[1] A. V. Turik, V. Yu. Topolov, A. I. Chernobabov, and E. I. Bondarenko, Izv. Ross. Akad. Nauk, Ser. Fiz. **57**(6), 82 (1993).
[2] V. Yu. Topolov, A. V. Turik, and A. I. Chernobabov, Kristallografiya **39**, 884 (1994) [Crystallogr. Rep. **39**, 805 (1994)].
[3] A. V. Turik, V. Yu. Topolov, and A. I. Chernobabov, Ferroelectrics **190**, 137 (1997).
[4] A. V. Turik, E. G. Fesenko, V. G. Gavrilyachenko, and G. I. Khasabova, Kristallografiya **19**, 1095 (1974) [Sov. Phys. Crystallogr. **19**, 677 (1974)].
[5] L. D. Grineva, V. P. Zatsarinnyĭ, V. A. Aleshin, V. A. Servuli, L. V. Shilkina, and E. S. Miroshnichenko, Problemy Prochnosti **4**, 34 (1993).
[6] L. D. Grineva, V. A. Aleshin, and O. N. Razumovskaya, Izv. Akad. Nauk SSSR, Ser. Fiz. **54**, 772 (1990).
[7] S. B. Rastoropov, V. Z. Borodin, V. E. Yurkevich, E. J. Eknadiosiants, A. E. Panich, A. N. Pinskaya, and A. V. Prikhod'kov, Ferroelectrics **160**, 107 (1994).
[8] E. A. Dul'kin, Kristallografiya **39**, 738 (1994) [Crystallogr. Rep. **39**, 669 (1994)].
[9] E. A. Dul'kin, Sverkhprovodimost: Fiz., Khim., Tekh. **5**(1), 103 (1992).

Translated by R. M. Durham

Frequency doubling of 859.2 nm radiation in a waveguide formed from Nb_2O_5 and Ta_2O_5 films on a $KTiOPO_4$ substrate

P. M. Zhitkov, A. Yu. Agapov, and V. M. Shevtsov

Russian Peoples' Friendship University, Moscow
(Submitted July 12, 1999)
Pis'ma Zh. Tekh. Fiz. **25**, 26–34 (November 26, 1999)

It is proposed that second harmonic generation in a waveguide formed from Nb_2O_5 and Ta_2O_5 films on a $KTiOPO_4$ crystal substrate can be used to obtain blue coherent radiation. It is shown that the second harmonic generation efficiency in a thin-film stripe waveguide may reach $1010\%\,W^{-1}\cdot cm^{-2}$, and the spectral phase-matching width may reach $0.45\,nm\cdot cm$. Generation of the second harmonic of 859.2 nm laser radiation was observed experimentally in a Ta_2O_5–Nb_2O_5–$KTiOPO_4$ waveguide.
[S1063-7850(99)02011-X]

Intensive studies are now being carried out to increase the density of information recording on optical-carrier media by using short-wavelength light sources for recording and readout. A miniature, reliable, fairly high-power source in the 400–500 nm range can be produced by doubling the frequency of semiconductor laser radiation.

The highest frequency conversion efficiency for semiconductor laser radiation can be achieved by using nonlinear waveguide devices. The small transverse dimensions of the field localization region and the diffraction-free propagation of waves in waveguides ensure that these systems have conversion efficiencies up to 10^4 times higher than those of conventional bulk systems.[1]

In order to reduce the transverse dimensions of the nonlinear interaction zone, the cross section of the waveguide structure must have the largest possible refractive index gradient. At constant pump source power this can maximize the intensities and thereby substantially enhance the nonlinear conversion efficiency.

Most studies of second harmonic generation (SHG) in optical waveguides have been made using graded-index structures on nonlinear crystal substrates. However, because of the characteristic features of the methods of fabricating these waveguides, the refractive index gradient between the surface carrier layer and the substrate generally does not exceed 0.1 whereas in thin-film waveguides this gradient may be greater than 0.5. Hence, thin-film optical waveguides on nonlinear crystal substrates appear to be the most promising frequency conversion devices.

In the present study we consider a waveguide structure formed by Nb_2O_5 and Ta_2O_5 films on a $KTiOPO_4$ (KTP) crystal substrate possessing high optical nonlinearity (Fig. 1). The film and substrate materials possess high optical strength, they are transparent in the wavelength ranges of the pump and second harmonic, and their refractive indices differ substantially.

Unlike a bulk SHG system, an optical waveguide can ensure that the phase velocities of the pump and second harmonic waves are equal when they are similarly polarized. In this case, it becomes possible to use the largest component of the nonlinear susceptibility tensor of the substrate material $d_{33}=18.5\,pm/V$ (Ref. 2). When selecting the TE polarization of the pump and second harmonic waves, the *c* crystallographic axis should be oriented in the plane of the substrate perpendicular to the direction of propagation of the interacting waves (Fig. 1).

Of the greatest practical interest is the phase matching of the lowest waveguide modes in this structure: the pump wave TE_0^{ω} and the harmonic $TE_1^{2\omega}$. The point of intersection of the dispersion curves of these modes at which their effective refractive indices are equal $n_{\rm eff}^{\omega}=n_{\rm eff}^{2\omega}$ is situated close to the cutoff of the second harmonic wave. Hence, the fractions of the power transferred by these modes in the nonlinear substrate, the overlap integral of their fields, and consequently the SHG efficiency are maximized.

Figure 2 shows the region of intersection of the dispersion curves of the TE_0^{ω} and $TE_1^{2\omega}$ waveguide modes in detail. An interesting feature of this structure is that for a Ta_2O_5 film of constant thickness the thickness of the Nb_2O_5 film can have two values for which phase matching is achieved (Fig. 2a). It is possible to select the thickness of the Ta_2O_5 film so that the dispersion curves of the interacting modes will touch at one point (Fig. 2b). In this case, the constraints on the accuracy of fabricating an Nb_2O_5 film of a particular thickness are reduced substantially.

In the course of the calculations it became clear that when the lasing wavelengths and refractive indices of the media forming the waveguide are constant, there is a range of film thicknesses in which the phase-matching condition can be satisfied for the TE_0^{ω} and $TE_1^{2\omega}$ modes. The coordinates of each point on the solid curve plotted in Fig. 3 correspond to the film thicknesses for which $n_{\rm eff}^{\omega}=n_{\rm eff}^{2\omega}$. This region is bounded. The thickness of the Nb_2O_5 film cannot exceed that corresponding to phase matching in a waveguide structure with a Ta_2O_5 film of infinite thickness. However, for Nb_2O_5 films of small thickness, no $TE_1^{2\omega}$ waveguide mode exists and the second harmonic wave can exist in the substrate in the form of Čerenkov radiation. The boundary of

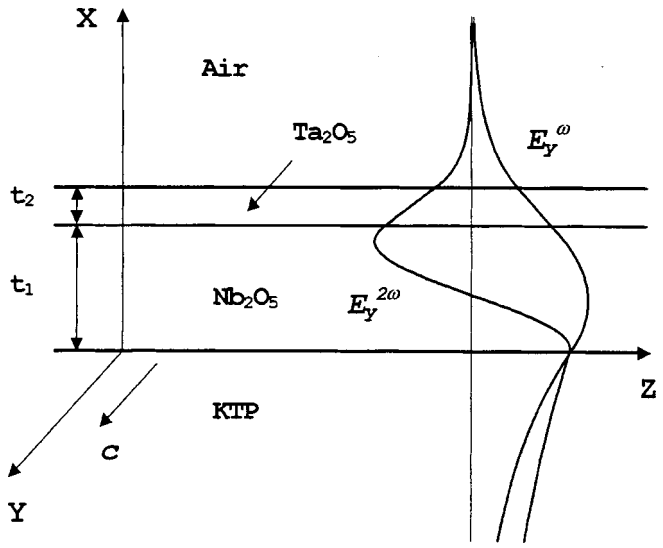

FIG. 1. Waveguide formed by Ta_2O_5 and Nb_2O_5 films on a KTP crystal substrate. The distributions of the fields of the TE_0^{ω} and $TE_1^{2\omega}$ modes in the cross section of the waveguide structure are shown on the right.

the Čerenkov radiation region is the dashed line (Fig. 3) on which the cutoff condition for the $TE_1^{2\omega}$ mode: $n_{\text{eff}}^{2\omega}=n_{\text{KTP}}^{2\omega}$ is satisfied at each point.

For each point on the solid curve plotted in Fig. 3 we calculated the normalized SHG efficiency η in a 3 μm wide Ta_2O_5–Nb_2O_5–KTP stripe frequency-doubler. The dependence of this efficiency on the thickness of the Nb_2O_5 film is plotted in Fig. 4. It can be seen that the curve of the normalized SHG efficiency has a maximum at which the overlap integral of the fields of the TE_0^{ω} and $TE_1^{2\omega}$ modes in the nonlinear substrate reaches the highest value. The main reason for the abrupt change in this integral is that the field distribution of the $TE_1^{2\omega}$ mode near the cutoff depends strongly on the thickness of the Nb_2O_5 film.

The maximum calculated value of the normalized efficiency of conversion to the second harmonic is 1010% $W^{-1}\cdot cm^{-2}$. For a pump wave power of 100 mW in the waveguide and an interaction length of 3 nm, the second-harmonic wave power is 9 mW. A comparison between this result and the published data[2,3] reveals that in terms of normalized conversion efficiency this system is superior to all known designs of KTP crystal frequency doublers.

An important characteristic of an optical frequency doubler is $\Delta\lambda$, the spectral phase-matching width normalized per unit nonlinear interaction length.[4] In order to calculate $\Delta\lambda$ we used values of the refractive indices of the film materials measured at several wavelengths and an interpolation technique described in Ref. 5. At the maximum of the normalized SHG efficiency the calculations give $\Delta\lambda=0.06\,\text{nm}\cdot\text{cm}$. As we move to the left on the solid curve in Fig. 3, the value of $\Delta\lambda$ increases monotonically and at the point corresponding to cutoff of the $TE_1^{2\omega}$ mode, it reaches a maximum of $0.45\,\text{nm}\cdot\text{cm}$ (Fig. 4). This behavior of $\Delta\lambda$ as the thickness of the Nb_2O_5 film decreases is caused by an increase in the fraction of the power transferred by the $TE_1^{2\omega}$ mode in the substrate, as a result of which the dispersion of $n_{\text{eff}}^{2\omega}$ falls rapidly and approaches n_{eff}^{ω}.

The possibility of substantially increasing $\Delta\lambda$ in the proposed structure becomes important in practice when these are used as pump sources for pulsed semiconductor lasers. For example, for a nonlinear interaction length of 3 mm the spectral phase-matching width reaches 1.5 nm, which means that the frequency of pump radiation having pulse durations up to 1 ps can be efficiently doubled. An increased spectral phase-matching width is also highly desirable for the development of waveguide nonlinear tunable optical parametric oscillators in the communications range of 1300–1600 nm.

The nonlinear waveguide film structures were fabricated by rf cathode sputtering. In this method the films are deposited at a relatively low rate so that their thicknesses can be

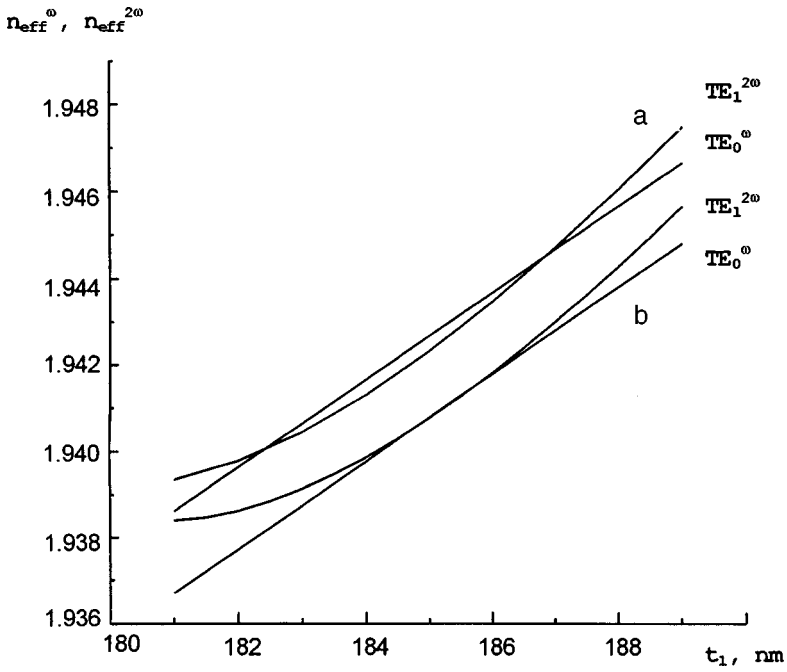

FIG. 2. Phase matching of the TE_0^{ω} and $TE_1^{2\omega}$ modes for Ta_2O_5 films of different thickness: a — $t_2=56$ nm and b — $t_2=52$ nm.

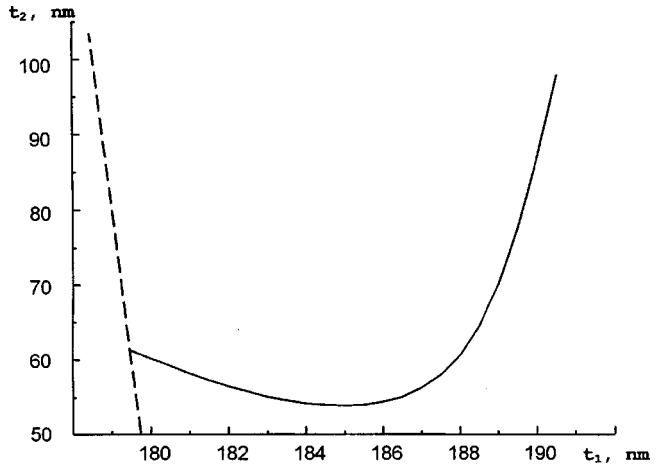

FIG. 3. Diagram of SHG regimes. The phase-matching condition for the TE_0^{ω} and $TE_1^{2\omega}$ waveguide modes is satisfied at the points on the solid curve.

monitored over the deposition time with a high degree of accuracy. In order to obtain a high SHG efficiency, during fabrication of the waveguide structure the error for the film thicknesses should not exceed a few angstrom, while the error for the refractive indices be within the fourth place of decimals. Our method of measuring the effective refractive indices using a prism coupling element[6] can measure the optical parameters of the waveguide films with the required degree of accuracy.

In order to determine the refractive indices of the Nb_2O_5 and Ta_2O_5 films, we prepared series of calibration samples. The films were deposited on a KTP substrate by sputtering metal targets in an oxygen–argon mixture. The parameters of the rf plasma discharge were varied from one sample to another. The films obtained were of high optical quality and had different rates of deposition and refractive indices. As a result, we selected a technological deposition regime for the Nb_2O_5 films which ensures the highest refractive indices at the working wavelengths. These values were $n_1^{\omega}=2.1880$ at the pump wavelength $\lambda^{\omega}=859.2$ nm and $n_1^{2\omega}=2.3712$ at the second-harmonic wavelength. In order to fabricate the Ta_2O_5 film we selected a regime which gives the refractive indices $n_2^{\omega}=1.8791$ and $n_2^{2\omega}=1.9629$.

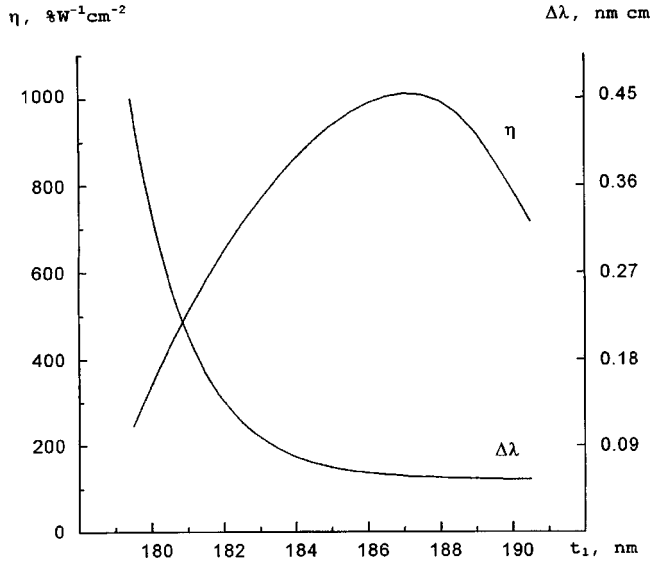

FIG. 4. Normalized characteristics of a stripe frequency doubler as a function of the Nb_2O_5 film thickness.

We used these experimental values of the refractive indices to calculate the film thicknesses for which the phase-matching condition is satisfied for the TE_0^{ω} and $TE_1^{2\omega}$ waveguide modes. Knowing the rates of deposition of the films, we calculated their deposition times and fabricated samples for the SHG experiments. The samples had Nb_2O_5 films of different thickness, while the thickness of the Ta_2O_5 film was kept constant at 55 nm.

Waveguide second harmonic generation was observed experimentally in a sample having an Nb_2O_5 film 183 nm thick. The pump source was a titanium–sapphire laser, tunable in the 850–860 nm range. Second harmonic generation was observed when the laser was operated in the cw and pulsed modes. The 859.2 nm pump radiation was focused by a lens of 10 cm focal length and was coupled into the waveguide using a prism. The pump and second-harmonic radiation was coupled out of the waveguide using a second prism coupler. The values of n_{eff}^{ω} and $n_{\text{eff}}^{2\omega}$ were measured near the coupling-out prism in the cw mode and were found to be 1.9408.

The powers transferred by the pump and second-harmonic waves were measured in the pulsed mode. The pulse duration was 0.1 ps and the repetition frequency 100 MHz. For a nonlinear interaction zone 300 μm wide, an interaction length of 3 mm, and an average pump wave power of 3 mW in the waveguide the average power of the second-harmonic wave was 15 μW.

For samples having thinner Nb_2O_5 films, SHG was always observed in the form of Čerenkov radiation within the laser tuning range. Measurements of the effective refractive index of the pump wave at $\lambda^{\omega}=859.2$ nm showed that the value of $n_{\text{eff}}^{\omega}=1.9107$ is lower than the refractive index of the substrate $n_{\text{KTP}}^{2\omega}=1.9384$.

To sum up, we suggest using SHG in a waveguide formed by Nb_2O_5 and Ta_2O_5 films on a KTP crystal substrate to double the frequency of semiconductor laser radiation. We have selected film thicknesses for which the overlap integral of the fields of the TE_0^{ω} and $TE_1^{2\omega}$ modes has a maximum. We have shown that by using a stripe waveguide design based on highly refracting Nb_2O_5 and Ta_2O_5 films, it is possible to achieve extremely high power densities in a nonlinear interaction zone having a cross-sectional area of 0.3×3 μm and obtain the highest normalized conversion efficiency reported so far for KTP structures, $1010\%\,\text{W}^{-1}\cdot\text{cm}^{-2}$.

We have also shown that the dispersion of the effective refractive indices of the different-frequency modes can be effectively controlled by selecting the film thicknesses in a Ta_2O_5–Nb_2O_5–KTP waveguide structure. We have demonstrated that the normalized spectral phase-matching width can be increased from 0.05 to 0.45 nm·cm.

Second harmonic generation of 859.2 nm laser radiation has been observed experimentally in a Ta_2O_5–Nb_2O_5–KTP waveguide.

The authors are grateful to S. A. Krikunov and S. A. Magnitskiĭ for supplying the crystal substrates and helping with the measurements using a titanium–sapphire laser.

[1] *Nonlinear Optical Properties of Organic Molecules and Crystals*, Vol. 1, edited by D. S. Chemla and J. Zyss (Academic Press, New York, 1987), 355 pp.
[2] T. Doumuki, H. Tamada, and M. Saitoh, Appl. Phys. Lett. **65**, 2519 (1994).
[3] D. Eger, M. Oron, and M. Katz, Appl. Phys. Lett. **64**, 3208 (1994).
[4] G. G. Gurzadyan, V. G. Dmitriev, and D. N. Nikogosyan, *Handbook of Nonlinear Optical Crystals* (Radio i Svyaz', Moscow, 1991), 159 pp.
[5] S. Ingrey, W. Westwood, and Y. Cheng, Appl. Opt. **14**, 2194 (1975).
[6] P. Herrman, Appl. Opt. **19**, 3261 (1980).

Translated by R. M. Durham

Mixed kinetic–hydrodynamic level of description for dispersed liquids

V. Ya. Rudyak

Novosibirsk State Architectural and Civil Engineering Institute
(Submitted July 19, 1999)
Pis'ma Zh. Tekh. Fiz. **25**, 35–38 (November 26, 1999)

It is shown that dispersed liquids (gaseous or liquid suspensions) can only be described at the hydrodynamic level over a limited range of flow parameters. A mixed kinetic–hydrodynamic model is proposed to describe flows of dispersed liquids. © *1999 American Institute of Physics.* [S1063-7850(99)02111-4]

The evolution of dispersed liquids, gaseous suspensions, or liquid suspensions is generally described using hydrodynamic equations (see, for example, Refs. 1 and 2). However, dispersed liquids can only be described at the hydrodynamic level if the corresponding characteristic temporal τ_L and spatial L flow scales differ substantially from the maximum kinetic scales. The hydrodynamic level of description will be single-fluid (single-velocity and single-temperature) if the dispersed liquid is fairly homogeneous. A characteristic indicator of the single-velocity flow regime of a gas mixture, liquids, or dispersed liquids is that the entire system is described by a single set of mass-averaged macroscopic characteristics. This is possible if some hydrodynamic, physically infinitely small, scale r_h can be isolated in the system so that

$$r_h \gg l_i \gg r_{0i}, \quad i=1,2,\ldots, \tag{1}$$

where r_{0i} are the characteristic particle sizes in the dispersed liquid (molecules and particles) and l_i is the mean free path of particles of the ith component (ith phase). The hydrodynamic, physically infinitely small volume $v_h \sim r_h^3$ is a point in the parameter space of the hydrodynamic variables.

A multifluid hydrodynamic flow regime may be established if the system is fairly inhomogeneous so that the relaxation times in the entire system, and within each component, differ substantially. Additionally, in order to ensure that each component (phase) is described hydrodynamically, the following condition must be satisfied

$$r_{hi} \gg l_i \gg r_{0i}, \quad i=1,2,\ldots, \tag{2}$$

where r_{hi} is the hydrodynamic, physically infinitely small, scale of the ith mixture component (ith phase). Obviously, the hydrodynamic, physically infinitely small scales for the carrier component r_{hf} and the dispersed component r_{hp} should differ fairly significantly.

The conditions (1) and especially (2) are fairly stringent. The latter will generally only be satisfied in real systems for molecular or finely dispersed systems. For moderately and coarsely dispersed systems, a multifluid flow regime will predominate. At the same time, it is appreciated that if the particles are fairly large, the condition for the existence of a hydrodynamic description of a dispersed liquid cannot be satisfied and this cannot be used. Using the hydrodynamic level of description in these cases leads to numerous paradoxes. An example is the prediction of an infinite velocity for a solid dispersed particle near a surface.

A commonly encountered situation is one where the carrier component can be described hydrodynamically, but the dispersed component cannot (such a situation is encountered when studying the flow of a coarsely dispersed liquid in a boundary layer). In these cases, a mixed level of description must be used: the carrier component, i.e., the gas or liquid, is described hydrodynamically while the dispersed component, i.e., the particles, is described kinetically. The aim of the present study is to construct this type of mixed description.

Let us assume that the carrier medium is not an extremely low-density gas. Its dynamics will then by described by hydrodynamics equations, which also contain the interphase interaction forces $\mathbf{F}_m$ and F_e

$$\frac{\partial \rho}{\partial t} + \nabla \cdot \rho \mathbf{u} = 0,$$

$$\rho \frac{\partial \mathbf{u}}{\partial t} + \rho \mathbf{u} \cdot \nabla \mathbf{u} + \nabla \cdot \mathbf{P} = \mathbf{F}_m,$$

$$\frac{\partial E}{\partial t} + \nabla \cdot E\mathbf{u} + \mathbf{P}:\nabla \mathbf{u} + \nabla \cdot \mathbf{q} = F_e. \tag{3}$$

The dynamics of the dispersed component will generally be described by the kinetic equation

$$\frac{\partial F_p}{\partial t} + \mathbf{V} \cdot \frac{\partial F_p}{\partial \mathbf{R}} = J_{pp}(F_p F_p) + J_{pg}(F_p F_g) \tag{4}$$

for the single-particle particle distribution function F_p. Here J_{pp} and J_{pg} are collision integrals and $\mathbf{V}$ and $\mathbf{R}$ are the velocity and coordinate of the particle center of mass, respectively.

Provided that the gaseous or liquid suspensions are not too dense, the particle collision integral J_{pp} may be modeled by the Boltzmann collision integral. In extremely low-density gaseous and liquid suspensions particle interaction can be neglected. This simplifies Eq. (4) significantly, and in this case, the particle collision integral J_{pp} can be dropped.

For low-density gaseous suspensions, the integral of particle collisions with molecules J_{pg} can also be modeled by the collision integral from the Boltzmann equation. When a molecule collides with a dispersed particle, the velocity of

the latter changes only slightly because its mass M is much greater than the molecular mass m: $\mu = m/M \ll 1$. By expanding the Boltzmann collision integral as a series with respect to the small parameter μ, it is easy to establish that this reduces to the Fokker–Planck collision integral.[3] For denser gaseous suspensions, in some cases the collision integral J_{pg} can be modeled by the Enskog collision integral.[4] However, in this case it will also reduce to the Fokker–Planck collision integral.

In general, the integral of collisions between dispersed particles and molecules of the carrier medium is not described by the Boltzmann (or Enskog) collision integral, even for finely dispersed gaseous suspensions.[5] This is because the particle–molecule interaction is essentially collective, and over a time of the order of the molecule–particle interaction time the particle undergoes many collisions with molecules. However, regardless of the type of collision integral, since the function F_p varies adiabatically in momentum space, it can also be represented in the form of the Fokker–Planck collision integral.

The form of the coefficient of friction appearing in the Fokker–Planck equation will be determined by the relationship between the dispersed particles and the carrier fluid. If the resisting force acting on the particle from the carrier fluid is described by the linear law $\mathbf{F}_f = -\mathbf{F}_p = K_u(\mathbf{u}_p - \mathbf{u}_f)$, which is widely used to solve problems in the mechanics of multiphase media, the dynamics of an extremely low-density dispersed medium will be described by the system (3) and the kinetic equation

$$\frac{\partial F_p}{\partial t} + \mathbf{V} \cdot \frac{\partial F_p}{\partial \mathbf{R}} = K_u \frac{\partial}{\partial \mathbf{V}} \cdot (\mathbf{V} F_p) + K_u \frac{kT}{2M} \frac{\partial^2 F_p}{\partial V^2}. \qquad (5)$$

The boundary conditions for the carrier component are the normal conditions of attachment (provided that the gas density is not too low) and those for the distribution function F_p are the conditions at the surface.

In general, the system of equations can contain additional terms associated with a more accurate description of the interphase forces, allowance for the thermophoretic force, and so on. A two-layer scheme for solving the problem can be used to describe real flows. For instance, when studying flow around a plate, the flow outside the boundary layer can be described hydrodynamically while that in the boundary layer can be described using Eqs. (3) and (4). At the interface of the boundary layer these results should be matched. The application of the system (3) and (4) will be described in a special study.

This work was supported by the RFBR (Grant No. 98-01-00719).

[1] S. L. Soo, *Fluid Dynamics of Multiphase Systems* (Blaisdell Publishing, Waltham, MA, 1967; Mir, Moscow, 1975, 536 pp.).
[2] R. I. Nigmatulin, *Dynamics of Multiphase Media*, Chap. I (Nauka, Moscow, 1987), 464 pp.
[3] D. Montgomery, Phys. Fluids **14**, 2088 (1971).
[4] S. Chapman and T. G. Cowling, 2nd ed. *Mathematical Theory of Non-Uniform Gases* (Cambridge University Press, Cambridge, 1952; Mir, Moscow, 1960, 510 pp.).
[5] V. Ya. Rudyak, Pis'ma Zh. Tekh. Fiz. **18**(20), 77 (1992) [Sov. Tech. Phys. Lett. **18**, 681 (1992)].

Translated by R. M. Durham

Coercive force of iron garnet films as a function of maximum external magnetic field strength

M. V. Logunov and M. G. Gerasimov

N. P. Ogarev Mordovian State University, Saransk
(Submitted November 17, 1998; resubmitted July 13, 1999)
Pis'ma Zh. Tekh. Fiz. **25**, 39–43 (November 26, 1999)

Results are presented of measurements of the coercive force of single-crystal iron garnet films using the half-width of the limiting and particular quasistatic hysteresis loops over a wide range of variation of the maximum magnetic field which reverses the magnetization of the film. Reasons for the disagreement between results obtained using various methods of measuring the coercive force are discussed. © *1999 American Institute of Physics.* [S1063-7850(99)02211-9]

The coercive force H_c is one of the fundamental parameters of a magnetic material characterizing its perfection. It is particularly interesting to study the coercive force of single-crystal iron garnet films which are among those magnetic materials having the most perfect crystal structure. Increasing attention has been addressed to this issue because the conditions of formation of ordered domain structures in magnetic films depend strongly on the coercive force and other parameters of the hysteresis loop.[1,2] So far, most data on the coercivity of iron garnet films have been obtained from studying hysteresis effects in alternating magnetic fields.[3–5] However, irreversible changes in the magnetization may be accompanied by the appearance of dynamism in the magnetic reversal process, including that at frequencies of tens of hertz.[6] In addition, the wide range of methods of studying coercive properties[5] and sample treatment,[5,7] and the range and gradient of the acting fields[8] present difficulties when the experimental results are compared.

Here we present results of measurements of the coercive force of (111)-oriented iron garnet films using the half-width of the limiting and particular hysteresis loops recorded by quasistatically varying the external magnetic field H. For comparison we also measured H_c using the method of domain wall oscillations[3–6] at 74 GHz. Both methods were used to study a region of the sample 1.5 mm in diameter. The field H was applied parallel to the easy magnetization axis perpendicular to the plane of the film. The results are given for a film having the composition $(Y, Lu, Gd, Bi)_3(Fe, Al)_5O_{12}$ and the parameters: thickness $h=2.9\ \mu$m, equilibrium period of stripe domains $P_0=5.8\ \mu$m, saturation magnetization $M_s=23$ G, and uniaxial anisotropy field $H_\kappa=1700$ Oe.

For iron garnet films there is a large difference between H_c and the saturation field of the film H_s (usually $H_s/H_c \sim 100$) which imposes additional constraints on the experimental apparatus.[4] In this study the measurements were made using a magnetooptic system based on the Faraday effect. High sensitivity was achieved by using modulated radiation from a microwave-pumped helium–neon laser as the light source, incorporating selective amplifiers in the differential signal recording system, and stabilizing the operating regimes of the system.[9] The magnetic field was regulated using an ambipolar electromagnet current stabilizer which allows measurements to be made with the magnetic field varied quasistatically at a given rate without mechanically reversing the current polarity.[10]

The maximum magnetic field H during recording of the hysteresis loops was varied over a wide range $H=(0.01–10)H_s$, where H_s is the saturation field of the film. The upper limit of this range was determined by the condition that H should be several times higher than the saturation field H_s to record the limiting hysteresis loops and the lower limit was determined by the fact that it should be 1.5–2 times higher than the coercive force H_c measured for the limiting loop. The rate of variation of H was 0.1–1 Oe/s. The hysteresis loops were typical of low-coercivity iron garnet films.[11] The field for nucleation of the domain structure during demagnetization from the saturated state is $H_n \sim 0.8H_s$.

The coercive force of the iron garnet films depends on the maximum magnetic field H achieved during magnetic reversal of the sample (Fig. 1) and the form of the dependence $H_c(H)$ changes substantially with increasing temperature and is accompanied by a reduction in the coercive

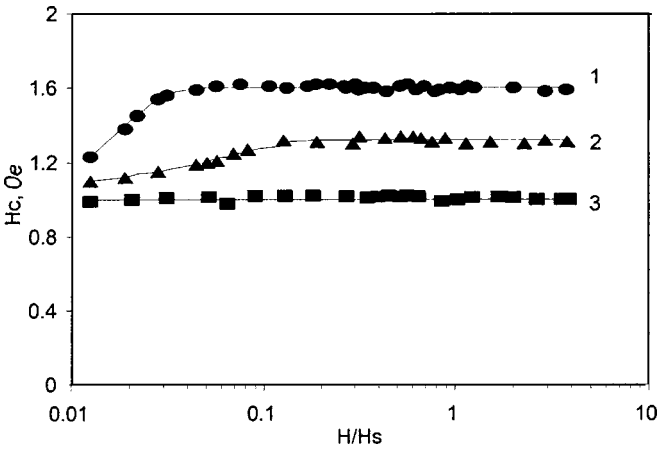

FIG. 1. Coercive force H_c as a function of maximum external magnetic field H at temperatures of 25 (*1*), 35 (*2*), and 45 °C (*3*).

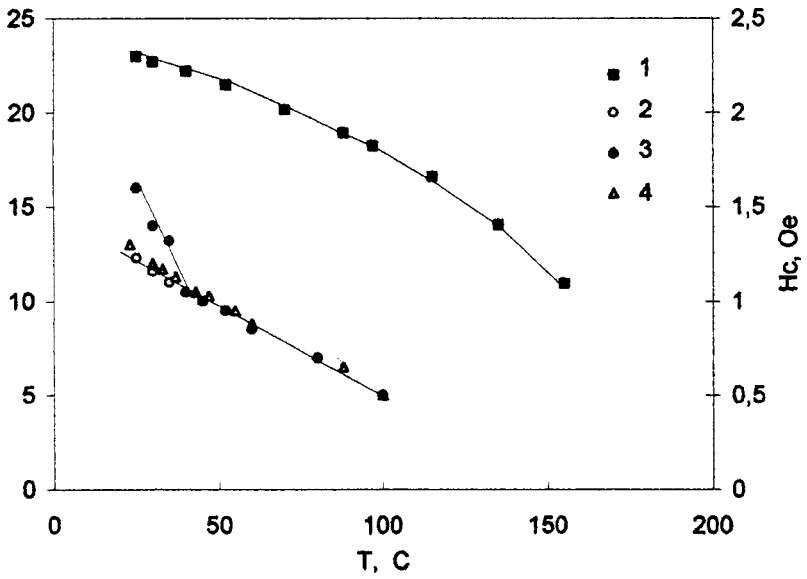

FIG. 2. Temperature dependences of the saturation magnetization M_s (*1*) and the coercive force H_c measured from the half-width of the particular (*2*, $H=2.5$ Oe) and limiting (*3*) hysteresis loops and using the domain wall oscillation method (*4*).

force.[12] This dependence may be characterized by the critical field H^*; for $H<H^*$ the width of the hysteresis loop begins to decrease. The value of H^* varies strongly with temperature: $H^*/H_c=3.5$ at $T=25$ °C and $H^*/H_c=15$ at $T=35$ °C. Such an appreciable variation of H^* occurs in a narrow range of temperature when the main magnetic parameters of the film, M_s (Fig. 2, curve *1*) and H_s vary by less than 10%. At the same time we find $H^*/H_n<0.1$, hence the reasons for the variation of H^* are not related to the domain nucleation processes. Leaving aside other possible mechanisms for the variation of H_c with temperature[13] caused by changes in the contributions of various types of defects to H_c, we note the factors which could be responsible for the contradictions between the results of measurements of the coercive force obtained by the method of domain wall oscillations and using the half-width of the hysteresis loop.

The oscillation method involves recording the amplitude of the domain wall shift as a function of the alternating magnetic field (essentially recording the envelope of the particular hysteresis loops). The coercivity field is determined by extrapolating the linear part of this dependence to zero domain wall shift. The results of the H_c measurements (Fig. 2, curve *4*) agree with those obtained using the half-width of the limiting hysteresis loop (Fig. 2, curve *3*) for the particular case when no dynamic effects appear during magnetic reversal in the alternating field and H_c does not depend on H (H_c is the same for the limiting and particular hysteresis loops, Fig. 1, curve *3*), and H_c is the same on the descending and ascending branches of the loop. For the results presented here this corresponds to $T>45$ °C. Hence, the difference between the values of H_c measured from the half-width of the limiting hysteresis loop and by the oscillation method is most pronounced near the kink on the temperature dependence of the coercive force.

The authors are grateful to A. Yu. Troshin for supplying the iron garnet films.

This work was supported by the RFBR, Grant No. 98-02-03325.

[1] I. E. Dikshteĭn, F. V. Lisovskiĭ, E. G. Mansvetova, and E. S. Chizhik, Zh. Éksp. Teor. Fiz. **100**, 1606 (1991) [Sov. Phys. JETP **73**, 888 (1991)].
[2] G. S. Kandaurova and V. Kh. Osadchenko, Pis'ma Zh. Tekh. Fiz. **20**(21), 24 (1994) [Tech. Phys. Lett. **20**, 864 (1994)].
[3] R. M. Josephs, AIP Conf. Proc. **10**, 286 (1972).
[4] G. A. Bazhazhin, E. N. Il'icheva, I. V. Mushenkova *et al.*, Zh. Tekh. Fiz. **55**, 396 (1985) [Sov. Phys. Tech. Phys. **30**, 233 (1985)].
[5] G. Vertesy, M. Pardavi-Horvath, L. Bodis, and I. Pinter, J. Magn. Magn. Mater. **75**, 389 (1988).
[6] O. V. Il'chishin and I. M. Makmak, Deposited Paper No. 2700 (UkrNIITI, Donetsk, Ukraine, 1986), 22. pp.
[7] A. Yu. Toropov, V. A. Klyuev, and M. V. Valeĭko, Pis'ma Zh. Tekh. Fiz. **24**(1), 73 (1998) [Tech. Phys. Lett. **24**, 33 (1998)].
[8] A. N. Grigorenko, S. A. Mishin, and E. G. Rudashevskiĭ, Pis'ma Zh. Tekh. Fiz. **13**, 1147 (1987) [Sov. Tech. Phys. Lett. **13**, 479 (1987)].
[9] M. V. Logunov and M. V. Gerasimov, in *Abstracts of papers presented at 15th All-Russia Seminar-School on New Magnetic Materials for Microelectronics, NMMM-XV*, Moscow, 1996 [in Russian], pp. 505–506.
[10] M. V. Logunov and V. D. Chervenkov, Prib. Tekh. Eksp. No. 1, 166 (1997).
[11] A. G. Shishkov, E. N. Il'icheva, and V. V. Grishachev, in *Abstracts of papers presented at 15th All-Russia Seminar-School on New Magnetic Materials for Microelectronics, NMMM-XV*, Moscow, 1996 [in Russian], pp. 163–164.
[12] M. V. Logunov and M. V. Gerasimov, in *Abstracts of papers presented at 16th All-Russia Seminar-School on New Magnetic Materials for Microelectronics, NMMM-XVI*, Moscow, 1998 [in Russian], pp. 559–560.
[13] G. Vértesy and I. Tomáš, J. Appl. Phys. **77**, 6426 (1995).

Translated by R. M. Durham

Kinetics of predetonation conductivity of silver azide

B. P. Aduev, É. D. Aluker, G. M. Belokurov, A. G. Krechetov, and A. Yu. Mitrofanov

Kemerovo State University
(Submitted June 3, 1999)
Pis'ma Zh. Tekh. Fiz. **25**, 44–48 (November 26, 1999)

The kinetics of the predetonation conductivity of silver azide have been measured with nanosecond time resolution. The experimental results are accurately approximated by an equation which includes multiplication of active particles by a first-order reaction and loss of these particles by a second-order reaction. © *1999 American Institute of Physics.* [S1063-7850(99)02311-3]

According to existing ideas,[1,2] the energy characteristics of the explosive decomposition of heavy metal azides are provided by the exothermic reaction $2N_3 \rightarrow N_6 \rightarrow 3N_2$. A necessary condition for this reaction is that two holes meet (evidently at a cationic vacancy), resulting in the appearance of two neighboring N_3 radicals which participate in this reaction. However, at present no experimental data are available, especially data on the kinetics of explosive decomposition, to confirm or refute this point of view.

An interesting possibility arose following the observation of predetonation conductivity whose kinetics should reflect those of predetonation decomposition.[3]

An investigation of the kinetics of predetonation conductivity would allow us to determine the order of the decomposition kinetics and thus serve as serious argument in support of (or against!) the bimolecular nature of the main exothermic reaction. This was the aim of the present study.

We investigated the kinetics of predetonation conductivity of silver azide whiskers ($\sim 2\times 0.1\times 0.15$ mm), mounted on the entry window of an acoustic detector. Explosive decomposition was initiated by a laser pulse (1064 nm, 10–20 mJ, 30 ps). The onset of deformation of the sample which subsequently develops into mechanical rupture (detonation) was determined from the leading edge of the acoustic signal. Details of the method are described in Ref. 4.

Typical current signal profiles are shown in Fig. 1a. These either comprise an asymmetric bell or a curve which reaches a plateau. The decay of the current signal correlates with the acoustic signal and is associated with the onset of mechanical damage to the sample.[4] A comparison between the amplitudes of signals of different profile reveals that the bell-shaped signal is observed in samples which fracture before the conductivity reaches a plateau.

Hence, even a qualitative analysis of the kinetics of predetonation conductivity shows that the rate of the chain reaction saturates and the heating and rupture of the sample are caused by the rate of heat release in the saturation regime exceeding the rate of heat removal.[5]

The simplest quantitative description of the observed kinetics is given by the following equation:

$$\frac{dn}{dt} = \alpha n - \beta n^2, \tag{1}$$

where n is the hole (electron) concentration.

The solution of Eq. (1) subject to the initial condition $n(t_0)=n_0$ is given by:

$$n(t) = \frac{\exp[\alpha(t-t_0)]}{n_\infty^{-1}\{\exp[\alpha(t-t_0)]-1\}+n_0^{-1}}, \tag{2}$$

where n_∞ is the concentration at the plateau, and t_0 and n_0

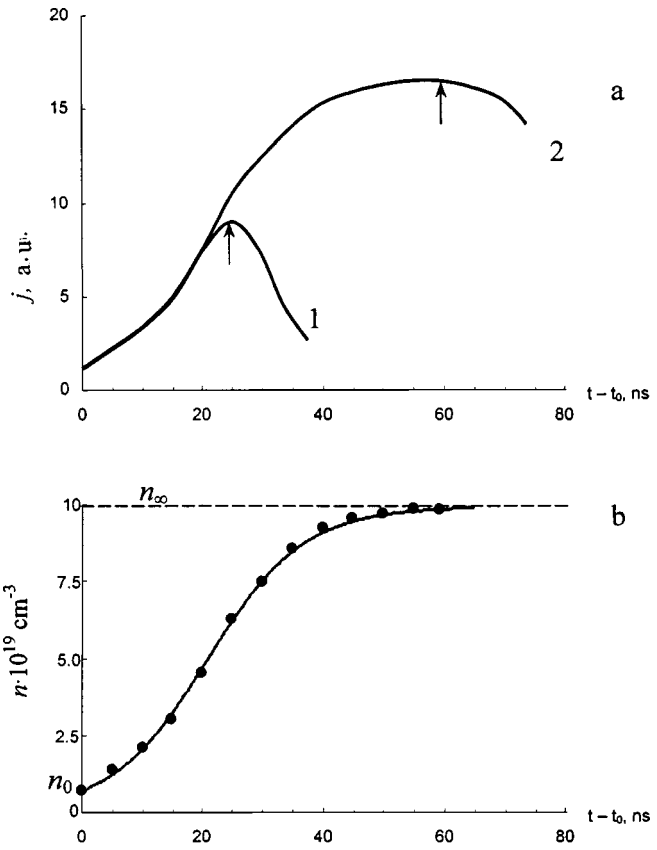

FIG. 1. Kinetics of predetonation conductivity of silver azide whiskers: a—typical profile of conductivity pulses, the arrows indicate the leading edge of the acoustic signal, *1*—bell-shaped pulse, *2*—pulse reaching a plateau, t_0 is the time at which the conductivity signal reaches a reliably measured value; b—kinetics of the concentration of band electrons (holes), the circles show the experimental conductivity measurements and the solid curve gives the approximation using expression (2).

are the time and concentration for which the conductivity reaches the reliably measured value (Fig. 1b).

The value of n in Fig. 1b is calculated from the relationship $\sigma = en\mu$ for $\mu \sim 10\,\mathrm{cm}^2 \cdot \mathrm{V}^{-1} \cdot \mathrm{s}^{-1}$ (Ref. 6).

We stress that the parameters t_0, n_0, and n_∞ in Eq. (2) are taken directly from the experimental curve and the only fitting parameter is α.

For all the samples studied, α lies in the range 10^{-8}–$10^{-9}\,\mathrm{s}^{-1}$, and β in the range 10^{-11}–$10^{-12}\,\mathrm{cm}^3 \cdot \mathrm{s}^{-1}$.

The good approximation of the experimental curves by expression (2) (Fig. 1b) casts doubts on the generally accepted (but not proven!) viewpoint that the main exothermic decomposition reaction of heavy metal azides is a bimolecular reaction.[2] In fact, the simplest treatment of Eq. (1), whose solution is given by expression (2), is that the evolution (branching) of the chain is determined by a unimolecular process (αn) and the termination is determined by a bimolecular process (βn^2).

In order to put forward a reasonable hypothesis on the nature of the corresponding processes, it is advisable to analyze the experimental values $\alpha \approx 10^{-8}$–$10^{-9}\,\mathrm{s}^{-1}$ and $\beta \approx 10^{-11}$–$10^{-12}\,\mathrm{cm}^3 \cdot \mathrm{s}^{-1}$.

It is simplest to begin with $\beta = vS_\tau$, where v is the thermal velocity of an electron (hole) and S_τ is the cross section of the process responsible for terminating the chain. For $v \sim 10^7\,\mathrm{cm} \cdot \mathrm{s}^{-1}$ we obtain $S_\tau \approx 10^{-18}$–$10^{-19}\,\mathrm{cm}^2$. These values of S_τ are typical of indirect interband recombination.[7] That is to say, the simplest treatment of bimolecular chain termination involves interband recombination of electrons and holes.

The simplest interpretation of the linear evolution of the chain (αn) involves capture of holes by point defects. In this case, we find $\alpha = vS_3N$, where v is the thermal velocity, S_3 is the capture cross section, and N is the defect concentration. For $v \sim 10^7\,\mathrm{cm} \cdot \mathrm{s}^{-1}$ and $N \sim 10^{15}\,\mathrm{cm}^{-3}$ (a typical concentration of cationic vacancies in silver azide whiskers[8]) we obtain $S_3 \sim 10^{-14}\,\mathrm{cm}^2$, i.e., a typical cross section for capture at an attracting center.[9] Thus the evolution of the chain may be attributed to the capture of holes at cationic vacancies (attracting centers).

These data therefore contradict the hypothesis that the main exothermic reaction responsible for the explosive decomposition of AgN_3 is bimolecular.

In our opinion, these results suggest and fairly well substantiate (at least at this stage of the research) the hypothesis that the evolution of the explosive decomposition chain reaction of heavy metal azides is determined by a unimolecular process of hole capture by cationic vacancies and chain termination is determined by bimolecular interband recombination of electrons and holes.

This work was supported by the RFBR (Grant No. 98-03-32001a).

[1] F. P. Bowden and A. D. Yoffe, *Fast Reactions in Solids*, (Butterworths, London, 1958), p. 242.
[2] *Energetic Materials*, Vol. 1, edited by H. D. Fair and R. F. Walker (Plenum Press, New York, 1987), p. 501.
[3] B. P. Aduev, E. D. Aluker, G. M. Belokurov, and A. G. Krechetov, JETP Lett. **62**, 215 (1995).
[4] B. P. Aduev, E. D. Aluker, G. M. Belokurov, and A. G. Krechetov, Russ. Phys. J. **39**, 1135 (1996).
[5] N. N. Semenov, *Chain Reactions* (Nauka, Moscow, 1986), 534 pp.
[6] V. I. Krasheninin, L. V. Kuz'mina, V. Yu. Zakharov, and A. Yu. Stalinin, Khim. Fiz. **14**(4), 126 (1995).
[7] O. V. Bogdanovich, S. A. Darznek, and P. G. Eliseev, *Semiconductor Lasers* (Nauka, Moscow, 1976), 415 pp.
[8] F. I. Ivanov, Dissertation for Doctor of Chemical Science [in Russian], Kemerovo (1997), 385 pp.
[9] A. M. Stoneham, *Theory of Defects in Solids: the Electronic Structure of Defects in Insulators and Semiconductors* (Clarendon Press, Oxford, 1975; Mir, Moscow, 1978, 926 pp.).

Translated by R. M. Durham

Phase multistability in quasiperiodically driven systems

T. E. Vadivasova, O. N. Sosnovtseva, and A. G. Balanov

N. G. Chernyshevskiĭ State University, Saratov
(Submitted May 31. 1999)
Pis'ma Zh. Tekh. Fiz. **25**, 49–56 (November 26, 1999)

The influence of quasiperiodic driving on phase multistability in coupled Feigenbaum oscillators is investigated. Various new effects associated with strange nonchaotic attractors are observed. [S1063-7850(99)02411-8]

A characteristic feature of the interaction of oscillators having a Feigenbaum mechanism of chaos formation is the establishment of multistability of periodic and chaotic regimes.[1–5] In this case, multistability is associated with the possible mutual synchronization of the oscillators in different phases relative to each other, and can thus be described as phase multistability. For periodic oscillations having undergone k period doublings, the number of possible limit cycles in the phase space of the interacting oscillators becomes 2^k. The phase shift between the oscillators may have values of $\phi_0+2\pi m$, where $m=0,1,2,\ldots 2^k-1$. In discrete-time systems, $\phi_0=0$ and it becomes meaningful to talk of the number of iterations by which the oscillations of the partial systems are shifted as a function of time. Phase multistability is conserved on transition to weakly advanced chaos.

In the present paper we consider how phase multistability is influenced by a quasiperiodic external action. We investigate a system of coupled logistic mappings in each of which we introduce a quasiperiodic excitation having the same rotation number:

$$\begin{aligned} x_{n+1}&=\varepsilon-x_n^2+\gamma(x_n^2-y_n^2)+a_1\cos 2\pi z_n,\\ y_{n+1}&=\varepsilon-y_n^2+\gamma(y_n^2-x_n^2)+a_2\cos 2\pi z_n,\\ z_{n+1}&=z_n+W, \quad \mod 1, \end{aligned} \tag{1}$$

where x_n and y_n are the dynamic variables of the partial systems, ε is the nonlinearity parameter, γ is the coupling parameter, z_n is the phase of the action which is assumed to be the same for both partial systems, and W is the rotation number determined by the external force (which corresponds to the ratio of the frequencies of action in the flow system). This was fixed as equal to the golden section: $W=0.5\times(\sqrt{5}-1)$. The term mod 1 implies that $0\leqslant z_n\leqslant 1$. The amplitudes of the action on the first and second oscillator are: $a_1=a_0$ and $a_2=pa_0$, respectively, where p is the detuning of the amplitudes. We assumed that no detuning occurs ($p=1$) and in this case, the system (1) has an invariant manifold U defined by the condition $x_y=y_n$. Trajectories starting from points belonging to U never leave the invariant manifold. The motion in the plane U corresponds to the case $m=0$ and is called cophasal. Regimes for which $m\neq 0$ are called noncophasal. The corresponding phase trajectories do not lie in U. Multistability in the system (1) in the absence of any external action ($a_0=0$) was investigated in Refs. 3 and 4. In the presence of weak coupling, these workers observed the coexistence of regimes ascribed to several branches generated by limit cycles corresponding to different values of m. As the parameter ε increases, chaotic regimes of different branches appear and these subsequently combine to form a global chaotic attractor. As the coupling parameter γ increases, the noncophasal regimes disappear and a transition to so-called complete synchronization is observed.[5,6]

Investigations of the system (1) made in the present study for $a_0\neq 0$, $p=1$, and $\gamma=0.002$, showed that phase multistability is fairly coarse relative to a weak quasiperiodic action. The main branches of regimes which existed in the autonomous system are conserved. However, instead of periodic oscillations, we observe quasiperiodic regimes and regimes corresponding to a strange nonchaotic attractor.[7–12] The latter occur as a result of fractalization of the invariant closed curve which is the transform image of the two-frequency quasiperiodic oscillations in a discrete-time system. In the system (1) we observe two mechanisms for fractalization: 1) a gradual distortion of the curve profile, resulting in a loss of smoothness;[11] 2) instantaneous fractalization as a result of a crisis occasioned by contact between the stable and unstable invariant curve.[8,9] For diagnostics of this strange nonchaotic attractor regime we used the phase sensitivity criterion proposed in Ref. 10, in addition to calculations of the Lyapunov exponents. For conciseness, we shall adopt the following notation for the dynamic regimes: T are quasiperiodic two-frequency oscillations, SNA is a strange nonchaotic attractor, SA is a strange attractor, the number preceding the letters indicates the number of attractor ribbons (parts), and the superscript: 0, 1, 2, 3 is equal to the number m which determines the phase shift between the sequences x_n and y_n. The symbol Σ indicates that limit sets of different branches combine.

The sequence of regimes with increasing ε, typical of small amplitudes a_0, is shown in Fig. 1a ($a_0=0.01$). Three branches of regimes: **A**, **B**, and **C**, created by quasiperiodic attractors for which $m=0,1$, and 2, respectively, are indicated. The cophasal quasiperiodic attractor T^0 (branch **A**) undergoes two doubling bifurcations (for $\varepsilon\approx 0.750$ and $\varepsilon\approx 1.253$) after which it becomes fractalized by the first of the methods specified ($\varepsilon\approx 1.376$). The formation of an SNA in the invariant manifold U is accompanied by a loss of coarseness of the cophasal regime. If the initial point is defined outside the manifold U, long-term transient intermit-

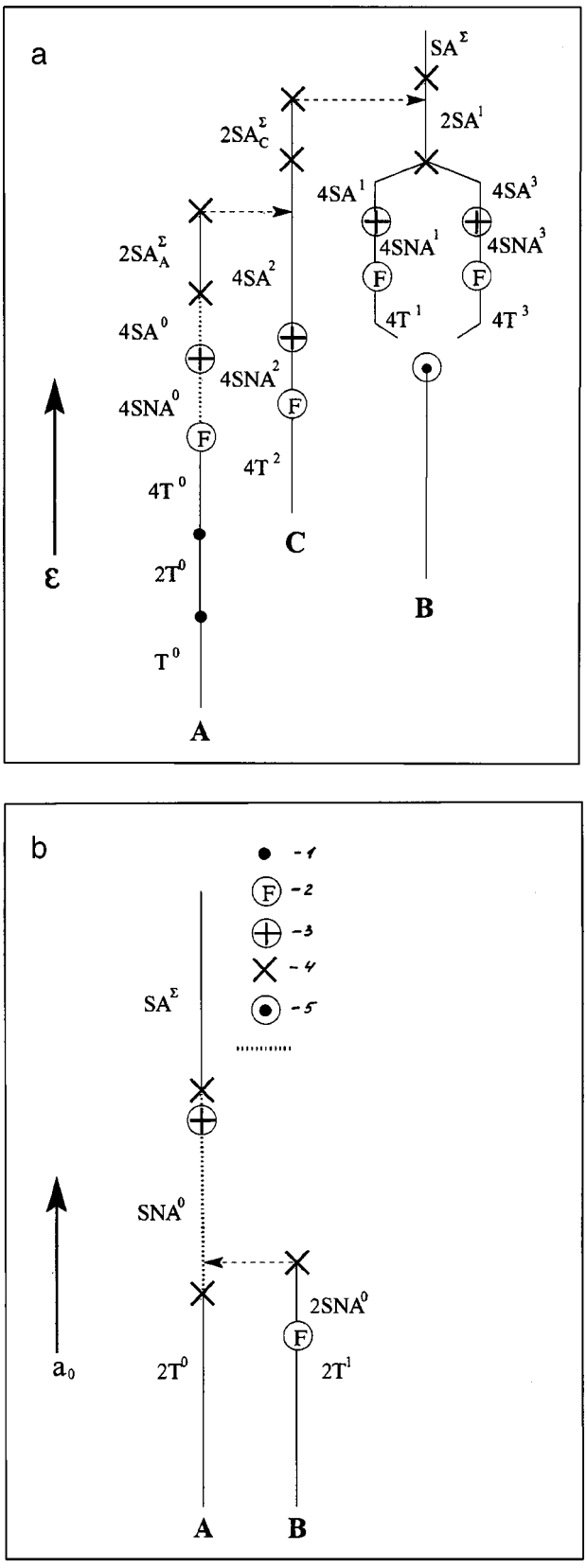

FIG. 1. Diagram showing regimes of system (1) without detuning ($p=1$): a —for varying parameter ε and constant $a_0=0.1$; b—for varying a_0 and constant $\varepsilon=1.2$: *1*—period doubling, *2*—fractalization of invariant curve, *3*—boundary of chaos, *4*—crisis, *5*—creation of three-dimensional torus, and *6*—sections of smooth attractor.

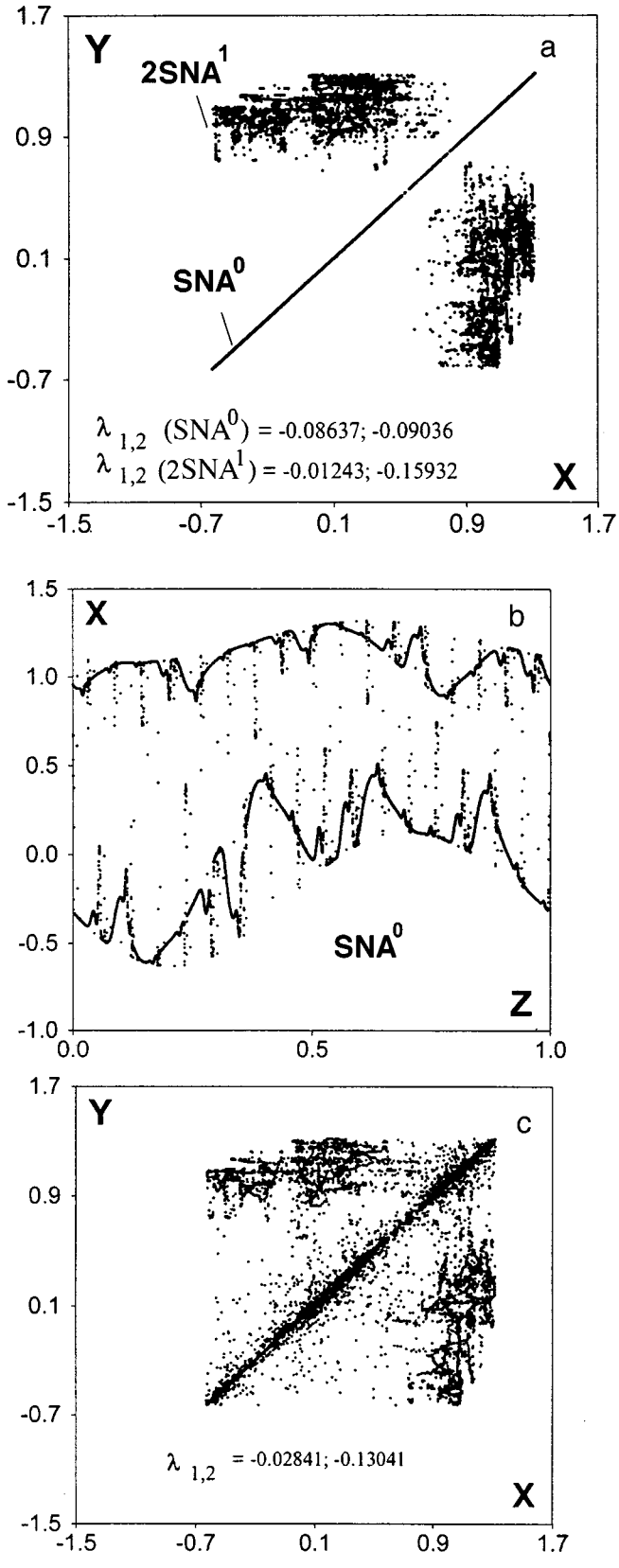

FIG. 2. Projections of strange nonchaotic attractors and corresponding nonzero Lyapunov exponents for $\varepsilon=1.2$: a—**X**–**Y** projections of coexisting attractors SNA^0 and $2SNA^1$; b—**X**–**Z** projection of SNA^0 attractor; c— **X**–**Y** projection of nonchaotic intermittence regime observed when the detuning $p=1.0001$ is introduced.

tence is observed.[13–15] A small detuning of the action amplitudes (≈ 1.0001) or weak noise give rise to ''bubbling'' phenomena.[13,14] This behavior suggests that not only a chaotic attractor but also a strange nonchaotic attractor may possess the properties of a Milnor attractor.[16] A further increase in ε leads to a blowout bifurcation at $\varepsilon \approx 1.380$, which is diagnosed from a change in the sign of the transversal Lyapunov exponent.[6,15] However, in all the cases studied, a transition to chaotic behavior preceded a blowout bifurcation. For $a_0 = 0.01$ a transition to chaos is observed for $\varepsilon \approx 1.379$. After a blowout bifurcation the $2SA_A^{\Sigma}$ attractor forms, no long lying within U. This attractor then becomes a chaotic saddle ($\varepsilon \approx 1.392$) and the mapping point goes over to the **C** branch attractor. The noncophasal **C** branch chaos evolves according to a similar scenario: T→SNA→SA (for $\varepsilon \approx 1.378$ and $\varepsilon \approx 1.379$, respectively). For $\varepsilon \approx 1.394$ the parts of the branch C chaotic attractor combine accompanied by the simultaneous connection of the branch **A** chaotic saddle. The ensuing combined chaos $2SA_C^{\Sigma}$ also ceases to be attractive for $\varepsilon \approx 1.519$ and the mapping point switches to the branch **B** attractor. Branch **B** is characterized by the creation of a three-frequency quasiperiodic regime ($\varepsilon \approx 1.25q$) whose transform is a two-dimensional mapping torus. A pair of invariant closed curves $4T^1$ and $4T^3$ corresponding to $m = 1$ and 3 are generated on the torus. These possess the property of mutual symmetry with respect to the transposition $x_n \rightarrow y_n$. As ε increases, they undergo fractalization ($\varepsilon \approx 1.382$) and chaos ensues ($\varepsilon \approx 1.385$). The chaotic attractors $4SA^1$ and $4SA^3$ combine at $\varepsilon \approx 1.398$ to form a single attractor $2SA^1$. For $\varepsilon \approx 1.523$ the attractor $2SA^1$ combines with a nonattracting chaotic set and the global attractor SA^{Σ} appears, which incorporates the chaotic sets of all branches.

From a certain value of the action amplitude a_0, multistability disappears. Figure 1b shows a sequence of regimes for $\varepsilon = 1.2$ when the amplitude varies between $a_0 \approx 0.118$ and $a_0 \approx 0.130$. Here we only observe regimes of branches **A** and **B** which combine as a_0 increases. For $a_0 \approx 0.1185$ the cophasal quasiperiodic attractor $2T^0$ (branch **A**) undergoes a crisis, which is accompanied by parts of the attractor combining.[8] As a result, the invariant curve becomes fractalized and the cophasal strange nonchaotic attractor SNA^0 appears. On branch **B** the curve $2T^1$ ($a_0 \approx 0.1182$) also fractalizes but without any crisis and the noncoaphsal attractor $2SNA^1$ appears. The projections of SNA^0 and $2SNA^1$ are shown in Figs. 2a and 2b. For $a_0 \approx 0.1188$ the nonchaotic fractal set of branch **B** ceases to be attracting. The attractor SNA^0 becomes the only one in the phase space but it is coarse. The detuning $p = 1.0001$ causes the nonchaotic fractal sets of branches **A** and **B** to combine. The combined attractor (Fig. 2a) is also not chaotic. In the absence of detuning the transition to chaos and the blowout bifurcation are observed almost simultaneously for $a_0 \approx 0.1260$, followed by the formation of the combined chaotic attractor SA^{Σ}.

This work was partially supported by RFBR Grant No. 98-02-16531. One of the authors (T.E.V) is also grateful for the support of the International Soros Program in the Exact Sciences (Grant No. d99-835, 1999).

[1] K. Kaneko, Prog. Theor. Phys. **69**, 1427 (1983).
[2] S. P. Kuznetsov, Izv. Vyssh. Uchebn. Zaved., Radiofiz. **28**, 991 (1985).
[3] V. V. Astakhov, B. P. Bezruchko, and E. P. Seleznev, Pis'ma Zh. Tekh. Fiz. **15**(3), 60 (1989) [Sov. Tech. Phys. Lett. **15**, 105 (1989)].
[4] V. V. Astakhov, B. P. Bezruchko, E. N. Erastova *et al.*, Zh. Tekh. Fiz. **60**(10), 19 (1990) [Sov. Phys. Tech. Phys. **35**, 1122 (1990)].
[5] D. E. Postnov, T. E. Vadivasova, O. V. Sosnovtseva' *et al.*, Chaos **9**(1), 227 (1999).
[6] L. M. Pecora and T. L. Carroll, Phys. Rev. Lett. **64**, 821 (1990).
[7] C. Grebogi *et al.*, Physica D **13**, 261 (1984).
[8] J. F. Heagy and S. M. Hammej, Physica D **70**, 140 (1994).
[9] U. Feudel and A. S. Pikovsky, Physica D **88**, 176 (1995).
[10] A. S. Pikovsky and U. Feudel, Chaos **5**, 253 (1995).
[11] V. S. Anishchenko, T. E. Vadivasova, and O. V. Sosnovtseva, Phys. Rev. E **53**, 4451 (1996).
[12] R. Ramaswamy, Phys. Rev. E **56**, 7294 (1997).
[13] P. Ashwin, J. Buescu, and I. Stewart, Nonlinearity **9**, 703 (1994).
[14] M. Hasler and Y. Maistrenko, IEEE Trans. Circuits Syst., I: Fundam. Theory Appl. **44**, 856 (1997).
[15] E. Ott and J. C. Sommerer, Phys. Lett. A **188**, 39 (1994).
[16] J. Milnor, Commun. Math. Phys. **99**, 177 (1985).

Translated by R. M. Durham

Electroluminescence of lead magnoniobate with heterodyned acoustic-frequency exciting fields

N. N. Kraĭnik and S. A. Flerova

A. F. Ioffe Physicotechnical Institute, Russian Academy of Sciences, St. Petersburg Dnepropetrovsk State University, Ukraine

(Submitted August 3, 1999)
Pis'ma Zh. Tekh. Fiz. **25**, 57–60 (November 26, 1999)

Electroluminescence of the model ferroelectric relaxor, lead magnoniobate, above the freezing point is studied when the exciting sinusoidal electric fields are heterodyned. An abrupt rise in the luminescence is observed near the maximum amplitudes of the carrier-frequency field.
 [S1063-7850(99)02511-2]

Ferroelectric relaxors are currently being studied in various contexts since they are an important part of the general problem of the physics of disordered systems, which primarily involves identifying the mechanism responsible for this disorder. These studies are also particularly relevant because of the potential practical applications of relaxors.

The present paper is devoted to studying the dynamic behavior of the model ferroelectric relaxor lead magnoniobate $PbMg_{1/3}Nb_{2/3}O_3$ (PMN) using its electroluminescence in strong, modulated, sinusoidal electric fields above its freezing point. The samples are investigated under conditions where the fluctuations of the ion displacements in the main part of the crystal bulk are fairly short-lived.

The luminescence observed as a result of switching the polarization of PMN in strong fields provides additional and independent information on the dynamics of polarization and depolarization processes, and also on domain-like and heterophase hysteresis phenomena (see, for example, Refs. 1–3). In order to obtain experimental data on the kinetics of the evolution of PMN electroluminescence in strong electric fields, we used a method of heterodyning the exciting fields.

For the investigations we used PMN single crystals grown by a modified spontaneous-crystallization method.[4] An exciting voltage was applied via InGa electrodes to single-crystal wafers 0.2–0.7 mm thick, using two sources of sinusoidal electric oscillations at frequencies f_1 and f_2 in the acoustic range. As a result of heterodyning, an amplitude-modulated signal of frequency $|f_1-f_2|$ acted on the crystal.[5] This technique allowed us to increase the amplitude of the exciting field, prevented any heating of the sample, and could be used to determine the crystal photoresponse under systematically and smoothly increasing (decreasing) amplitudes of the carrier-frequency field. In each sinusoidal packet the maximum electric field E_{max} reached 25 kV/cm. At this stage of the research, particular attention was directed toward the zero-beat regimes when $f_1 \cong f_2$. The electric field was applied in the [001] pseudocubic direction and the luminescence was recorded from the lateral surfaces of the sample using an FÉU-97 photomultiplier and an S8-17 storage oscilloscope. Results of measurements at 300 K are presented. The samples were optically homogeneous with no defects visible under a microscope.

Figure 1 shows oscilloscope traces of the electroluminescence, typical of all the samples studied. Before specific electric field strengths were reached, the envelope of the photopulse packet was similar to the envelope of a packet of positive or negative half-periods of the sinusoidal exciting field (see Fig. 1, frame *1*). At a specific value E_{max}, abrupt surges of electroluminescence intensity suddenly appear (frame *2*), increasing in an avalanche-like fashion and becoming broader as the exciting field increases (frames *3* and *4*). The ''pedestal'' of the photopulse packet also varies (frames *4–6*; only part of the pulse is shown in frame *6*). The field E_{max} at which the first intensity surges appear depends on the crystal thickness. For thicknesses of 0.68, 0.425, and 0.25 mm the values of E_{max} were 6.4, 10.5, and 15.4 kV/cm, respectively. One reason for this dependence may a difference between the conditions for emission of radiation from crystals of different thickness. However, further studies are required to clarify this issue definitively.

Electroluminescence in ferroelectrics in general, and in the ferroelectric relaxor PMN in particular, is a cooperative effect in which, depending on the crystal state and the excitation conditions, ensembles of domains or domain-like formations of different levels luminesce (such as isolated polar regions, ferroclusters, and so on). These results show that under the influence of a fairly strong increasing electric field, cascade growth and transformation of switchable regions take place with changes in the dynamics of the domain and heterophase boundaries in these regions, accompanied by an avalanche-like rise in the luminescence signal. For example, when the field E_{max} increased from 15 to 25 kV/cm, the luminescence intensity at the maximum increased by more than three orders of magnitude. Moreover, the photopulse packet acquired a multistepped profile. The different regions of the packet may correspond to different mechanisms for switching and establishment of the polarization, and also for the subsequent depolarization. The change in the PMN electroluminescence recorded in the present study suggests that flow processes take place in this particular range of electric fields, although insufficient data are available to indicate the formation of an infinite cluster.[6]

We are of the opinion that further studies of the electroluminescence of ferroelectric relaxors excited in hetero-

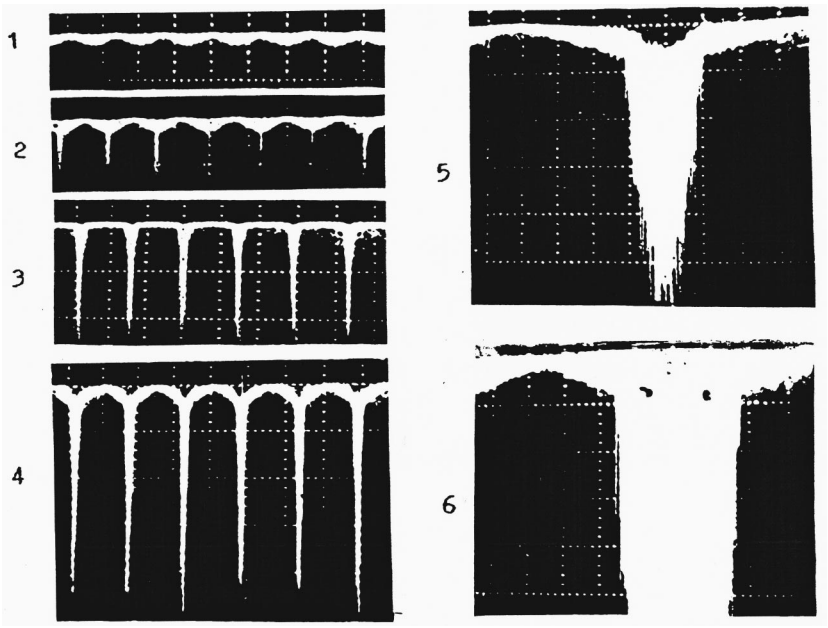

FIG. 1. Examples of oscilloscope traces of the electroluminescence (*1–6*) during heterodyning at frequencies $f_1 \cong f_2 \cong 985$ Hz. Maximum electric field strength in the sinusoidal packet E_{max}, kV/cm: 12.9 (*1*), 15.4 (*2*), 16.8 (*3*), 18.2 (*4*), 16.5 (*5*), and 17.5 (*6*). Vertical sensitivity, V/division: 0.02 (*1–3*), 0.05 (*5–6*), and 0.1 (*4*). Sweep time, s/division: 1.0 (*1–4*) and 0.2 (*5, 6*). Sample thickness $d = 0.25$ mm. Photomultiplier voltage, kV: 1.2 (*1–4*) and 1.5 (*5, 6*).

dyning regimes are of interest to identify the electroluminescence mechanisms and to determine the processes of polarization reversal as a function of the spectral composition of the applied voltage.

[1] N. N. Krainik, L. S. Kamzina, and S. A. Flerova, Ferroelectrics **208**, 363 (1998).
[2] S. A. Flerova, A. Yu. Kudzin, O. E. Bochkov, and N. N. Kraĭnik, Fiz. Tverd. Tela (Leningrad) **31**(2), 123 (1989) [Sov. Phys. Solid State **31**, 243 (1989)].
[3] S. A. Flerova, S. A. Popov, N. N. Kraĭnik, O. E. Bochkov, and A. P. Lazarev, Fiz. Tverd. Tela (Leningrad) **27**, 3492 (1985) [Sov. Phys. Solid State **27**, 2108, (1985)].
[4] I. E. Myl'nikova and V. A. Bokov, *Crystal Growth*, Vol. 3 [in Russian], Academy of Sciences of the USSR Press, Moscow (1961), pp. 438–446.
[5] A. M. Bonch-Bruevich, *Radio Electronics in Experimental Physics*, (Nauka, Moscow, 1966), pp. 92, 142–144, 396.
[6] J. M. Ziman, *Models of Disorder: the Theoretical Physics of Homogeneously Disordered Systems* (Cambridge University Press, Cambridge, 1979 ; Mir, Moscow, 1982, 591 pp.).

Translated by R. M. Durham

Characteristics of four-wave mixing in a Bose-condensed atomic gas

I. E. Mazets

A. F. Ioffe Physicotechnical Institute, St. Petersburg
(Submitted August 3, 1999)
Pis'ma Zh. Tekh. Fiz. **25**, 61–64 (November 26, 1999)

An analysis is made of four-wave mixing of laser radiation interacting with an ultracold degenerate ensemble of boson atoms trapped in a magnetic trap. It is shown that the existence of long-range order in this type of atomic system leads to a new mechanism for the generation of the reversed wave whose experimental manifestation should differ from four-wave mixing in a nondegenerate gas. A similar nonlinear optical effect may be used for diagnostics of an ultracold gas at temperatures not much lower than the phase transition temperature. © *1999 American Institute of Physics.* [S1063-7850(99)02611-7]

Studies of Bose–Einstein condensates of neutral atomic gases have recently become a rapidly developing field of science on the border between atomic physics and physics of condensed media (see reviews presented in Refs. 1–3). These systems are of interest from the fundamental research point of view primarily because the interatomic interaction in them, unlike that in liquid helium, is fairly weak which makes it possible to construct an exact quantitative theory and compare the results with precision experiments. From the practical point of view, a Bose condensate is important as the basic element of an atomic beam source with a large spatial coherence length, i.e., an atom laser.[2,4]

At present, optical methods based on the absorption or refraction of laser radiation in a cloud of ultracold atoms are widely used for the diagnostics of a neutral atom condensate.[2,3] Javanainen[5] and You *et al.*[6] developed a linear theory in terms of the intensity of the incident wave field. Qualitatively, its conclusions can be put forward as follows: in a condensate, in addition to incoherent scattering characterized by the radiative half-width γ, coherent scattering of incident photons also takes place at the wavelength $\lambda = 2\pi/k$, in resonance with the atomic transition to the first excited state. The scattering takes place predominantly in the forward direction in the small angle $\Omega \approx \frac{3}{2}(kR)^{-2}$, where R is the size of the atomic cloud. The corresponding line half-width is $\Gamma = \gamma N \Omega$, where N is the number of atoms in the condensate. When N is fairly large, coherent photon scattering becomes more probable than incoherent scattering.

Similarly, it may be predicted that the specific characteristics of a Bose condensate should also appear when laser radiation interacts nonlinearly with this condensate. In the present study a theoretical analysis is made of the formation of a light-induced grating in a Bose condensate in the field of a standing light wave.

As we know,[1,3] the macroscopic wave function Ψ of an atomic-gas Bose condensate normalized to the condition $\int |\Psi|^2 d^3\mathbf{r} = N$, is described by the Gross–Pitaevskiĭ equation

$$i\hbar \frac{\partial}{\partial t}\Psi = -\frac{\hbar^2}{2M}\nabla^2\Psi + U\Psi + g|\Psi|^2\Psi, \tag{1}$$

where M is the atomic mass and g is the interatomic interaction constant which, for alkali metals, has typical values of the order of $10^{-38}\,\mathrm{erg}\cdot\mathrm{cm}^{-3}$. In our case, the external potential

$$U = \frac{M}{2}\omega_{tr}^2 r^2 + 2V_0 \cos(2\mathbf{qr}) \tag{2}$$

includes, in addition to the harmonic potential of the trap (the first term on the right-hand side which, for simplicity, we assume to be isotropic), the Stark shift in the field of two light waves intersecting at the angle ϑ, i.e., $q = k\sin(\vartheta/2)$. We also have $V_0 = D^2E^2/(\hbar\Delta)$, where E and D are the amplitude of the light wave and the matrix element of the electric dipole moment of the transition, respectively. The detuning Δ of the laser frequency from resonance is assumed to be large compared with γ, which means that incoherent scattering leading to escape of atoms from the condensate can be eliminated.

We shall seek a steady-state solution of Eq. (1) corresponding to the ground state: $\Psi = \psi \exp(-i\mu t/\hbar)$, where μ is the chemical potential of the system. If the maximum Stark shift is small compared with the chemical potential, an approximate solution may be obtained using perturbation theory:

$$\psi = \psi_0(1 - f\cos(2\mathbf{qr})), \tag{3}$$

where the unperturbed solution is determined from

$$\mu\psi_0 = -\frac{\hbar^2}{2M}\nabla^2\psi_0 + \frac{M}{2}\omega_{tr}^2 r^2\psi_0 + g|\psi_0|^2\psi_0, \tag{4}$$

and the small correction contains the factor

$$f = V_0/(\hbar^2 q^2/M + g|\psi_0|^2). \tag{5}$$

Thus, the existence of a spatially modulated potential leads to the formation of a light-induced density grating in the Bose condensate. For comparison, we note that in a nondegenerate gas described by a Boltzmann distribution, the formation of a light-induced grating accounting for 1% of the total number of atoms, takes place for $V_0 \approx 10^{-24}$ erg at a

temperature of around 1 μK, which is substantially lower than the standard temperatures of the atoms in magnetooptic traps.

However, the main distinguishing feature for a Bose condensate is that the solution (3) corresponds to finding N atoms in a coherent superposition of the unperturbed solution and the spatially modulated state corresponding to a light-induced density grating. Thus, when a third (probe) light wave is applied, this being incident on the condensate at a certain angle determined by energy and momentum conservation laws, coherent scattering of photons may take place accompanied by a change in their wave vector of $\mathbf{q}$. If a light-induced grating having the spatial dependence $\cos(2\mathbf{qr})$ is created in the nondegenerate gas, generation of the reversed wave will be accompanied by a change in the wave vector of $2\mathbf{q}$ (Ref. 7).

By analogy with the case of coherent forward scattering,[5,6] the collective width Γ_q of the coherent scattering process in which the wave vector changes by $\mathbf{q}$ is calculated using the Wigner–Weisskopf theory:

$$\Gamma_q = f^2 \gamma N \Omega/2. \tag{6}$$

The simplest estimate of the cross section for this process gives[5]

$$\sigma_q \approx \frac{\lambda^2}{2\pi\Omega} \frac{\Gamma\Gamma_q}{\Delta^2+\Gamma^2}. \tag{7}$$

Since the chemical potential of a Bose condensate in a trap is usually substantially lower than the single-photon recoil energy $\hbar^2 k^2/(2M)$, the cross section contains a strong dependence on the angle ϑ of intersection of the light beams forming the grating. An estimate shows that four-wave mixing in a Bose condensate will take place fairly efficiently for small ϑ of around a few degrees. The angle of deflection of the coherently scattered beam at the grating will also be of the same order. The cone expansion angle in which the photons are coherently scattered is at least an order of magnitude lower so that the probe and signal beams can be easily distinguished.

This characteristic feature of four-wave mixing of laser radiation may be used to determine the presence of a condensate in a cloud of atoms in a trap at temperatures slightly below the phase transition temperature when the above-condensate fraction of the ensemble is fairly large, making it difficult to use simple optical methods of diagnostics.

This work was supported by RFBR Grant No. 99-02-17076.

[1] L. P. Pitaevskiĭ, Usp. Fiz. Nauk **168**, 641 (1998).
[2] M. R. Andrews, D. S. Durfee, S. Inouye, D. M. Stamper-Kurn, H.-J. Miesner, and W. Ketterle, J. Low Temp. Phys. **110**(1), 153 (1998).
[3] F. Dalfovo, S. Giorgini, L. P. Pitaevskii, and S. Stringari, Rev. Mod. Phys. **71**, 463 (1999).
[4] I. Bloch, T. Hänsch, and T. Esslinger, Phys. Rev. Lett. **82**, 3008 (1999).
[5] J. Javanainen, Phys. Rev. Lett. **72**, 2375 (1994).
[6] L. You, M. Lewenstein, R. J. Glauber, and J. Cooper, Phys. Rev. A **53**, 329 (1999).
[7] B. Ya. Zel'dovich, N. F. Pilipetskiĭ, and V. V. Shkunov, *Phase Conjugation* (Nauka, Moscow, 1985), 247 pp.

Translated by R. M. Durham

Phase dependence of the superconducting current in YBCO Josephson junctions on a bicrystal substrate

G. A. Ovsyannikov, I. V. Borisenko, K. I. Konstantinyan, A. D. Mashtakov, and E. A. Stepantsov

Institute of Radio Engineering and Electronics, Russian Academy of Sciences, Moscow
(Submitted July 23, 1999)
Pis'ma Zh. Tekh. Fiz. **25**, 65–72 (November 26, 1999)

Dependences of the amplitudes of the harmonic and subharmonic Shapiro steps on an external monochromatic signal were used to study the current–phase dependence of high-temperature superconducting junctions on a bicrystal substrate. It is shown that for a symmetric definition of the transport current across the junction with an edge transparency of the order of $\overline{D}=10^{-4}$ and a mirror-symmetric bicrystal interface, the current–phase dependence is close to sinusoidal which differs from the theoretical predictions and is most likely caused by twinning of the high-temperature superconducting films of the electrodes forming the junction. A departure from symmetry in the definition of the transport current across the junction causes the current–phase dependence to deviate from sinusoidal, which increases with increasing degree of asymmetry. This change in the current–phase dependence is accurately described by a model which takes into account the formation of coupled Andreev states in junctions of superconductors with a $d_{x^2-y^2}$ type of superconducting wave function. © *1999 American Institute of Physics.* [S1063-7850(99)02711-1]

When Josephson junctions are used in superconducting electronic devices, an important parameter is the dependence of the superconducting current I_s on the phase difference φ between the order parameters of the two superconductors forming the Josephson junction (current–phase dependence). This dependence $I_s(\varphi)$ determines the dynamic parameters of the Josephson junction such as the Josephson inductance, the microwave impedance, the spectral composition of the self-induced Josephson generation, and so on. It follows from general quantum-mechanics relationships that for any type of Josephson junction $I_s(\varphi)$ is 2π-periodic and is an odd function of the phase. Calculations of Josephson devices are usually made assuming[1] a sinusoidal current–phase dependence $I_s(\varphi)=I_c\sin\varphi$ (I_c is the critical current of the Josephson junction), which is only observed in tunnel junctions between ordinary *s*-superconductors over a wide range of temperature.[2] However, in Josephson junctions between *s* superconductors with direct conduction a nearly sawtooth dependence $I_s(\varphi)$ is observed at low temperatures, which may be expressed as an expansion in terms of Fourier components

$$I_s(\varphi)=\sum I_c\delta_n\sin(n\varphi),\quad n\geqslant 1, \tag{1}$$

where the even components δ_n are negative, i.e., the phase difference φ_0 for which the maximum of $I_s(\varphi)$ is observed lies in the range $\pi/4\leqslant\varphi_0\leqslant\pi/2$ (Ref. 2). One reason for this complex dependence $I_s(\varphi)$ is that multiple Andreev reflection contributes to the superconducting current, and bound states with energies $\varepsilon<\Delta$ (Δ is the superconductor gap) occur in junctions with direct conduction. The situation is considerably more complex in Josephson junctions consisting of high-temperature superconductors (HTSCs), most of which are assumed to have a $d_{x^2-y^2}$ type of superconducting wave function (*d*-superconductor). A change in the sign of the order parameter on going round the ''c'' axis of a *d*-superconductor (D) leads to the appearance of bound states at the *d*-superconductor–insulator (I) interface, having energies substantially lower than the gap, even in the absence of a second superconductor.[3,4] As a result, at low temperatures $I_s(\varphi)$ only retains its sinusoidal dependence in tunnel junctions between *d*-superconductors (DID) in a narrow range of junction transparencies $\overline{D}$ and angles of misorientation of the crystallographic axes of the HTSC electrodes relative to the normal to the interface α and β. For example, for $\alpha=45°$, $\beta=-45°$ this range is determined by: $\overline{D}\leqslant(2kT/\Delta)^2$ (Refs. 3 and 4). At low temperatures maximum of the dependence $I_s(\varphi)$ deviates from $\sin\varphi$ both in the direction $\pi/4\leqslant\varphi_0\leqslant\pi/2$, and in the direction $(0\leqslant\varphi_0\leqslant\pi/4)$ opposite to that in junctions between *s*-superconductors with direct conduction.[3–5]

The dependence $I_s(\varphi)$ is usually determined from measurements of the amplitude–frequency characteristics of a microwave resonator coupled with an interferometer in which the Josephson junction is shunted by the superconducting inductance L. The main constraint involved in using this method of determining $I_s(\varphi)$ is the magnitude of the critical current which determines the Josephson inductance $L_J=\Phi_0/2\pi I_c$ (where Φ_0 is the magnetic flux quantum). For a reliable determination of $I_s(\varphi)$ the inductance of the interferometer must satisfy the constraint $L<L_J$. For realistic interferometer dimensions of the order of a few tens of micron the critical current I_c should not exceed $10\,\mu$A, which severely restricts the choice of samples. In the present study

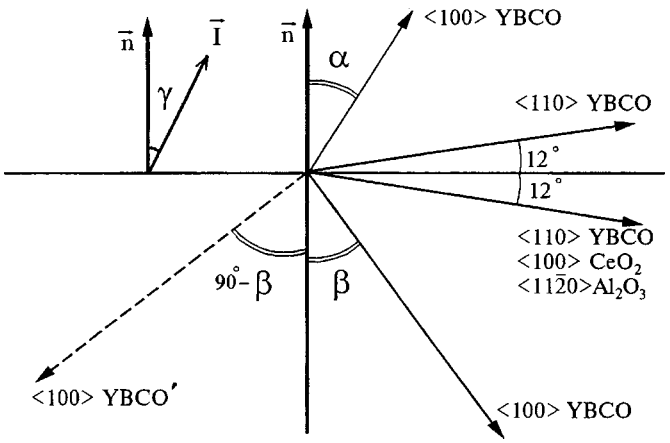

FIG. 1. Configuration of the crystallographic axes of YBCO films relative to the bicrystal interface showing the angles of misorientation of the bicrystal ($\alpha=33°$, $\beta=-33°$). The dashed line shows the orientation of the twin ($\alpha=33°$, $\beta=57°$). The direction of dc current flow is shown in the upper left.

we use a different method of determining $I_s(\varphi)$ based on measuring the critical current and the Shapiro steps as a function of the amplitude of external monochromatic electromagnetic radiation $I_m(A_{\mathrm{RF}})$. Changes in the Shapiro steps were first used to estimate $I_s(\varphi)$ in superconducting thin-film tin bridges[6] and were then applied to HTSC structures in Ref. 7. Here we report measurements of the current–phase dependence of HTSC Josephson junctions on bicrystal sapphire substrates.

The Josephson junctions were fabricated on the $(11\bar{0}2)$ plane of sapphire substrates consisting of two crystals for which the $\langle 11\bar{2}0\rangle$ directions formed an angle of $\pm 12°$ with the plane of the interface (see Fig. 1). The HTSC film was deposited by first depositing an epitaxial CeO_2 buffer layer 30 nm thick by rf magnetron sputtering followed by an epitaxial $YBa_2Cu_3O_x$ (YBCO) film grown by diode sputtering in a dc discharge at high oxygen pressure.[8] Thin-film YBCO bridges 5–10 μm wide and 10–20 μm long, crossing the bicrystal interface, were prepared by liquid chemical etching of YBCO in a 0.5% solution of Br_2 in ethanol. As a result, we obtained YBCO Josephson junctions on a bicrystal substrate for which the [001] directions of YBCO are perpendicular to the plane of the substrate and the $\langle 100\rangle$ directions on either side of the interface form the angle $\alpha=33°$, $\beta=-33°$ with the normal to the interface lying in the plane of the substrate. At liquid helium temperature, we measured the dependences of the Shapiro steps on the millimeter-range microwave current for samples where the YBCO bridge crossed the bicrystal interface at right angles (the angle between the normal to the interface and the direction of the current is $\gamma=0$) and at various fixed values $\gamma=18°$, 36°, 54°, 72° (Fig. 1).

The appearance of Shapiro steps involves the locking of Josephson oscillations with harmonics of the external monochromatic signal. The absence of any harmonics of the self-induced Josephson oscillation in the time dependence of the parameter $(\sin\varphi)^{-1}$ for the final junction voltage having $I_s(\varphi)=I_c\sin\varphi$, has the result that the locking regions of the harmonics of the self-induced oscillation with the external signal are zero (no subharmonic Shapiro steps are observed).[1] In a Josephson junction having a uniform current distribution, these steps appear when $I_s(\varphi)$ deviates from a sinusoidal dependence. It is easy to show that in terms of the resistive model when $\omega=hf_c/2eI_cR_N\geqslant 1$ (where f_c is the frequency of the external signal), the maximum values of the subharmonic Shapiro steps uniquely determine the amplitudes of the harmonic components of $I_s(\varphi)$, δ_n in Eq. (1) so that for $\delta_1=1-\delta_2$, $\delta_n=0$ for $n>2$ we have for the amplitudes of the steps I_m:

$$I_1(a)=\max I_c\{[(1-\delta_2)J_1(a\omega)\sin\theta + \delta_2 J_2(2a/\omega)\sin 2\theta]\},$$
$$I_{1/2}(a)=\max I_c[\,\delta_2 J_1(2a/\omega)\sin 2\theta], \qquad (2)$$

where the maximum is determined from the phase shift θ between the self-induced oscillation and the external signal, J_n are nth order Bessel functions, and $a=A_{\mathrm{RF}}/I_c$ is the normalized amplitude of the external monochromatic signal $A_{\mathrm{RF}}\sin(2\pi f_e t)$.

The results of calculations using the relations (2) for $\delta_2=0$, -0.2, and $\omega>1$ are shown by the solid curves in Fig. 2, which also gives results of experimental investigations of junctions with $\gamma=0$ and 54°. It can be seen that despite the

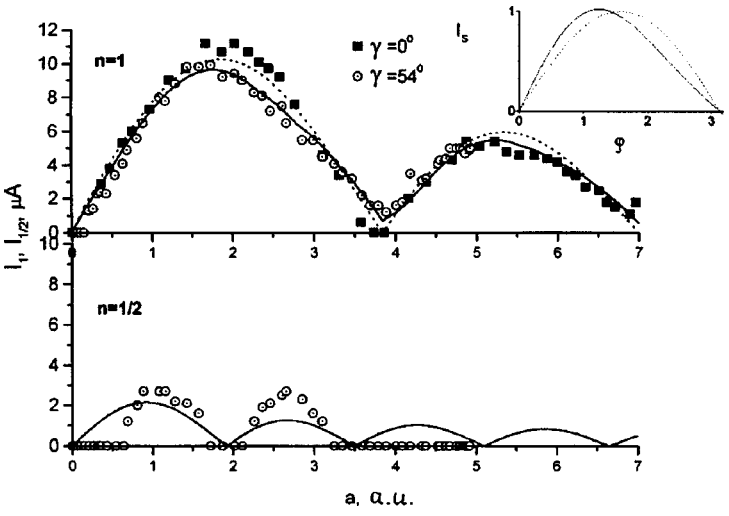

FIG. 2. Dependences of the amplitudes of the first ($n=1$) and subharmonic ($n=1/2$) Shapiro steps on the microwave current. The dashed curves give the calculations using the resistive model $I_s(\varphi)=I_c\sin(\varphi)$ and the solid curves give $I_s(\varphi)=I_c\times(1-\delta_2)\sin(\varphi)-I_c\delta_2\sin(2\varphi)$, $\delta_2=0.2$. The inset shows the change in $I_s(\varphi)$ as δ_2 increases. The solid curve is plotted for $\delta_2=0$, and the dashed curve for $\delta_2=0.2$.

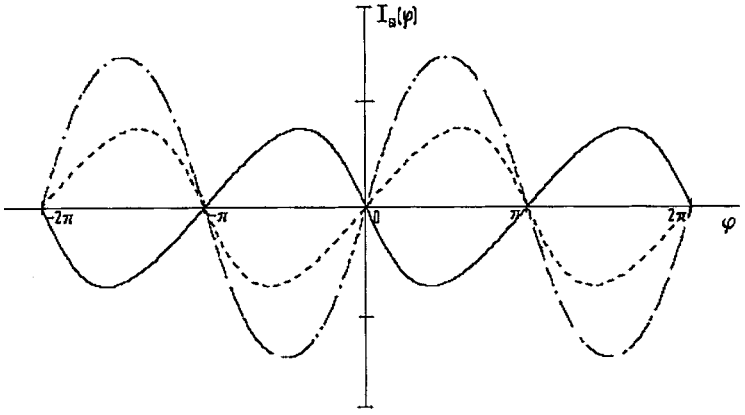

FIG. 3. Theoretical dependences $I_s(\varphi)$ for a mirror-symmetric bicrystal junction $\alpha=-\beta=45°$ (dashed curve) and for a symmetric junction $\alpha=45°$, $\beta=45°$ (solid curve) which for a given angle of misorientation describe a contact with a twin. The dot-dash curve gives the resultant curve.

assumed fairly strong deviation of $I_s(\varphi)$ from sinusoidal (see inset to Fig. 2), the first Shapiro step is close to the case $\delta_2=0$ (dashed curve in Fig. 2). It can be seen that in our case the deviation of $I_s(\varphi)$ from $\sin(\varphi)$ for $\gamma=0$ is less than 5%, which generally occurs in tunnel junctions between *s*-superconductors. However, for Josephson junctions with $\gamma>30°$, a subharmonic Shapiro step is observed whose maximum determines the value of δ_2. Theoretical calculations[3,4] indicate that for the experimental values of the transparency of the tunnel barrier between *d*-superconductors $\overline{D}=10^{-4}$, determined using the value of R_NS, at $T=4.2$ K, and angles of misorientation $\alpha=45°$, $\beta=-45°$, the deviation of $I_s(\varphi)$ should be substantial $\delta_2=0.2$ for $\gamma=0$ (see Fig. 3). A possible reason for the difference between the experiment and the calculations[3,4] may be twinning of the YBCO film. In fact, when twinning is taken into account, the Josephson junction may be considered to be a set of parallel-connected junctions: 1) $\alpha=33°$, $\beta=-33°$; 2) $\alpha=33°$, $\beta=57°$; 3) $\alpha=-57°$, $\beta=-33°$; and 4) $\alpha=-57°$, $\beta=57°$. We calculated $I_s(\varphi)$ for a Josephson junction with $\alpha=45°$, $\beta=-45°$ and $\alpha=45°$, $\beta=45°$ (see Fig. 3) bearing in mind that the Andreev levels do not vary substantially for angles of misorientation between 20° and 45° (Refs. 3 and 4). It can be seen from Fig. 3 that the functions $I_s(\varphi)$ for each of the junctions formed by a twinning complex differ substantially from sinusoidal. However, the total current across two parallel-connected junctions has a nearly sinusoidal dependence $I_s(\varphi)$, as was observed experimentally.

Figure 4 gives the maximum Shapiro subharmonic step as a function of the angle of deviation of the direction of junction current flow from the normal. It can be seen that the deviation of $I_s(\varphi)$ from sinusoidal increases as γ increases. At the same time, the critical current density increases slightly. Assuming that an increase in γ is equivalent to a rotation of the bicrystal interface relative to the YBCO crystallographic axes,[10] the increase in γ is equivalent to a transition from a symmetric bicrystal Josephson junction to an asymmetric one. Moreover, the critical current depends nonmonotonically on the angle of rotation (solid curve in Fig. 4). This nonmonotonicity has been observed experimentally.[10] In our case, only a slight increase in $j_c(\gamma)$ is observed.

To sum up, experimental investigations have shown that the current–phase dependence of symmetric HTSC junctions on a bicrystal substrate is close to sinusoidal and this can probably be attributed to the twinning of the HTSC films of the electrodes forming the junction. This factor and also inhomogeneities of the interface cause the experimental data to differ from the predictions of the model which allows for the appearance of bound Andreev states in superconductor junctions having a $d_{x^2-y^2}$ type of superconducting wave function. A departure from symmetry in the definition of the transport current across the junction leads to a change in the current–phase dependence which increases as the degree of asymmetry increases.

The authors are grateful to P. B. Mozhaev and F. V. Komissinskiĭ for assistance with the experiment, and to A. V. Zaĭtsev, E. Il'ichev, Z. Ivanov, V. Shumeĭko, and A. Kadigrobov for useful discussions.

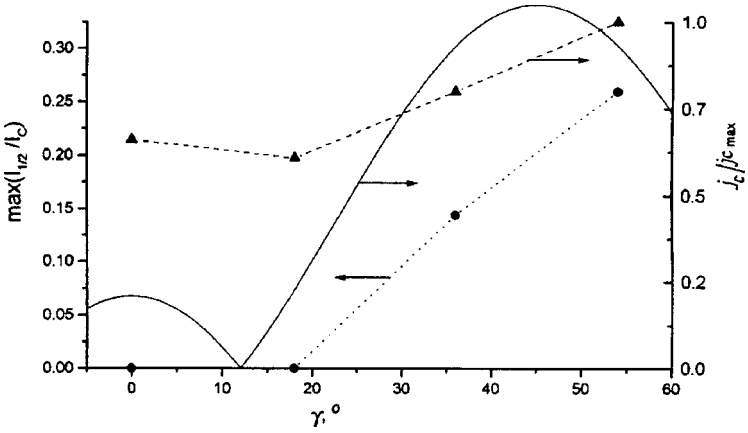

FIG. 4. Dependences of the maximum amplitude of the Shapiro subharmonic step and the critical current density on the angle of deviation of the current direction from the normal. The solid curve gives the critical current of the Josephson junction as a function of the angle of asymmetry of the bicrystal interface obtained using the method described in Ref. 10.

This work was partly financed by the Russian Program ''Topical Problems in Physics of the Condensed State,'' ''Superconductivity'' subprogram, by the Russian Fund for Fundamental Research, and the INTAS Program of the European Union.

[1] K. K. Likharev and B. T. Ul'rikh, *Systems with Josephson Junctions* [in Russian], Moscow State University Press, Moscow (1978), 447 pp.
[2] K. Likharev, Rev. Mod. Phys. **51**, 102 (1979).
[3] Y. Tanaka and S. Kashiwaya, Phys. Rev. B **56**, 892 (1997).
[4] R. A. Riedel and P. E. Bagwell, Phys. Rev. B **57**, 6084 (1998).
[5] E. Il'ichev, V. Zakosarenko, R. P. J. Ijsselsteijn *et al.*, Phys. Rev. Lett. **81**, 894 (1998).
[6] V. N. Gubankov, V. P. Koshelets, and G. A. Ovsyannikov, Zh. Éksp. Teor. Fiz. **71**, 348 (1976) [Sov. Phys. JETP **44**, 181 (1976)].
[7] R. Kleiner, A. S. Katz, A. G. Sun *et al.*, Phys. Rev. Lett. **76**, 2161 (1996).
[8] A. D. Mashtakov, K. I. Konstantinyan, G. A. Ovsyannikov, and E. A. Stepantsov, Pis'ma Zh. Tekh. Fiz. **25**(7), 1 (1999) [Tech. Phys. Lett. **25**, 249 (1999)].
[9] Yu. S. Barash, H. Bukrhardt, and D. Rainer, Phys. Rev. Lett. **77**, 4070 (1996).
[10] Z. G. Ivanov, E. A. Stepantsov, T. Claeson *et al.*, Phys. Rev. B **57**, 602 (1998).

Translated by R. M. Durham

Dispersion of magnetostatic waves in a tangentially magnetized ferrite wafer with normal uniaxial anisotropy

V. I. Zubkov and V. I. Shcheglov

Institute of Radio Engineering and Electronics, Russian Academy of Sciences, Fryazino
(Submitted February 18, 1999)
Pis'ma Zh. Tekh. Fiz. **25**, 73–78 (November 26, 1999)

A dispersion law is obtained and analyzed for the first time for magnetostatic waves in a tangentially magnetized ferrite wafer with uniaxial anisotropy where the axis is perpendicular to the plane of the wafer and the applied static magnetic field is weaker than the anisotropy field. This model qualitatively describes the dispersion of magnetostatic waves in hexa- and orthoferrite wafers and also in an unsaturated ferrite wafer. © *1999 American Institute of Physics.* [S1063-7850(99)02811-6]

Magnetostatic waves (MSWs) in an anisotropic ferrite wafer arbitrarily magnetized to saturation were analyzed in Refs. 1–5. However, these studies either allowed only for cubic anisotropy[1–4] or they took uniaxial anisotropy into account but assumed that it was weak compared with the cubic anisotropy.[5] Recent experiments[6] have shown that uniaxial anisotropy may exceed cubic anisotropy, even in epitaxial yttrium iron garnet films. In hexa- and orthoferrites the uniaxial anisotropy is greater than the saturation magnetization and determines their microwave properties.

In this context, it is relevant to study the dispersion of MSWs in a tangentially magnetized ferrite plate possessing uniaxial anisotropy, whose axis is perpendicular to the plane of the wafer when the magnetizing field H_0 is weaker than the anisotropy field H_A. The results of such an investigation are presented below (neglecting the domain structure, as in Refs. 1–5).

Let us set the yz plane of the coordinate system coincident with the plane of the wafer and with the x axis perpendicular to it. The axis of uniaxial anisotropy is directed along x and the anisotropy field H_A is greater than the saturation magnetization of the wafer $4\pi M_0$. The field H_0 is applied in the plane of the wafer along the z axis and the magnetization vector $\mathbf{M}$ of the ferrite wafer invariably lies in the xz plane. This vector is oriented parallel to the x axis in the field H_0 and as it increases, it turns toward the z axis and lies on this axis when $H_0=H_A$, producing an effective anisotropy field of $H_A=2KM_0-4\pi M_0$, i.e., the difference between the uniaxial anisotropy field and the degaussing field of the ferrite wafer. A second-order phase transition takes place at the field $H_0=H_A$ after which the magnetization vector $\mathbf{M}$ is invariably directed along the z axis. Magnetostatic waves propagate in the plane of the wafer. The angle between the wave vector $\mathbf{k}$ of these waves and the y axis will be denoted by φ.

The dispersion relation for the MSWs, obtained by standard methods,[7,8] has the form

$$\beta-2\mu_H\alpha\coth(\alpha kd)=0, \tag{1}$$

where $\alpha=\{(\mu_A\mu_H^{-1})[(1-\mu_P\mu_A\mu_H^{-1})\sin^2\varphi+\cos^2\varphi]\}^{1/2}$, $\beta=(\nu_H^2-\mu_P^2)\cos^2\varphi-\mu_H\mu_A+\mu_P^2-1$, $\mu_H=1+\Omega_H^2\Lambda^{-1}$, $\mu_A=1+(\Omega_A^2-\Omega_H^2)\Lambda^{-1}$, $\mu_P=-\Omega_H(\Omega_A^2-\Omega_H^2)^{1/2}\Lambda^{-1}$, $\nu_H=\Omega\Omega_H\Lambda^{-1}$, $\Lambda=\Omega_A[(\Omega_A^2-\Omega_H^2)-\Omega^2]$, $\Omega=\omega(4\pi\gamma M_0)^{-1}$, $\Omega_H=H_0(4\pi M_0)^{-1}$, $\Omega_A=H_A(4\pi M_0)^{-1}$, ω is the frequency, γ is the modulus of the electron gyromagnetic ratio, and k is the wave number.

It can be seen from Eq. (1) that the nature of the solution is determined by the form of the parameter α, and that two types of MSWs are possible. As for the MSWs in an isotropic ferrite wafer,[7,8] when α is imaginary, the waves are volume MSWs and when α is real, they are surface waves. These waves are subsequently called anisotropic MSWs (anisotropic, anisotropic volume, and anisotropic surface MSWs). Their wavefront is not perpendicular to the plane of the ferrite wafer as in Refs. 7 and 8 but is more strongly inclined to this plane, the closer is H_0 to H_A. Unlike in Refs. 7 and 8, the distribution of the rf magnetization over the thickness of the wafer is not a standing but a traveling one and is described by a periodic function, either with constant amplitude (anisotropic volume MSWs) or whose amplitude has a maximum at the surfaces of the ferrite wafer and decays exponentially inside the wafer (anisotropic surface MSWs). Anisotropic volume MSWs are multimode while the surface MSWs are single-mode. When $\varphi=0°$ the anisotropic MSWs degenerate into surface and volume MSWs as described in Refs. 7 and 8.

Anisotropic MSWs exist in given frequency–field regions, in frequency ranges [between $\Omega(0)$ and $\Omega(\infty)$] and in ranges of wave numbers k (between 0 and ∞) determined by Eq. (1) and by the characteristics of the components of the magnetic permeability tensor ν_H, μ_P, μ_H, and μ_A (zeros, ∞, limits) appearing in this equation.

Figure 1 shows the limits of the frequency–field regions for anisotropic MSWs propagating an angles $\varphi=0°$ (a) and $\varphi=90°$ (b) for $4\pi M_0=1750$ Gs and $H_A=3.5$ kOe.

For MSWs with $\varphi=0°$ curve *1* is described by

$$\Omega(0)=\{[\Omega_A(\Omega_A^2-\Omega_H^2)+\Omega_H^2]\Omega_A^{-1}\}^{1/2}, \tag{2}$$

and volume and surfaces MSWs with this frequency have $k=0$.

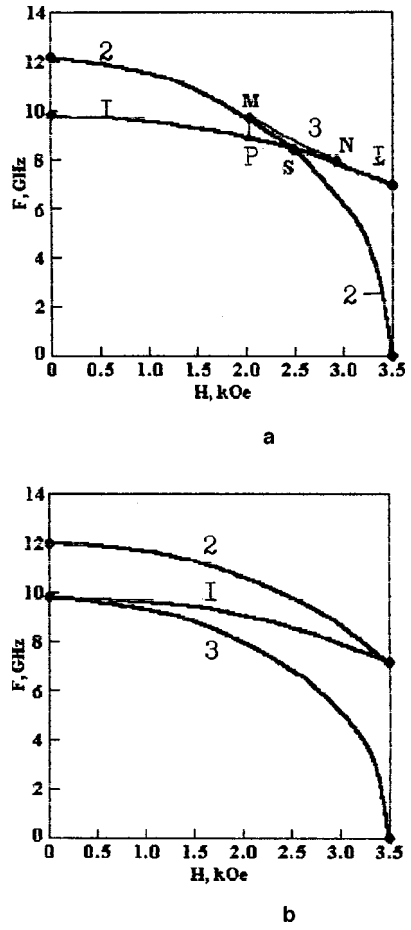

FIG. 1. Limiting frequencies of spectrum as a function of the field when waves propagate (a) perpendicular to the field H_0 ($\varphi=0°$) and (b) parallel to the field H_0 ($\varphi=90°$).

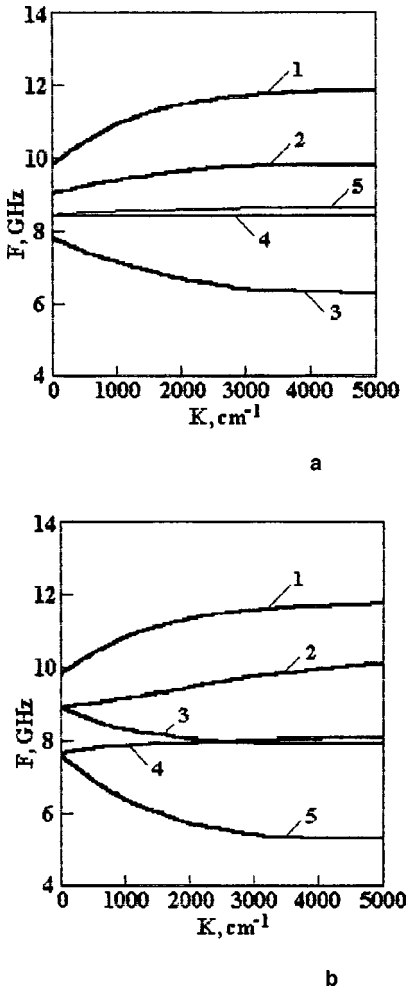

FIG. 2. Dispersion curves for waves propagating (a) perpendicular to the field H_0 ($\varphi=0°$) and (b) parallel to the field H_0 ($\varphi=90°$) for various fields: (a): *1*—$H_0=0$ Oe, *2*—2 kOe, *3*—3 kOe, *4* and *5*—2.474 kOe; (b): *1*—$H_0=0$ Oe, *2* and *3*—2 kOe, *4* and *5*—3 kOe.

Curve *2* is described by

$$\Omega_v(\infty)=[(\Omega_A^2-\Omega_H^2)(\Omega_A+1)\Omega_A^{-1}]^{1/2}, \tag{3}$$

and volume MSWs with this frequency have $k=\infty$.

Curve *3* only exists in the section MN and is described by the formula

$$\Omega_S(\infty)=(\Omega_A^3+\Omega_H^2)(2\Omega_A\Omega_H)^{-1}, \tag{4}$$

and surface MSWs with this frequency have $k=\infty$.

Curves *1* and *2* intersect at point *S*. The corresponding field H_0 will subsequently be called critical and will be denoted by H_S ($H_S=2474$ Oe in Fig. 1a). Points *M* and *N* are the points of contact of curves *1* and *2* with curve *3*. Between curves *1* and *2* volume MSWs exist (in the field $H_0<H_S$ these are forward waves and for $H_0>H_S$ they are return waves). In the region bounded by the curvilinear triangle MPN, a forward MSW exists whose spectrum in the triangle MPS overlaps with that of the surface MSW which also occurs for MSWs in a ferrite wafer exhibiting cubic anisotropy.[3–5]

For $\varphi=90°$ only anisotropic volume MSWs exist (Fig. 1b). Curve *1* is described by formula (2). Curves *2* and *3* are respectively described by:

$$\Omega_{v,1}(\infty)=[(\Omega_A^2-\Omega_H^2)+\Omega_A]^{1/2}, \tag{5}$$

$$\Omega_{v,2}(\infty)=(\Omega_A^2-\Omega_H^2)^{1/2}, \tag{6}$$

for anisotropic volume MSWS at these frequencies we have $k=\infty$.

The anisotropic volume MSWs between curves *1* and *2* are forward waves and those between curves *1* and *3* are return waves.

Figure 2 shows dispersion curves of MSWs with $\varphi=0°$ (a) and $\varphi=90°$ (b) for various fields H_0 for ferrite wafers 15 μm thick.

In Fig. 2a curves *1–4* describe the first mode of a volume MSW and curve *5* describes a surface MSW. Curve *1* corresponds to the field $H_0=0$ Oe and describes the dispersion of forward volume MSWs similar to those in an isotropic ferrite wafer under normal magnetization.[7,8] Curve *2* corresponds to the field $H_0<H_S$, it curves upward, and describes forward waves in the region between curves *1* and *2* (Fig. 1a). Curve *3* corresponds to the field $H_0>H_S$, it curves downward, and describes return waves in the region between curves *1* and *2* (in Fig. 1a). Curve *4* corresponds to the field $H_0=H_S$ and describes volume MSWs for which the frequency range of existence degenerates into a point and the

dispersion curve degenerates into a horizontal straight line. Curve *5* also corresponds to the field $H_0=H_S$ but describes a forward surface MSW for which the frequency range of existence is finite.

Figure 2b describes the first mode of an anisotropic volume MSW. Curve *1* is the same as curve *1* in Fig. 2a. Curves *2* and *3* correspond to the field $H_0=2$ kOe. Curve *2* curves upward and describes a forward wave in the region between curves *1* and *2* in Fig. 1b. Curve *3* curves downward and describes a return wave between curves *1* and *3* in Fig. 1b. Curves *4* and *5* correspond to the field $H_0=3$ kOe. Their frequencies are lower than those for $\varphi=0°$, since the magnetization vector **M** is more inclined to the direction of H_0. In other respects these curves are similar to curves *2* and *3*.

These results qualitatively explain the spectrum, dispersion, and excitation characteristics of MSWs in a ferrite wafer possessing normal uniaxial anisotropy under tangential magnetization in the presence of a domain structure.[6] Anisotropic MSWs have not yet been observed in hexa- and orthoferrites and no comparisons can be made with these.

This work was supported by the RFBR (Grant No. 96-02-17283a).

[1] A. S. Beregov, Izv. Vyssh. Uchebn. Zaved. Radioélektron. **27**(10), 9 (1984).
[2] O. A. Chivileva, A. G. Gurevich, and L. M. Émiryan, Fiz. Tverd. Tela (Leningrad) **29**(1), 110 (1987) [Sov. Phys. Solid State **29**, 61, (1987)].
[3] I. V. Zavislyak, V. M. Talaevskiĭ, and L. V. Chevnyuk, Fiz. Tverd. Tela (Leningrad) **31**, 319 (1989) [Sov. Phys. Solid State **31**, 906 (1989)].
[4] G. M. Dudko, G. T. Kazakov, A. G. Sukharev, Yu. A. Filimonov, and I. V. Shein, Radiotekh. Élektron. (Moscow) **35**, 960 (1990).
[5] P. E. Zil'berman, V. M. Kulikov, V. V. Tikhonov, and I. V. Shein, Radiotekh. Élektron. (Moscow) **35**, 966 (1990).
[6] A. V. Vashkovskiĭ, É. G. Lokk, and V. I. Shcheglov, Zh. Éksp. Teor. Fiz. **111**, 1016 (1997) [JETP **84**, 560 (1997)].
[7] R. W. Damon and J. R. Eshbach, J. Phys. Chem. Solids **19**, 308 (1961).
[8] A. V. Vashkovskiĭ, V. S. Stal'makhov, and Yu. P. Sharaevskiĭ, *Magnetostatic Waves in Microwave Electronics* (Saratov State University Press, Saratov, 1993), 316 pp.

Translated by R. M. Durham

Exact solution for the steady-state surface profile of a liquid metal in an external electric field

N. M. Zubarev

Institute of Electrophysics, Urals Branch of the Russian Academy of Sciences, Ekaterinburg
(Submitted July 13, 1999)
Pis'ma Zh. Tekh. Fiz. **25**, 79–83 (November 26, 1999)

An analysis is made of the equilibrium profile of the free surface of a liquid metal in an external electric field neglecting gravitational forces. It is shown that a conformal mapping method can be used to find a wide range of exact solutions corresponding to the case of planar symmetry.
 [S1063-7850(99)02911-0]

The problem of the steady-state profile of the free surface of a liquid metal in an external electric field plays an important role in understanding the main laws governing the evolution of electrohydrodynamic instability.[1,2] A considerable number of studies (see, for example, Refs. 3 and 4) have solved a similar problem using the approximation of small surface perturbations (a liquid of finite permittivity is usually considered; the case of a liquid metal corresponds to the limit $\varepsilon \to \infty$). We shall show that in the two-dimensional case when all the quantities depend on the pair of independent variables x and y, using a conformal mapping method can remove this constraint.

Let us assume that the vector of the external field E_0 is directed along the y axis. The distribution of the electric field potential φ (the field strength is given by $\mathbf{E}=-\nabla\varphi$) above the surface S of the liquid metal is described by the Laplace equation:

$$\varphi_{xx}+\varphi_{yy}=0,$$

which should be supplemented by the equipotential condition at the conductor boundary $\varphi|_S=0$, and also by the condition for uniformity of the field at infinity:

$$\varphi \to -E_0 y, \quad y \to \infty. \tag{1}$$

Note that for the radius of curvature of the equipotential surface we have $R^{-1}=-\partial E/\partial\varphi$, where $E=|\mathbf{E}|$ is the absolute value of the field strength. Then, neglecting the gravitational field, the force balance condition[5] is written in the form:

$$p+\left|\frac{E^2}{8\pi}\right|_S=\alpha\left|\frac{\partial E}{\partial\varphi}\right|_S, \tag{2}$$

where α is the surface tension, and p is the difference between the liquid pressure and the external pressure which we assume to be equal to the unperturbed electrostatic pressure: $p=-E_0^2/(8\pi)$.

We take E_0 as the unit of electric field strength and $8\pi\alpha E_0^{-2}$ as the unit of length. We then introduce the auxiliary function ψ which is harmonically conjugate with the potential φ (the curves $\psi=\text{const}$ define the field lines). The expression $w=\varphi-i\psi$ (the so-called complex potential) is an analytic function of the complex variable $z=x+iy$ (Ref. 5). In this case $f-i\theta\equiv\ln(-dw/dz)$ will also be an analytic function. The value of θ has the meaning of the slope of the electric field strength vector with respect to the abscissa and the value of f is related to the absolute value of the field by $f=\ln E$. Using the properties of analytic functions, in terms of coordinates where φ and ψ will play the role of independent variables, we obtain for $\varphi<0$:

$$f_{\varphi\varphi}+f_{\psi\psi}=0. \tag{3}$$

The boundary conditions for the function f can easily be determined from Eqs. (1) and (2):

$$\partial f/\partial\varphi=-e^{-f}+e^{f}, \quad \varphi=0, \tag{4}$$

$$f\to 0, \quad \varphi\to-\infty. \tag{5}$$

That is to say, the problem of finding the steady-state surface profile of a liquid metal in an external electric field allowing for capillary forces reduces to an analysis of the nonlinear boundary-value problem (3)–(5) on the half-plane.

It should be noted that apart from the coefficients, the system (3)–(5) agrees with that obtained in Ref. 6 to solve the problem of the steady-state profile of a progressive capillary wave. The analogy arises because, from the mathematical point of view, the equations describing the two-dimensional electric field distribution in the absence of space charge are identical to the equations for the two-dimensional potential flow of an ideal liquid.

By analogy with Ref. 6, we shall seek a solution in the form:

$$f(\varphi,\psi)=\ln\left(\frac{Z(\varphi)+Y(\psi)}{Z(\varphi)-Y(\psi)}\right), \tag{6}$$

where Y and Z are unknown functions of the variables ψ and φ, respectively. Substituting this expression into Eqs. (3)–(5), we observe that the following relations should be satisfied:

$$Z(\varphi)=(k/2+1)e^{-k\varphi}+(k/2-1)e^{k\varphi},$$

$$Y(\psi)=\sqrt{k^2-4}\cos(k\psi),$$

in conjunction with Eq. (6), which are exact solutions of this boundary-value problem.

We then require the dependences of the functions E and θ on the variable ψ at the surface of the conductor. Substituting the expressions for Z and Y into Eq. (6) and bearing in mind that $E=\exp f$, we find that the absolute value of the electric field strength is given by:

$$E|_{\varphi=0}=\frac{1+c(k)\cos(k\psi)}{1-c(k)\cos(k\psi)}, \tag{7}$$

where we have introduced the notation $c(k)=\sqrt{1-4/k^2}$. For the angle $\theta|_{\varphi=0}$, using the Cauchy–Riemann condition $\partial\theta/\partial\psi=\partial f/\partial\varphi$, we obtain from Eq. (4) by integrating over ψ:

$$\theta|_{\varphi=0}=\frac{\pi}{2}+2\arctan\left(\frac{kc(k)}{2}\sin(k\psi)\right). \tag{8}$$

We shall now construct equilibrium profiles of the free surface of the liquid metal using the coordinates $\{x,y\}$. Changing from the variables φ and ψ to the variables x and y is accomplished by means of the transformation: $z=-\int\exp(-f+i\theta)dw$. Then substituting expressions (7) and (8), separating the real part from the imaginary, and bearing in mind that at the boundary $w=-i\psi$, we finally obtain:

$$y=1-c(k)-\frac{4k^{-2}}{1+c(k)\cos(k\psi)}, \tag{9}$$

$$x=\frac{\pi}{k}-\psi+\frac{2c(k)k^{-1}\sin(k\psi)}{1+c(k)\cos(k\psi)}, \tag{10}$$

where $k\geqslant 2$. Thus, we have obtained parametric equations for the equilibrium surface S. It can be seen that the wavelength is given by $\lambda=2\pi/k$ so that the parameter k plays the role of the wave number.

Expressions (9) and (10) can be used to find the amplitude of the perturbation of the liquid metal surface, defined as the difference between the maximum and minimum values of y per period, as a function of the wave number: $A(k)=2\sqrt{1-4/k^2}$. As k increases, the amplitude increases monotonically, reaching a maximum for $k=k_c\approx 3.042$, when the region occupied by the liquid becomes multiply connected, i.e., isolated liquid-metal droplets form, connected to the main bulk of the metal by infinitely thin constrictions. The equilibrium surface corresponding to the critical value of the wave number $k=k_c$ is shown in Fig. 1; also plotted is the family of equipotential surfaces, which gives some idea of the electric field distribution above the liquid metal boundary. To conclude, we note that for the configuration of conducting liquid shown in the figure the ratio of the amplitude of the surface perturbation to the wavelength is 0.73 and the electric field at the tip is almost an order of magnitude, 7.1 times, higher than the external field.

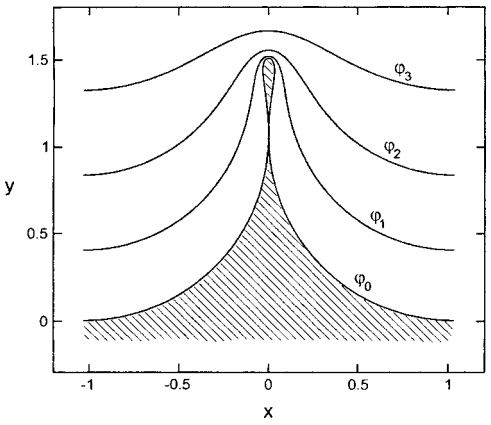

FIG. 1. Single period of the steady-state profile of the free surface of a liquid metal in an external electric field for the critical wave number $k=k_c\approx 3.042$. Equipotential surfaces corresponding to different values of the parameter φ are shown ($\varphi_1=-0.07$, $\varphi_2=-0.19$, and $\varphi_3=-0.42$); at the liquid metal boundary $\varphi=\varphi_0=0$.

The author is grateful to E. A. Kuznetsov for kindly drawing attention to Ref. 6 and also to A. M. Iskol'dskiĭ and N. B. Volkov for fruitful discussions.

This work was supported financially by the RFBR, Project No. 97-02-16177.

[1] L. Tonks, Phys. Rev. **48**, 562 (1935).
[2] Ya. I. Frenkel', Zh. Tekh. Fiz. **6**, 347 (1936).
[3] M. I. Shliomis, Usp. Fiz. Nauk. **112**, 427 (1974) [Sov. Phys. Usp. **17**, 153 (1974)].
[4] E. A. Kuznetsov and M. D. Spektor, Zh. Éksp. Teor. Fiz. **71**, 262 (1976) [Sov. Phys. JETP **44**, 136 (1976)].
[5] L. D. Landau and E. M. Lifshitz, *Electrodynamics of Continuous Media*, 2nd ed. (Pergamon Press, Oxford, 1984; Nauka, Moscow, 1982).
[6] G. D. Crapper, J. Fluid Mech. **2**, 532 (1957).

Translated by R. M. Durham

Long-lived explosive-emission cathode for high-power microwave radiation generators

A. V. Gunin, V. F. Landl', S. D. Korovin, G. A. Mesyats, and V. V. Rostov

Institute of High-Current Electronics, Siberian Branch of the Russian Academy of Sciences, Tomsk
Institute of Electrophysics, Urals Branch of the Russian Academy of Sciences, Ekaterinburg
(Submitted July 28, 1999)
Pis'ma Zh. Tekh. Fiz. **25**, 84–94 (November 26, 1999)

The operation of cold explosive-emission cathodes having a current density of $\sim 10^4$ A/cm^2, fabricated using various materials, was investigated under a large number of switching cycles. The cathode voltage was ~ 500 kV, the maximum current ~ 5 kA, and the pulse duration ~ 20 ns. It is shown that when the number of switchings is small ($\leqslant 10^3$ pulses), cathodes having similar geometry exhibit similar emission properties. For most of the materials studied, as the number of switching cycles increases ($\geqslant 10^3$ pulses), the current rise time increases (as far as the pulse duration) and the maximum vacuum diode current decreases. When a graphite cathode was used, the maximum current remained unchanged up to 10^8 switching cycles. The mass removed from the cathode was determined for various materials. The results were used to achieve continuous operation of a relativistic 3 cm backward-wave tube having an output power of 350–400 MW and an almost constant power level during 10^8 pulses at a repetition frequency of 100–150 Hz. © *1999 American Institute of Physics.* [S1063-7850(99)03011-6]

INTRODUCTION

One of the main problems encountered when using high-current pulse-periodic accelerators is the development of long-lived, explosive-emission cold cathodes. Experiments have shown that in most cases, the emission properties of cold cathodes depend on the total number of pulses[1] and as the number of pulses increases, the current rise time increases, the maximum electron beam current decreases, and its spatial homogeneity deteriorates.[2] When the emission surface of the cathode is a set of separately operating emitters, the total diode current begins to depend on the number and dimensions (expansion velocity) of the emission centers.[3] In Ref. 4, Bykov *et al.* proposed a cathode for planar vacuum diodes having a current density of 10–100 A/cm^2 in which the emission surface is the surface of a metal–dielectric contact, described as a metal–dielectric cathode. In this cathode the voltage threshold at which the emission surface can form is lower than that of cathodes made of homogeneous materials, and solves the problem of achieving constant conditions for the appearance of emission centers in the presence of erosion of the metal and the dielectric. Studies have shown that a metal–dielectric cathode having an emission surface area of ~ 200 cm^2 has a lifetime of more than 10^8 pulses at ~ 500 kV, ~ 5 kA, and ~ 20 ns pulse duration.

Coaxial vacuum diodes with an external magnetic field (Fig. 1) usually use sharp-edged cold explosive-emission cathodes, which can produce tubular electron beams having a current density of $\sim 10^4$ A/cm^2. These beams are usually used in relativistic microwave generators to obtain high-power microwave radiation. Edge cathodes in the form of hollow cylinders can achieve fairly high electric fields at their surface, which may exceed 10^6 V/cm at a cathode voltage of ~ 500 kV. This suggests that these cathodes may conserve their emission properties over a fairly large number of pulses. However, as a result of the high current density, sharp-edged, explosive-emission cathodes are more strongly influenced by erosion processes compared with cathodes in planar vacuum diodes.[1,2] The aim of the present study was to make an experimental investigation of changes in the emission properties of cathodes in a coaxial vacuum diode over a

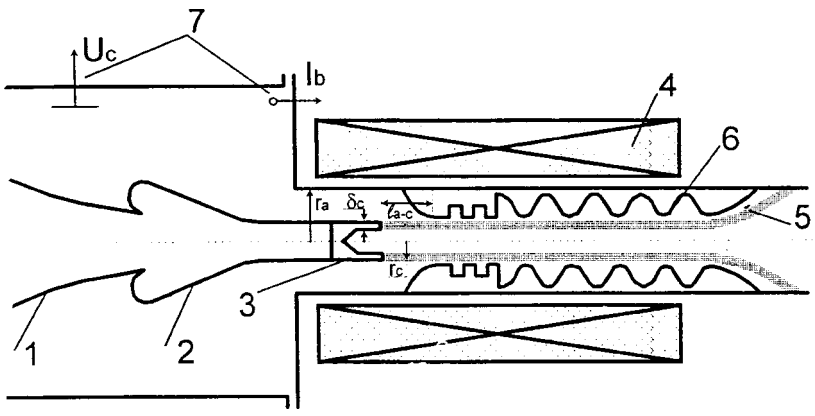

FIG. 1. Coaxial diode with tubular electron beam: *1* — insulator, *2* — cathode holder, *3* — cathode, *4* — solenoid, *5* — electron beam, *6* — backward-wave tube structure, and *7* — cathode voltage and diode current detectors.

large number of current pulses, to determine the mass removed from the cathode, and to search for materials to fabricate cathodes having a lifetime longer than 10^8 current pulses.

EXPERIMENTAL SETUP AND METHOD OF MEASUREMENT

The experiments were carried out using SINUS-500 which is a modified version of SINUS-6 (Ref. 5) and comprises a high-power, nanosecond microwave generator based on a relativistic backward-wave tube having a high pulse repetition frequency. A tubular electron beam was formed in a longitudinal magnetic field having an induction of ~ 0.6 T which was generated by a permanent cooled solenoid having a power consumption of ~ 20 kW. The beam was transported through the electrodynamic structure of the backward-wave tube[6] and deposited on a cooled collector. The cathode voltage was ≈ 500 kV, the beam current ≈ 5 kA, and the pulse duration ≈ 20 ns. The microwave radiation had an output power of 350–400 MW, a wavelength of ~ 3 cm, and a pulse duration of 6–11 ns. The pulse repetition frequency was 100–150 Hz. In all the experiments the incident-wave amplitude of the diode voltage was kept constant by maintaining a constant level of actuating voltage at the controlled spark gap in the accelerator.

For the experiments we used cathodes made of various materials: stainless steel ($\rho = 8.1$ g/cm^3), copper ($\rho = 8.93$ g/cm^3), magnesium ($\rho = 1.74$ g/cm^3), and pyrolytic graphite ($\rho = 1.88$ g/cm^3), as well as composites of various materials such as copper–graphite and copper–dielectric. The cathodes were fabricated as hollow cylinders ≈ 35 mm in diameter having wall thicknesses between 0.2 and 2 mm. A copper–graphite cathode having a total wall thickness of ≈ 0.4 mm was fabricated by close fitting of a graphite ring into a copper one and the copper–dielectric cathode was made of double-sided foil-covered glass Textolite, 0.2 mm thick.

The measurements were made using a TDS-754C oscilloscope (500 MHz, 2 G/s) which recorded pulse traces of the cathode voltage, the vacuum diode current, and the microwave output power. The voltage detector was a capacitive divider, the current was recorded using a Rogowski loop, and the microwave power was recorded using a calibrated detector based on a 6D16D vacuum diode. The emission properties of the cathodes were determined from the maximum current over the pulse duration and the time taken for the current to rise to 4 kA (Fig. 2). The consumption of the cathode material as a result of erosion of the emission surface was determined from the total reduction in the cathode mass after 10^6 current pulses had passed through it. The charge passing through the cathode was calculated by integrating the current pulse (Fig. 2b) between 0 and 80 ns, and was found to be $\approx 160\ \mu$C/pulse. The error in determining the charge given by the displacement current of the vacuum diode (Fig. 2c) did not exceed 10%.

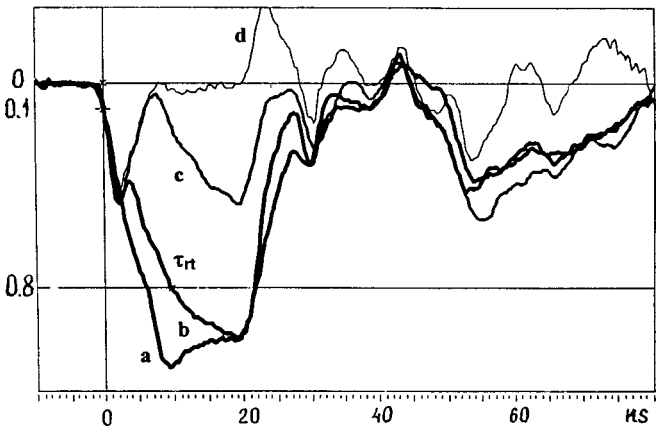

FIG. 2. Oscilloscope traces of pulses: a — voltage, b — current, c — diode current when emission has terminated, and d — reactive diode current (without electron beam).

EXPERIMENTAL RESULTS AND DISCUSSION

Figure 3 gives the current rise time for cathodes having approximately the same wall thickness fabricated using different materials, plotted as a function of the number of pulses. Figure 4 gives the maximum vacuum diode current as a function of the number of pulses for the same cathodes. It

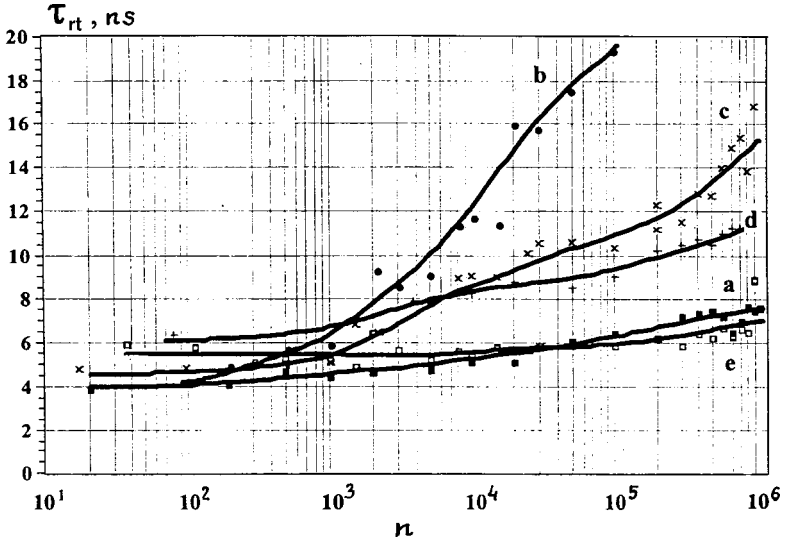

FIG. 3. Variation of current rise time to 4 kA level: a — graphite 0.3 mm, b — stainless steel 0.1 mm, c — copper 0.2 mm, d — magnesium 0.2 mm, and e — copper–dielectric 0.2 mm.

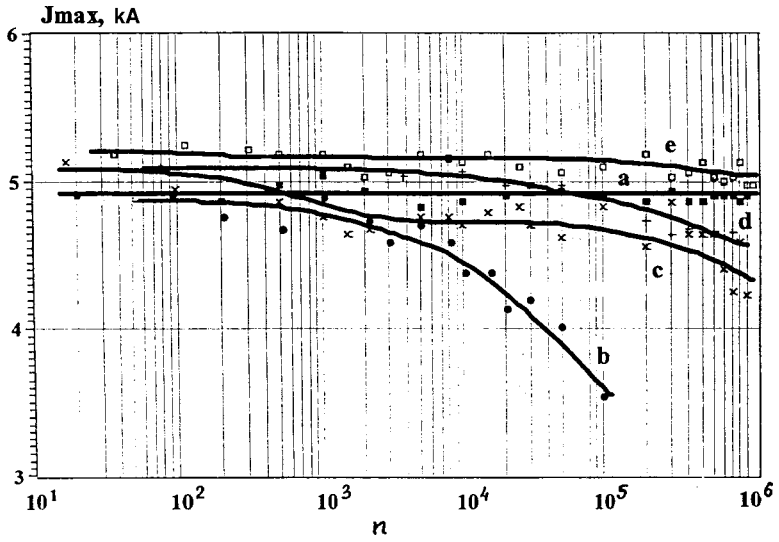

FIG. 4. Variation of current amplitude: a — graphite 0.3 mm, b — stainless steel 0.1 mm, c — copper 0.2 mm, d — magnesium 0.2 mm, and e — copper–dielectric 0.2 mm.

can be seen that for a small number of pulses ($N \leqslant 10^3$), both the current rise time and the maximum vacuum diode current are almost independent of the cathode material. This can evidently be attributed to the existence of various dielectric inclusions, and also adsorbed gas on the cathode surface which lowers the critical electric fields at which plasma emission centers may form. In this case, the electrophysical properties of the cathode material have little influence on the processes of formation of the cathode emission surface.

As the number of pulses increases, the surface of the cathode becomes cleaned of foreign inclusions and adsorbed gas. For $N \geqslant 10^3$ pulses the individual properties of the cathode material begin to appear under these experimental conditions. For most of the cathodes studied, an increase in the number of pulses leads to an increase in the current rise time up to the duration of the voltage pulse, and consequently reduces the maximum vacuum diode current. Experiments carried out using cathodes having different wall thickness δ_c, show that as δ_c increases, the current rise time and the maximum beam current vary more rapidly as a function of the number of pulses. For pure metals, the most probable mechanism for the formation of emission centers is the explosions of microtips as a result of their rapid heating by the field emission current.[1] When these microtips explode, they disintegrate. However, microtips may be created as a result of the expulsion of liquid metal from the emission zone under the action of high pressures.[7] An increase in the current rise time of the vacuum diode indicates that the number of emission centers decreases as the number of pulses increases. In particular, for a stainless steel cathode we observed complete termination of the emission after 10^4–10^5 pulses. In this case, the profiles of the current pulses were similar to the reactive current profile of the diode (Fig. 2d). Hence, a deterioration in the emission properties of the cathodes may be caused by changes in the microrelief and cleaning of the cathode surface by the current flow.

Results of experiments to measure the consumption of cathode material are presented in Table I. Also given are data on the removal of material obtained by other authors[8–11] in various experiments.

A comparison of these data shows that the specific mass consumptions depends on the current flow regime (pulsed[8] or quasiconstant[9–11]). Nevertheless, we can postulate that in both cases, the main factor responsible for the removal of cathode material is evaporation accompanying heating of the cathode material near the emitting cathode spot. The droplet fraction of the cathode erosion is clearly small in our case, which does not contradict the results presented in Ref. 12.

It has been noted that for all the cathodes studied, the emission properties deteriorated as the number of pulses increased. This was manifest particularly in an increase in the current rise time (τ_{rt}) which indicates that the number of emission centers decreases as the number of pulses increases. Stabilization of τ_{rt} was only observed for graphite and copper–dielectric cathodes. However, the latter exhibits an anomalously high consumption of material, apparently caused by intense evaporation of the dielectric.

A pyrolytic graphite cathode 34.8 mm in diameter hav-

TABLE I.

Material	Average consumption 10^{-9} g/pulse	Bulk consumption 10^{-6} cm^3/C	Mass consumption 10^{-6} g/C	Mass consumption, 10^{-6} g/C			
				Ref. 8	Ref. 9	Ref. 10	Ref. 11
Copper	9.1	6.7	60	12	130	115	40
Magnesium	4.13	14.4	25	–	36	–	25
Graphite	5.58	18.1	34	142	–	170	–
Copper–graphite	10.1	–	63	–	–	–	–
Copper–dielectric	27	–	170	–	–	–	–

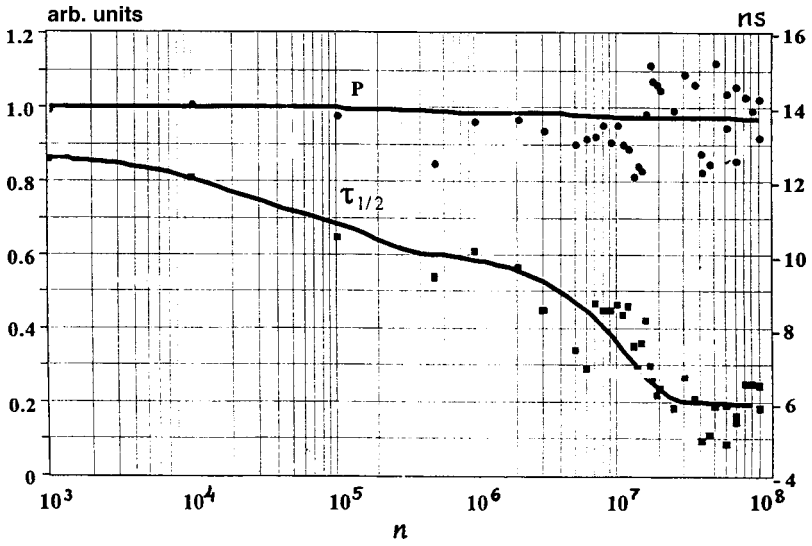

FIG. 5. Variation in output parameters of microwave generator.

ing an edge thickness of 0.3 mm was tested after 10^8 switching cycles. The initial distance L_{a-c} was selected so that the postulated reduction in its length as a result of erosion ($\sim$9 mm) had no appreciable influence on the impedance of the coaxial vacuum diode. This made it possible for a relativistic backward-wave tube to operate over the entire experiment (10^8 switching cycles). Figure 5 shows the relative change in the power and half-height duration of the microwave pulses. The radiation power fell by no more than 10%. The duration of the microwave pulses showed a larger variation, decreasing from 11 to 6 ns. The change in the pulse duration was accompanied by an increase in the current rise time of the vacuum diode. A decrease in the duration of the microwave pulses was accompanied by an increase in their instability from one pulse to another. This indirectly indicates some deterioration in the quality of the electron beam caused by a reduction in the number of emission centers.

The current rise time for the graphite cathode varied rapidly over the first 10^6 pulses but after 5×10^6 pulses, it reached $\sim$8.5 ns and remained constant (Fig. 6). Data on the bulk consumption of graphite (Table I) show that this number of pulses corresponds to a change in the cathode length by a value of the order of its wall thickness $\delta_c=0.3$ mm. This suggests that over the first $(3–5)\times10^6$ pulses the profile of the cathode edge changes which equalizes the electric field distribution at its surface, and thus the cathode operation becomes steady-state.

CONCLUSIONS

These experiments have shown that for a small number of current pulses (10^3–10^4) the emission properties of the cathodes are mainly determined by the initial state of the surface layer and are almost independent of the cathode material. For a particular choice of geometric parameters of the coaxial vacuum diode, graphite cathodes can have a lifetime of more than 10^8 switching cycles (Fig. 7). Under these experimental conditions, processes leading to changes in the parameters of the electron beam caused by changes in the emissivity of the graphite cathode terminate after $\sim5\times10^6$ pulses. These processes are associated with the formation of an edge profile of the emitting cathode which corresponds to

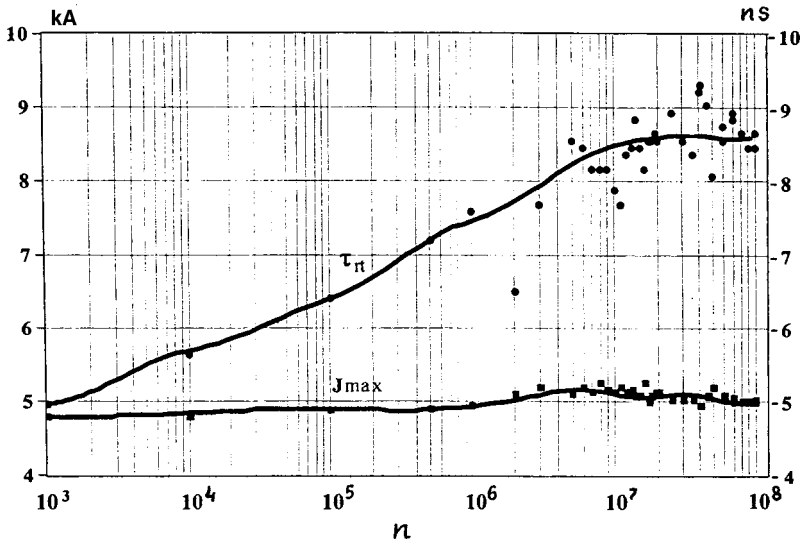

FIG. 6. Current amplitude and rise time for graphite cathode.

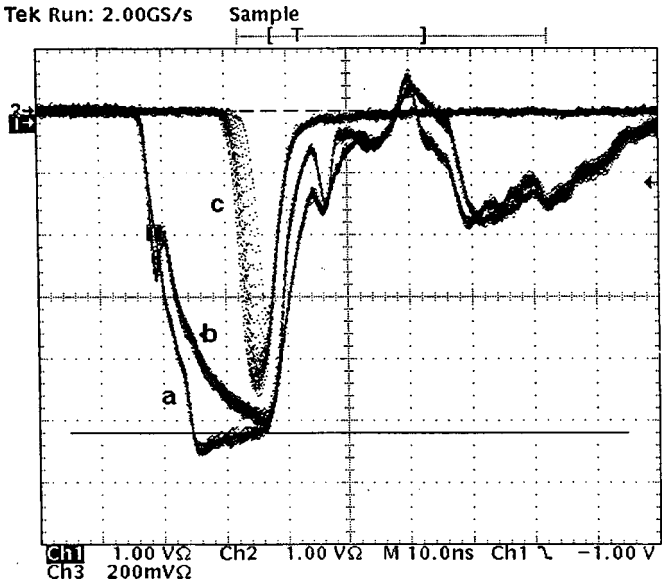

FIG. 7. Typical oscilloscope traces after 10^8 pulses: a — cathode voltage, b — diode current, and c — microwave radiation.

the minimum electric field at its surface. The quality of the electron beam does not change substantially and it can be used to obtain high-power microwave radiation in relatively low magnetic fields.

This work was supported financially by GEC Marconi Research Center, Chelmsford, UK.

[1] G. A. Mesyats and D. I. Proskurovskiĭ, *Pulsed Electric Discharge in Vacuum* [in Russian], Nauka, Novosibirsk (1984), 256 pp.
[2] A. S. El'chaninov, F. Ya. Zagulov, S. D. Korovin, and G. A. Mesyats, Zh. Tekh. Fiz. **51**, 1005 (1981) [Sov. Phys. Tech. Phys. **26**, 601 (1981)].
[3] S. Ya. Belomyttsev, S. D. Korovin, and I. V. Pegel', Zh. Tekh. Fiz. **69**(6), 97 (1999) [Tech. Phys. Lett. **44**, 695 (1999)].
[4] N. M. Bykov, V. P. Gubanov, A. V. Gunin *et al.*, ''Development of Long Lifetime Cold Cathode'' in *Proceedings of 10th International Pulsed Power Conference, Albuquerque, NM, 1995*, pp. 71–74.
[5] A. S. El'chaninov, F. Ya. Zagulov, S. D. Korovin *et al.*, *High-Current Pulse-Periodic Electron Accelerators for Generation of Microwave Radiation*, in: *Relativistic High-Frequency Electronics* [in Russian], Institute of Applied Physics Press, Gorky (1981), pp. 5–21.
[6] I. K. Kurkan, V. V. Rostov, and E. M. Tot'meninov, Pis'ma Zh. Tekh. Fiz. **24**(10), 43 (1998) [Tech. Phys. Lett. **24**, 388 (1998)].
[7] B. A. Koval', D. I. Proskurovskiĭ, V. F. Tregubov, and E. B. Yankelevich, Pis'ma Zh. Tekh. Fiz. **5**, 603 (1979) [Sov. Tech. Phys. Lett. **5**, 246 (1979)].
[8] B. A. Koval', D. I. Proskurovskiĭ, and E. B. Yankelevich, *Emitter Materials for Long-Lived Cold-Emission Cathode* in *Abstracts of Papers presented at Third All-Union Symposium on High-Power Pulsed Electronics*, Tomsk, 1978 [in Russian], pp. 19–20.
[9] A. A. Plyutto, V. N. Ryzhkov, and A. T. Kapin, Zh. Éksp. Teor. Fiz. **47**, 494 (1964) [Sov. Phys. JETP **20**, 328 (1964)].
[10] C. W. Kimblin, J. Appl. Phys. **44**, 3074 (1973).
[11] J. E. Daalder, Physica C **104**, 91 (1981).
[12] D. I. Proskurovskiĭ and E. B. Yankelevich, Radiotekh. Élektron. (Moscow) **24**(1), 132 (1979).

Translated by R. M. Durham